MODELING IGNITION AND EXTINCTION IN CONDENSED PHASE
COMBUSTION

BY

SUSHILKUMAR KOUNDINYAN

DISSERTATION

Submitted in partial fulfillment of the requirements
for the degree of Doctor of Philosophy in Theoretical and Applied Mechanics
in the Graduate College of the
University of Illinois at Urbana-Champaign, 2016

Urbana, Illinois

Doctoral Committee:

    Professor D. Scott Stewart, Chair
    Professor Moshe Matalon
    Professor Nick Glumac
    Professor Waltraud Kriven

Abstract

The characteristics of ignition and extinction in thermites and intermetallics are a subject of interest in developing the latest generation of energetic materials. An experimental "striker confinement" shock compression experiment was developed in the Prof. Glumac's research group at the University of Illinois to study ignition and reaction in composite reactive materials. These include thermitic and intermetallic reactive powders. We discuss our model for the ignition of copper oxide-aluminum thermite in the context of the striker experiment and how a Gibbs formulation model, that includes multi-components for liquid and solid phases of aluminum, copper oxide, copper and aluminum oxide, can predict the events observed at the particle scale in the experiments. Furthermore, the characteristics of a steady diffusion flame that arises at the interfaces of two condensed phase reactant (titanium-boron) and gas reactant (methane-air) streams that form an opposed counterflow are discussed. In the the gas flow scenario, the asymptotic analysis is carried on both constant and variable density formulations and compared the solutions to those obtained numerically. In the case of condensed phase reactants, several types of analyses are carried out at increasing levels of complexities: an asymptotic analysis valid in the limit of low strain rates (high residence time in the reaction zone), a constant mixture density assumption that simplifies the flow description, diffusion models with equal and unequal molecular weights for the various species, and a full numerical study for finite rate chemistry, composition-dependent density and strain rates extending from low to moderate values.

To Amma and Appa

Acknowledgements

Everything that I have accomplished during my pursuit of doctoral degree would not be possible without the support of my advisor, D. Scott Stewart. His endless patience in guiding my scientific curiosity along with the life lessons he imparted, have made my years in graduate school a life transforming experience. I have the utmost respect and gratitude for Prof. Moshe Matalon. His guidance with various aspects of my dissertation has been invaluable. I would like to thank the other members of my committee, Prof. Nick Glumac and Prof. Trudy Kriven for their feedback. I also wish to thank Dr. John Bdzil for his assistance during the early stages of my research.

To my fellow graduate students, Brandon Lieberthal, Kibaek Lee, Sungjin Choi, Alberto Hernández, Lana Šteković, and Alex Wass, I had the most enjoyable time in Graduate School thanks to you guys. I will always treasure the wonderful moments we have shared these past 6 years.

My best friend, Forbes Leung, has been a constant source of support and amusement during my adult life. His advice on all facets of life has made me into a well-rounded person. I am also grateful to Sarath Velagaleti, Josh Kezele and Tim Wong. You guys are the best! I have met many incredible people during my tenure at Champaign/Urbana. While I cannot list all of them, I would like to mention Jyothi Sadhu, Nishanth Lingala, Mahesh Natarajan, Sohan Kale, Gokul Pathikonda, Nek Sharan, Krishna Valavala and Dhruv Gelda. The numerous wonderful memories I share with each of them are priceless. I would be remiss if I did not acknowledge Hamid (aka the Jerusalem guy). His delicious food has kept me healthy during the most stressful of times.

My wife, Aishwarya, is the love of my life. She makes me a better person everyday through her warmth and compassion. I eagerly look forward to growing old with her. My brother, Srivathsan, is the smartest and kindest person I know. While he is younger than me, his advice and support throughout my life has been invaluable. Finally, I am very thankful for the love and support my parents (Ms. Parvatham and Mr. Prabu Koundinyan) provided all my life. I will never forget the sacrifices they have made for my brother and me. Therefore, I dedicate this thesis to them.

Table of Contents

List of Tables

List of Figures

Chapter 1

Introduction

1.1   Background

Energetic materials are a broad class of manufactured materials that traditionally include both propellants and explosives, but thermite and intermetallic/metal mixtures as well. These materials are made from a set of initial components, elements or compounds, that may have been subjected to processing or may have imperfections and contaminants such as cracks, inclusions or surface oxidation. Energetic compounds include molecular explosive and molecular oxidizer crystallites, like HMX and ammonium perchlorate (AP), plastic binders and resins like HTPB, metals like aluminum (Al) and titanium (Ti), metal oxides like iron oxide, copper oxide, and intermetallic elements like carbon, silicon and boron. Our examples of constituents are not exhaustive, but include those commonly used in the manufacture of energetic materials. Each component in the mixture, prior to the composite assembly, has its individual mechanical and thermo-chemical identity that is often well-characterized as an inert material. The individual components are combined to make an agglomerated composite mixture that is pressed or cast into a mold for explosive and propellant applications. The powders and crystallites of the constituent compounds have a characteristic mean dimension that varies from hundreds of to one micron and particle size distribution that is known and can be controlled.

As an alternative to an agglomerated composite, there is interest in forming layers of the constituent components in laminates or regular arrays, with specific interstitial spacing between components. A prominent example is related to the development of reactive nano-foils that are used in special joining and welding applications [1]. In this case thin, approximately 10 micron layers of foil

1

(of say nickel and aluminum) are pressed into a laminate ply. The reaction to form nickel/aluminum products is started with thermal initiation (heating) that first melts the aluminum and allows the reaction to proceed. The speed of the reacting front that moves perpendicular to the plies dependent on the foil spacing and ply composition and construction [2].

Reactive energetic material, as defined in a 2004 US National Academy of Sciences report [3], is a class of materials that generally combines two or more nonexplosive solids that upon ignition react and release energy. The source of the ignition energy is assumed to come from a shock wave caused by impact of the reactive material with a stationary target. The ignition energy is obtained from the fact that a composite agglomerate has interstitial voids that are in the range of 1 to 20 % by volume. After impact a densification of the composite occurs, and because of the density and acoustic impedance contrast between composite constituents, local energy concentrations occur. This leads to localized heating (hot spots) that in turn lead to the thermal events that are required to melt the constituent components and initiate the reaction at interfaces. Once melting occurs, then in addition to greater species mobility of reactants, there are relative motions of the constituent material. The underlying specification of the particle sizes and the characteristic spatial features introduces an additional length scale. On particle-size scale the interfaces may not be planar thus flows can be generated in contiguous interacting regions on the microscale dimensions of the composite. Thus relative motions of the condensed phase constituents occur in the decomposition regions of propellants. Consider a standard composite solid propellant matrix composed of ammonium perchlorate (AP) and small aluminum particles embedded in a rubbery binder. Under standard operating conditions, the region between the surface of the propellant exposed to hot products of the rocket chamber to the cold core of the propellant suffers an extremely large temperature gradient. The materials in this thermal layer change from solids, to liquids, to mixed liquids, and eventually to mainly gases. There are significant differences in the thermal expansion of the oxidizers, the binders and the metals and those differences can generate flows of molten materials in chemically active condensed phase region, with local flow speeds in the micro-scale environment that are comparable to those of propellant regression rates (i.e., on the order of $1\,\mathrm{cm/s}$). The majority of propellants investigation have focused on the gas-phase reactions that occur above the propellant surface, with

minimal attention given to the internal condensed phase phenomena [4]. In part this is because decomposition and chemical reactions in composite propellants are quite complex and involve phase transformation and/or gas products.

1.2 Rationale

There is interest in engineering energetic nano-composite reactive material, made from sub micron metal and metal oxides to enable rapid and localized high temperature heating which can be activated by shock impact. Therefore, this dissertation focuses on modeling ignition and extinction in condensed phase combustion. Before we proceeded to analyze the condensed phase behavior, we focused on understanding the phenomenon in gas phase. The second chapter is concerned with the asymptotic analysis of combustion equations in counterflow geometry and their validation to numerical methods. The asymptotic analysis yields analytic insights into extinction behavior for large activation energy and it is compared to numerical solutions for both constant and variable density formulations.

The third chapter analyzes the steady diffusion flame that forms at the interface of two condensed phase reactant streams. Because of experiments done by Glumac et al. [5], we have focused on the Ti/B system and describe it simply with three components; two reactants Ti and B, and the product TiB_2. We have ignored the intermediary species TiB in this model. We analyze the effect of density variation and diffusion on the reaction between titanium and boron. The diffusion model for the components is described by Maxwell-Stefan diffusion law, which is formulated in terms of binary diffusivities. We analyze the microscale length and relative motion between the reactants, which represent the characteristic scales, and in particular the strain rate that determines the conditions that differentiate between vigorous and weak burning between titanium and boron. [6]

Finally, we present a model for ignition between aluminum (Al) and and copper oxide (CuO), which produces aluminum oxide (Al_2O_3). The diffusion and reaction model presented in chapter 3 is updated by incorporating phase change for all the materials. The liquid and solid phases of each species is treated as a separate material while the phase change itself is modeled as a reaction.

The experiments done by Glumac et al. [7], show rapid ignition and quenching events once the shock passes through the unreacted sample. An typical size of such events is approximately 100 μm. Therefore, a slab geometry with a mixing region of 100 μm is chosen and a thermal impulse is induced on the aluminum side of the slab. Two different thermal impulses (3000K and 2000K) were studies to analyze the effect of local temperature on the reaction.

Overall, this dissertation presents a model for handling phase change and material diffusivities during ignition and extinction of condensed phase combustion. The second chapter analyzes gas phase counterflow combustion to develop an analytic understanding of the governing equations. The third chapter models the Ti/B counterflow system without considering phase change or intermediary species. The fourth chapter analyzes ignition in Al/CuO system while considering phase change and material diffusivities for all 8 constituent species.

Chapter 2

Counterflow Diffusion Flames - Numerical Solutions vs Asymptotic Approximation

2.1 Introduction

The governing equations for diffusion flames consists of fluid mechanics equations in addition to the mass balance equations for various species involved in the chemical reaction [8]. These equations are too difficult to solve analytically so people choose to solve them either using numerical methods or other approximate methods, such as asymptotics. Liñán [9], in his seminal work, thoroughly analyzes the structure of a constant-density planar diffusion flame in a counterflow geometry with unity Lewis numbers, which assumes that the chemical reactions are all confined to a thin reaction zone. After his work, many others have looked into the asymptotic structure of counterflow diffusion flame near extinction under various conditions [10–12]. Cheatham and Matalon [13] derive a general formulation, unrestricted to any particular diffusion flame geometry, and it is multidimensional and time-dependent. The asymptotic methods give a clear insight of the solution dependence on various variables in the governing equations at limiting cases.

Numerical methods used to solve diffusion flame equations have been employed to approximate various features of the flame under different conditions. Smooke et al. [14], has examined the numerical solution of two-dimensional axis-symmetric laminar diffusion flames for methane-air configuration with full reaction chemistry. He also presents a generalized computational method using boundary value methods with adaptive gridding [15]. Ribert et al. [16] have even included non-ideal equation of state (Soave-Redlich-Kwong EOS) in their equations to model O2/H2 reactions in subcritical and supercritical conditions. Many others have also numerically computed the structure and extinction of counterflow diffusion flames for various input and chemical configurations [17–22].

Experimental investigations into the structure and extinction of diffusion flames are necessary to validate the theoretical and numerical calculations. Different techniques used in counterflow diffusion flame experiments are summarized by Tsuji [23]. Ishizuka and Tsuji [24] measure the effect of inert gas in initial mixtures on the extinction of diffusion flames. Sung et al. [25] captured the structure of counterflow diffusion flames for various strain rates and compared it to numerical solutions. Many others have also experimentally looked into the structure and extinction of counterflow diffusion flames for various conditions [26, 27].

In this chapter, we are looking into the effects of density variations in counterflow diffusion flame. The similarity solution is used to essentially transform the governing equations to quasi one-dimensional system. An asymptotic analysis is presented for both constant and variable density formulations and compared to numerical solutions. The numerical solution is verified with the asymptotic approximation at the Burke-Schumann limit. We present the comparisons for large/small Lewis number and mixture strength under constant and variable density formulations. The asymptotic extinction temperature had moderate agreement with numerical solution while the corresponding flame position matched well with each other. The asymptotic extinction Damköhler number for both formulations also matched well with the numerical solution.

2.2 Formulation

A counterflow geometry, as shown in Figure 3.1, consists of two opposing streams of equal strain rate, 2ϵ, one containing fuel with mass fraction $\tilde{Y}_{F_0}$, and the other containing oxidizer with mass fraction, $\tilde{Y}_{O_1}$. When successfully ignited combustion occurs in the form of a flat diffusion flame parallel to, and located on one side of the stagnation plane (see Figure 3.1). The temperature and density of the streams are assumed equal and given by $\tilde{T}_0$ and $\tilde{\rho}_0$ respectively. The chemical reaction is modeled by an overall irreversible reaction of the form:

$$\nu_F \, \text{Fuel} + \nu_O \, \text{Oxidizer} \rightarrow \text{Products} + \{Q\}$$

where ν_i is the stoichiometric coefficient of species i (subscripts F and O stand for Fuel and Oxidizer, respectively) and Q represents the total chemical heat release. The reaction rate obeys an Arrhenius type relation with an activation energy E and a pre-exponential factor B, namely

$$\tilde{\omega} = B\left(\frac{\tilde{\rho}\tilde{Y}_F}{W_F}\right)\left(\frac{\tilde{\rho}\tilde{Y}_O}{W_O}\right)e^{-E/R\tilde{T}} \tag{2.1}$$

where $\tilde{\rho}$ and $\tilde{T}$ represent density and temperature of the mixture, W_i is the molecular weight of species i and R is the universal gas constant.
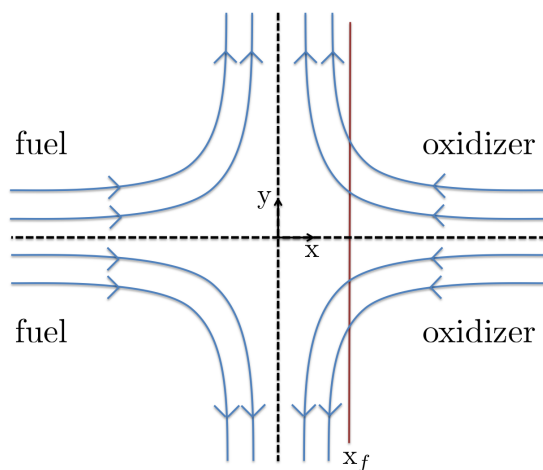
Figure 2.1: Schematic of a counterflow diffusion flame.

In the following, the effect of gravitational forces is assumed to be negligible. The mixture properties such as thermal conductivity λ, specific heat at constant pressure c_p and viscosity μ are all assumed constant. Diffusion of each of the two reactants obeys Fick's law with $\mathscr{D}_F$ and $\mathscr{D}_O$ the binary diffusivities of the fuel/oxidizer into the inert gas. The mass diffusivities are assumed to vary linearly with temperature such that $\tilde{\rho}\mathscr{D}_F$ and $\tilde{\rho}\mathscr{D}_O$ remain constant. The mixture is assumed to behave as an ideal gas, satisfying $\tilde{P}_0 = \rho_0 R T_0 / \overline{W}$, where $\overline{W}$ is the molecular mass of the mixture assumed constant. The combustion process is nearly isobaric, which implies that pressure variations from the ambient pressure $\tilde{P}_0$ are small, on the order of the squared (representative) Mach number.

We normalize the mass fractions $\tilde{Y}_F$ and $\tilde{Y}_O$ with $\tilde{Y}_{F_0}$ and $\nu\tilde{Y}_{F_1}$ respectively, where $\nu =$

7

$\nu_O W_O / \nu_F W_F$ is the mass-weighted stoichiometric coefficient ratio. The initial mixture strength is then given by $\phi = \nu \tilde{Y}_{F_0} / \tilde{Y}_{O_1}$. The pressure and temperature are made dimensionless by $\tilde{P}_0$ and q/c_p, where $q = Q\tilde{Y}_{F_0} / \nu_F W_F$ is the heat release parameter, and density by $\tilde{\rho}_c = \tilde{P}_0 \overline{W} c_p / qR$. Using ϵ^{-1} as a characteristic time, the characteristic velocity and length are $\sqrt{\mathscr{D}_{th}\,\epsilon}$ and $\sqrt{\mathscr{D}_{th}/\epsilon}$ respectively, where $\mathscr{D}_{th} = \lambda / \tilde{\rho}_c c_p$ is the thermal diffusivity of the mixture.

The flow field, assumed two-dimensional with u, v representing the x, y velocity components, admits a "similarity solution" of the form

$$u = u(x), \qquad v = y\,\overline{v}(x), \qquad p = p(x, y) \tag{2.2}$$

such that the transverse pressure gradient varies linearly with distance from the axis, namely $\partial p / \partial y = -Cy$, with the constant C is determined by boundary conditions. For a flat steady flame T, Y_F and Y_O vary only along the axial direction x. The steady state governing equations in dimensionless form become:

$$\frac{d(\rho u)}{dx} + \rho \overline{v} = 0 \tag{2.3}$$

$$\rho u \frac{du}{dx} = -\frac{\partial p}{\partial x} + Pr\left(\frac{d^2 u}{dx^2} + \frac{1}{3}\frac{d}{dx}\left(\frac{du}{dx} + \overline{v}\right)\right) \tag{2.4}$$

$$\rho u \frac{d\overline{v}}{dx} + \rho \overline{v}^2 = C + Pr\frac{d^2\overline{v}}{dx^2} \tag{2.5}$$

$$\rho u \frac{dY_F}{dx} = L_F^{-1}\frac{d^2 Y_F}{dx^2} - \omega \tag{2.6}$$

$$\rho u \frac{dY_O}{dx} = L_O^{-1}\frac{d^2 Y_O}{dx^2} - \omega \tag{2.7}$$

$$\rho u \frac{dT}{dx} = \frac{d^2 T}{dx^2} + \omega \tag{2.8}$$

$$\rho T = 1 \tag{2.9}$$

The parameters that appear in these equations are the Lewis numbers $L_F = \lambda / \tilde{\rho} c_p \mathscr{D}_F$, $L_O =$

$\lambda/\tilde{\rho}c_p\mathscr{D}_O$ and Prandtl number $Pr = \mu c_p/\lambda$. The reaction rate ω is:

$$\omega = D\,\theta^3(\rho/\rho_a)^2\,Y_F\,Y_O\exp\left\{\frac{\theta(T-T_a)}{T/T_a}\right\} \tag{2.10}$$

where,

$$D = \frac{1}{\epsilon}\left(\frac{R\tilde{T}_a}{E}\right)^3\frac{\nu_O B}{\tilde{\rho}_c W_F}\,\tilde{\rho}_a^2\,\tilde{Y}_{F_0}\,e^{-E/R\tilde{T}_a} \tag{2.11}$$

is the Damköhler number, which represents the flow-to-chemical reaction times ratio, and $\theta = qE/c_p R\tilde{T}_a^2$ is the activation energy parameter. Here $\tilde{T}_a$ is the adiabatic flame temperature corresponding to complete combustion of reactants (to be determined) and $\tilde{\rho}_a$ is the associated density. We note that hereafter when the same symbols are used for dimensional and dimensionless variables, the one without a "tilde" denotes the same quantity but in dimensionless form. Hence, for a given mixture and for given state conditions, the Damköhler $D \propto \epsilon^{-1}$ is controlled by the flow.

Far upstream on either side of the stagnation plane, taken without loss of generality at $x = 0$, the state of the gas is uniform and the velocities $v \sim 2y$ and $u \sim -2x$. Hence, the boundary conditions are:

$$\overline{v} = 2,\ T = T_0,\ Y_F = 1,\ Y_O = 0 \quad \text{as} \quad x \to -\infty \tag{2.12}$$

$$\overline{v} = 2,\ T = T_0,\ Y_F = 0,\ Y_O = \phi^{-1} \quad \text{as} \quad x \to \infty \tag{2.13}$$

When applying these conditions to (2.5), one finds that $C = 4\rho_0$. Finally, to ensure that the stagnation plane remains at the origin, the condition

$$u(0) = 0 \tag{2.14}$$

is imposed.

In the following sections, the coupled nonlinear boundary value problem will be solved using two different approach: (i) an asymptotic approach that exploits the limit of a large activation energy parameter and (ii) a direct numerical approach. Moreover, to elucidate the role of thermal expansion on the combustion process both cases of constant and variable density flows will be

discussed.

2.3 Large Activation Energy Asymptotics

In deriving the solution for $\theta \gg 1$, we follow the formulation of Cheatham and Matalon [13], which is valid for distinct and non-unity Lewis numbers and carried to $\mathcal{O}(\theta^{-1})$. The analysis covers the whole range $\infty > D > D_{\text{ext}}$, namely from complete combustion to extinction. The reaction is confined to a thin reactive-diffusive region which, when $\theta \to \infty$, shrinks to a sheet located at $x = x_f$. Jump conditions across x_f account for the heat released and the degree of fuel and oxidizer consumed in the reaction zone.

Equations (2.3)-(2.9) must then be solved on either side of the reaction sheet with $\omega = 0$ and subject to:

$$[u] = [\bar{v}] = [T] = [Y_F] = [Y_O] = 0 \tag{2.15}$$

$$\left[\frac{d\bar{v}}{dx}\right] = 0\,, \qquad [p] = \tfrac{4}{3} Pr \left[\frac{du}{dx}\right] \tag{2.16}$$

$$\left[\frac{dT}{dx}\right] = -\frac{1}{L_F}\left[\frac{dY_F}{dx}\right] = -\frac{1}{L_O}\left[\frac{dY_O}{dx}\right] \tag{2.17}$$

$$Y_F|_{x=x_f^+} = \theta^{-1} L_F S_F(\gamma, \delta) \tag{2.18}$$

$$Y_O|_{x=x_f^-} = \theta^{-1} L_O S_O(\gamma, \delta) \tag{2.19}$$

where all variables consist here of the combined first two terms[1] in their expansion in θ^{-1}, for example $T = T^{(0)} + \theta^{-1} T^{(1)} + \cdots$. Here the operator $[\cdot]$ denotes the jump in the quantity, namely the difference between its values at x_f^+ and x_f^-. The reactant leakage through the reaction sheet (2.18)-(2.19) is expressed in terms of the "leakage functions" S_F and S_O, which depend on the two auxiliary $\mathcal{O}(1)$ parameters

$$\gamma = \frac{dT/dx|_{x_f^+} + dT/dx|_{x_f^-}}{[dT/dx]} \tag{2.20}$$

---

[1] If the equations are solved for the leading and first terms recursively, the jump relations that must be satisfied for each term in the expansion are different than those listed above; for detail see [13].

$$\delta = \frac{4 L_F L_O}{[dT/dx]^2} D e^{h_f} \tag{2.21}$$

The parameter γ, which depends only on the leading order temperature, measures the excess heat conducted on one side of the reaction sheet, or equivalently on the mixture strength. The parameter δ is a measure of the reactivity of the chemical reaction and depends primarily on the total enthalpy available at the reaction sheet

$$h_f = \tfrac{1}{2}(1 - \gamma) h_F + \tfrac{1}{2}(1 + \gamma) h_O \,,$$

where h_F and h_O are the enthalpies associated with the fuel and oxidizer, determined from

$$
\begin{aligned}
T + L_F^{-1} Y_F |_{x=x_f^+} &= T_a + \theta^{-1} h_F \\
T + L_O^{-1} Y_O |_{x=x_f^-} &= T_a + \theta^{-1} h_O \,.
\end{aligned}
$$

The above formulation is restricted to $-1 < \gamma < 1$, or to what has been termed by [9] the "diffusion-flame regime", excluding the "premixed-flame regime" associated with $\mathcal{O}(1)$ leakage of one of the reactants.

The leakage functions S_F and S_O are obtained as matching conditions from the numerical solution describing the inner structure of the reaction zone [13], and due a symmetry property of these equations may be expressed as

$$
S_F =
\begin{cases}
S_1 & \text{for } 0 \le \gamma < 1 \\
S_2 & \text{for } -1 < \gamma \le 0
\end{cases}
\tag{2.22}
$$

$$
S_O =
\begin{cases}
S_2 & \text{for } 0 \le \gamma < 1 \\
S_1 & \text{for } -1 < \gamma \le 0 \,.
\end{cases}
\tag{2.23}
$$

For a given $\delta > \delta_c$, the solution in the reaction zone is multi-valued; the two distinct solutions merge at $\delta = \delta_c$ and no solution exists otherwise. When expressed in terms of δ, each of the leakage functions traces two branches. Along one of the branches, referred to as the *lower-branch*, S_1 and

S_2 are both decreasing functions of δ that tend to zero, or to the Burke-Schumann limit, as $\delta \to \infty$. Along the other branch, referred to as the *upper-branch*, S_1 and S_2 are both increasing functions of δ that tend, in the limit, to a state associated with $\mathcal{O}(1)$ reactant leakage, a state that is of no interest believed to be unstable.

In order to have direct access to the leakage functions, without the necessity to repeatedly integrate numerically the structure equations, [13] provided the following formulae

$$S_1 = \begin{cases} a_0\, \delta^{-4/3} \exp\left\{ - a_1 (\delta - \delta_c)^{a_2} \right\} & \text{lower branch} \\ \delta^{-1/3} \left(q_0 + q_1 (\delta - \delta_c)^{q_2} \right) & \text{upper branch} \end{cases} \qquad (2.24)$$

$$S_2 = \begin{cases} b_0\, \delta^{-4/3} \exp\left\{ - b_1 (\delta - \delta_c)^{b_2} \right\} & \text{lower branch} \\ \delta^{-1/3} \left(r_0 + r_1 (\delta - \delta_c)^{r_2} \right) & \text{upper branch} \end{cases} \qquad (2.25)$$

that best fit the numerical data, where

$$\delta_c = \left(1 - |\gamma| - (1-|\gamma|)^2 + .26(1-|\gamma|)^3 + .055(1-|\gamma|)^4 \right) e^1 \qquad (2.26)$$

is an approximation for the critical δ_c, first obtained by [9]. The coefficients a_i, b_i, q_i and r_i, which depend on γ only, are given by Cheatham and Matalon [13], which should be consulted for further detail.

We are thus faced with a free surface, nonlinear boundary value problem that consists of solving equations (2.3)-(2.9) with $\omega = 0$ on either side of the reaction sheet, subject to the the jump conditions at (2.15)-(2.19) at $x = x_f$ and the boundary conditions (2.12)-(2.14). As noted in [13] the aforementioned jump conditions are sufficient to determine the mass fraction and temperature profiles as well as the location x_f of the reaction sheet. The flame temperature T_f is determined as the value of the temperature at the reaction sheet, namely $T_f = T(x_f)$.

2.3.1 Constant density flow

It must be noted that for the constant density case, $\rho = 1$ is effectively the equation of state that replaces (2.9), with $\rho_a = 1$ in the reaction rate (2.10). The velocity field in this case is exactly satisfied by

$$u = -2x, \qquad v = 2y, \qquad p = p_s - 2(x^2 + y^2)$$

where p_s is the stagnation pressure. The remaining equations admit the explicit solution

$$T = \begin{cases} T_0 + (T_f - T_0)\dfrac{1 + \operatorname{erf} x}{1 + \operatorname{erf} x_f} & \text{for } -\infty < x < x_f \\[2mm] T_0 + (T_f - T_0)\dfrac{1 - \operatorname{erf} x}{1 - \operatorname{erf} x_f} & \text{for } x_f < x < \infty \end{cases} \tag{2.27}$$

$$Y_F = \begin{cases} 1 - (1 - \theta^{-1} L_F S_F)\dfrac{1 + \operatorname{erf}(\sqrt{L_F}x)}{1 + \operatorname{erf}(\sqrt{L_F}x_f)} & \text{for } -\infty < x < x_f \\[3mm] \theta^{-1} L_F S_F \dfrac{1 - \operatorname{erf}(\sqrt{L_F}x)}{1 - \operatorname{erf}(\sqrt{L_F}x_f)} & \text{for } x_f < x < \infty \end{cases} \tag{2.28}$$

$$Y_O = \begin{cases} \theta^{-1} L_O S_O \dfrac{1 + \operatorname{erf}(\sqrt{L_O}\,x)}{1 + \operatorname{erf}(\sqrt{L_O}\,x_f)} & \text{for } -\infty < x < x_f \\[3mm] \phi^{-1} - (\phi^{-1} - \theta^{-1} L_O S_O)\dfrac{1 - \operatorname{erf}(\sqrt{L_O}\,x)}{1 - \operatorname{erf}(\sqrt{L_O}\,x_f)} & \text{for } x_f < x < \infty \end{cases} \tag{2.29}$$

where the determination of the position of the reaction sheet x_f and the flame temperature T_f result from solving the following transcendental relations

$$\frac{1 - \operatorname{erf}^2(\sqrt{L_F}x_f)}{1 - \operatorname{erf}^2(\sqrt{L_O}x_f)}\left\{ \frac{1 + \operatorname{erf}(\sqrt{L_O}x_f) - 2\theta^{-1}\phi L_O S_O}{1 - \operatorname{erf}(\sqrt{L_F}x_f) - 2\theta^{-1} L_F S_F} \right\} e^{(L_F - L_O)x_f^2} = \phi\sqrt{\frac{L_O}{L_F}} \tag{2.30}$$

$$T_f = T_0 + \frac{1}{2L_F}\left\{ \frac{1 - \operatorname{erf}(\sqrt{L_F}x_f) - 2\theta^{-1} L_F S_F}{(1 - \operatorname{erf}^2(\sqrt{L_F}x_f))/(1 - \operatorname{erf}^2 x_f)} \right\} e^{(1 - L_F)x_f^2} \tag{2.31}$$

respectively. Consistency of the asymptotic solution requires retaining only the first two terms in the expansion of (2.30)-(2.31) in powers of θ^{-1}. The leading terms are obtained by setting $S_F = S_O = 0$, leading to

$$\frac{1 + \operatorname{erf}(\sqrt{L_F}x_f)}{1 - \operatorname{erf}(\sqrt{L_O}x_f)} e^{(L_F - L_O)x_f^2} = \phi\sqrt{\frac{L_O}{L_F}} \tag{2.32}$$

$$T_a = T_0 + \frac{1}{2\sqrt{L_F}} \frac{(1 - \mathrm{erf}^2 x_f)e^{(1-L_F)x_f^2}}{1 + \mathrm{erf}(\sqrt{L_F}x_f)} \, , \tag{2.33}$$

and corresponding to the Burke-Schumann limiting solution. Solving for the $\mathcal{O}(\theta^{-1})$ terms results in cumbersome relations; instead, the solution of (2.30)-(2.31) was sought numerically using a root solving algorithm.

2.3.2 Variable density flow

For a variable density flow, the equations for the temperature and mass fractions are coupled to the fluid dynamic equations and must satisfy the jump conditions (2.15)-(2.19) at a location x_f that remains to be determined. In the absence of an analytical solution, a numerical procedure is used to solve the boundary value problem (2.3)-(2.9). An initial guess for the flame position x_f, temperature T^*, transverse $\bar{v}^*$ and axial u^* velocities at the reaction sheet location (denoted by *), represented by α_i with $i = 1, 4$, respectively, is first made and the equations solved using the Matlab boundary value solver bvp5c. The solver uses the four-stage Lobatto-IIIa collocation algorithm to solve the boundary value problem. [28]. A Newton-Raphson algorithm is then used to iterate on the guessed values until the four conditions $\mathcal{F}_i = 0 \ \{i = 1, \ldots, 4\}$ are satisfied simultaneously, where

$$\mathcal{F}_1 = \frac{1}{L_F}\left[\frac{dY_F}{dx}\right] - \frac{1}{L_O}\left[\frac{dY_O}{dx}\right] \qquad \mathcal{F}_2 = \left[\frac{dT}{dx}\right] + \frac{1}{L_F}\left[\frac{dY_F}{dx}\right] \tag{2.34}$$

$$\mathcal{F}_3 = [d\bar{v}/dx] \qquad \mathcal{F}_4 = u|_{x=0} \tag{2.35}$$

The Newton-Raphson algorithm requires a numerical Jacobian, which is populated by second order central difference analysis of the guessed values with $\Delta\alpha_i = 10^{-6}$, and is implemented until convergence is achieved, namely $|\mathcal{F}_i| < 10^{-6}$. The x-momentum equation (2.4) is used together with the jump condition (2.16) a-posteriori, in order to solve for the axial dependence of the pressure.

For a given set of parameters, an arc-length continuation procedure is followed for the determination of the solution over the entire range $\delta_c < \delta < \infty$ as described next. For the construction of the lower branch, the analytical constant density flow solution is used as an initial guess in the

algorithm for solving the variable density Burke-Schumann limit solution. Starting with a large value of δ, here taken as $\delta = 10$, the Burke-Schumann solution is used as the initial guess and when decreasing δ incrementally, the previous solution is used as the initial guess until $\delta = \delta_c$ is reached. The upper branch solution is obtained starting from $\delta = \delta_c$, and increasing δ by small increments.

2.4 Numerical Approach

The numerical solution of the boundary-value problem (2.3)-(2.9) is computed by using a modified psudo-time relaxation method with uniform grid to solve the equations. Therefore, a time derivative is imposed to the left hand side of Eqs. (2.5)-(2.8), which are used to compute $\bar{v}$, Y_F, Y_O and T respectively. u is computed by integrating Eqn (2.3) using the trapezoidal rule with the boundary condition given in Eqn (2.14) at the end of each time step. Since x spans from $-\infty$ to $+\infty$, a sufficiently large computational domain size must be selected, beyond which the changes in variables are negligible. Therefore, the Burke-Schumann limit solution is first computed and used as guidance for setting the domain boundaries. It should be noted that the flame position in the numerical approximation is determined as the location where the flame temperature is at its maximum.

Along a unit length of domain, there exists typically 250 to 500 grid points. For example, a domain of [-3, 3] contains 1500 to 3000 points. The length of reaction zone gets smaller as Damköhler number increases. Therefore, in order to resolve accurately the reaction zone at higher Damköhler numbers, a larger number of grid points is needed. We used fourth order Runge-Kutta for time derivative and the time step is determined by trial and error. Typically, time step usually varies between 10^{-7} and 10^{-6}. The Burke-Schumann solution is used as an initial condition at time $t = 0$ for large Damköhler number. Let f be the solution of variable at $t = n$ and $\hat{f}$ be the solution of variable at $t = n + 1$, which is a full computational second later. The solution is assumed to have approached steady state when $\max_i |f_i - \hat{f}_i| < 10^{-6}$, where i corresponds to the domain node number.

The explicit direct approach fails as the Damköhler number gets closer extinction value because the equations become unstable. To extend the curve around the extinction point we adopt a version

of the continuation method used by Kurdyumov and Matalon [29] to compute the unstable portion of a response diagram. The governing equations are solved with an additional constraint that the temperature remains constant at some reference point, say $T(x^*) = T^*$. This additional constraint is used to iterate on the value of Damköhler number, D, by solving the temperature equation at this fixed point during each time step. Convergence is achieved when both the Damköhler number and the space distribution of solution do not vary within a computational second.

For the results presented below the following parameters were held fixed (unless otherwise stated):

$$T_0 = 0.134, \qquad \theta = 20, \qquad Pr = 0.7$$

which correspond to typical values of hydrocarbon combustion at atmospheric conditions. The mixture strength and fuel Lewis number (L_F) are varied over the range

$$0.5 < L_F < 2, \qquad 0.4 < \phi < 4,$$

corresponding to various degree of dilution [30]. The results obtained by varying fuel Lewis number is equivalent to that obtained by varying oxidizer Lewis number due to symmetry. Hence, we set $L_O = 1$. The entire range of strain rates, from low up to the extinction value are covered by varying the Damköhler number from sufficiently large values down to extinction.

2.5 Results

For sufficiently large Damköhler number (or small strain rate), the Burke-Schumann solution should match the computational solution, which is used as a validation step for the numerical method and as a starting point for the response curve calculation. In Figure 2.2, we compare the numerical and asymptotic solutions for the variable density configuration. As it can be seen, the numerical solution matches the asymptotic solution extremely well, with the small difference attributed to the finite reaction rate used in the numerical solution compared to the infinitely fast chemistry of the the asymptotic solution. Also, the domain boundaries seem more than sufficient to span the infinite

16

physical domain as there is negligible change in temperature or mass fraction profiles beyond the numerical boundaries. We conducted this validation step for all considered parameter variations and they yielded similar results.
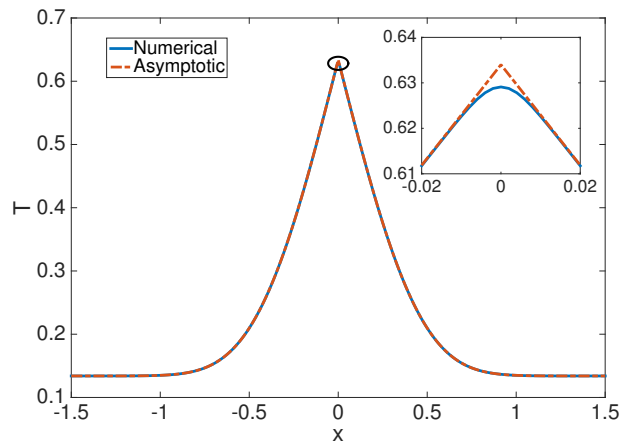
(a) Temperature
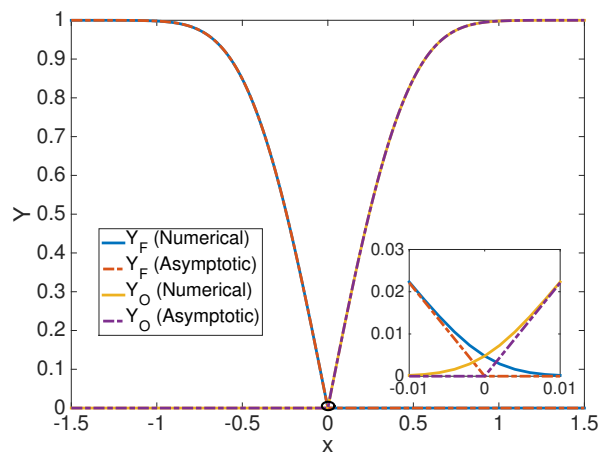
(b) Mass fraction

Figure 2.2: Comparison of the variable density numerical and asymptotic solutions for $D = 1000$, with $L_F = 1$, $L_O = 1$, $\phi = 1$.

2.5.1   Reaction sheet location

The reaction in the Burke-Schumann limit is confined to a sheet located at x_f obtained from the asymptotic expressions (2.30) and (2.17) for the constant- and variable-density flows, respectively. In Figure 2.3, we show the dependence of x_f on the mixture strength for various values of the fuel Lewis number. For unity Lewis numbers, i.e., when L_F is also equal to one, the reaction sheet lies on the fuel side for $\phi < 1$ (lean conditions) and on the oxidizer side for $\phi > 1$ (rich conditions). Density variation has a strong effect on the flame position. For low mixture strength values, the variable density solution is higher than the constant density solution and vice-versa for high mixture strength values. As L_F increases, the flame position moves more towards the oxidizer region and has a larger difference between constant and variable density solutions. In the numerical solution, as D decreases from complete combustion to extinction, the thickness of the reaction zone, which is centered at x_f, increases.
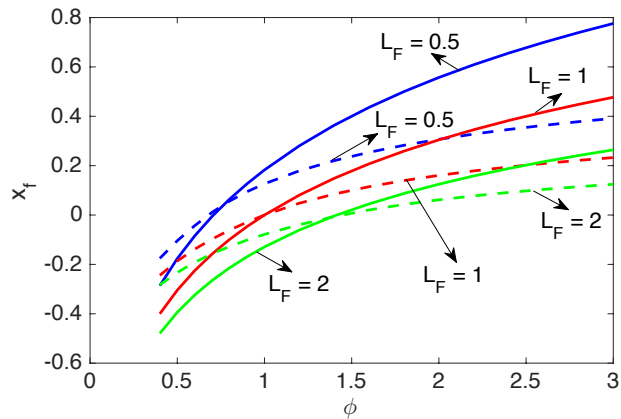
Figure 2.3: The dependence of the reaction sheet position x_f in the Burke-Schumann limit on the mixture strength ϕ, for various fuel Lewis numbers L_F, with oxidizer Lewis number $L_O = 1$. The dashed line represents the variable density solution, while the solid line represents the constant density solution.

18
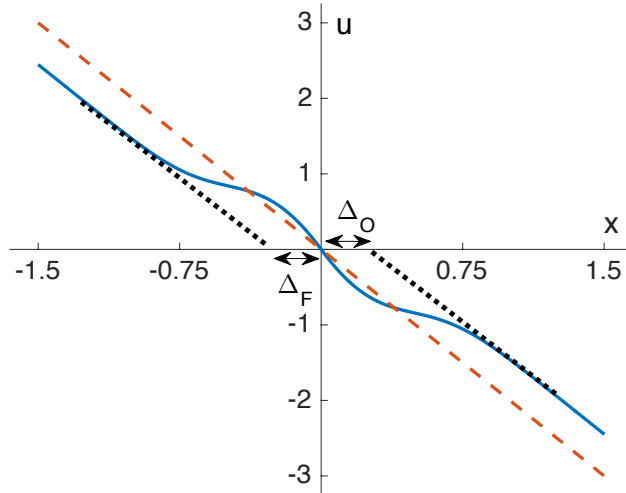
(a) $L_F = 1$, $L_O = 1$, $\phi = 1$, $D = 1000$ (Burke-Schumann)
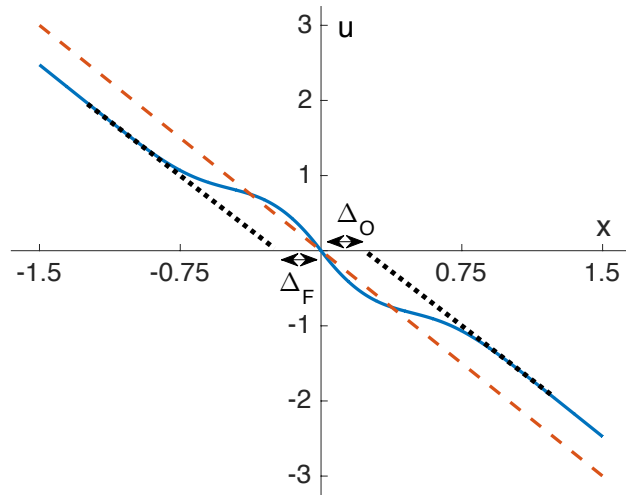
(b) $L_F = 1$, $L_O = 1$, $\phi = 1$, $D = 0.99$ (Extinction)

Figure 2.4: x-velocity comparison for constant and variable density formulations at complete combustion and extinction. The solid and dashed lines represent the asymptotic variable and constant density solution respectively. The dotted line represents the offset in the x-velocity due to density variation.

2.5.2   Flow field

The displacement effect of a premixed flame in stagnation point flow is studied by Eteng et al. [31]

A similar analysis is presented here for the counterflow diffusion flame. In Figure 2.4, we compare
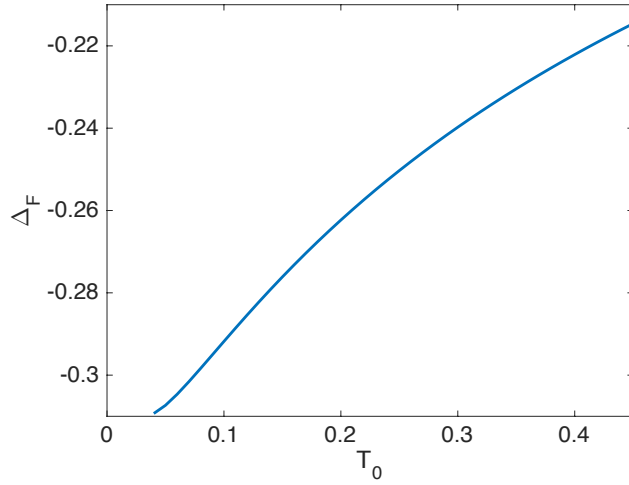
Figure 2.5: Δ_F as a function of heat release (as included in T_0) when $L_F = 1$, $L_O = 1$, $\phi = 1$.

the effect of density variation in the x-velocity at complete combustion and extinction. The offset due to density variation in the fuel and oxidizer region is characterized by Δ_F and Δ_O respectively. Δ_F is larger/smaller than Δ_O depending on the values of L_i and ϕ. For the case of unity Lewis number and mixture strength, Δ_F and Δ_O are equal due to symmetry. Both Δ_F and Δ_O are affected by changes in leakage functions (due to variations in Damkohler number) and heat release. It is evident from Figures 2.4(a) and 2.4(b) that as D approaches extinction, the decrease in flame temperature causes a reduction in the offset due to density variation. Similarly, as heat release is increased (or T_0 is decreased), there is a greater offset in the x-velocity as shown in Figure 2.5.

The variation in density can cause a jump in pressure as seen in Eqn (2.16). Due to the boundary condition in (2.14), when the reaction sheet is located at $x = 0$, there is no jump in pressure (as evident in Figure 2.6(a)). When the reaction sheet is not located at the center (as shown in Figure 2.6(b)), there is a jump in pressure whose magnitude corresponds to heat release. In Figure 2.7, it is evident that as heat release increases (or T_0 decreases), the jump in pressure also increases.
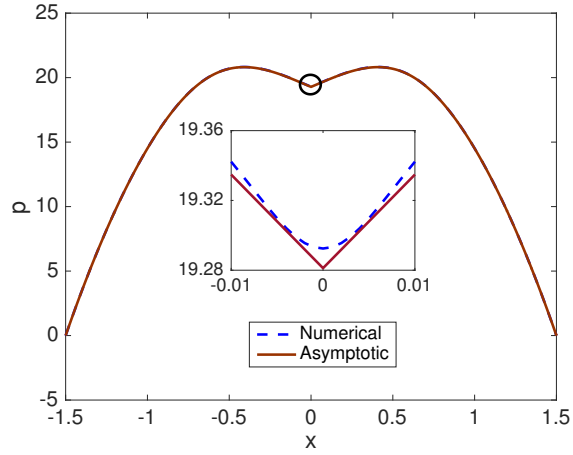
(a) $L_F = 1$, $L_O = 1$, $\phi = 1$
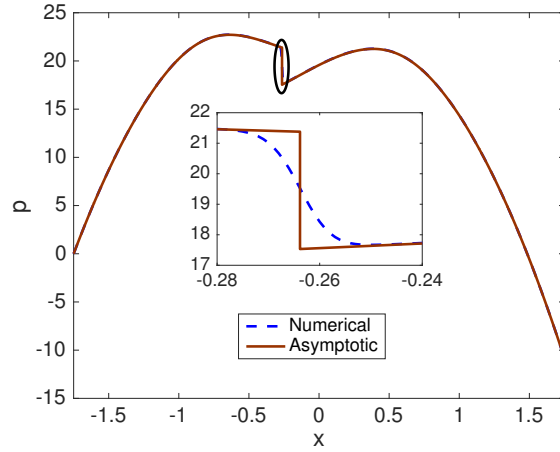
(b) $L_F = 1$, $L_O = 1$, $\phi = 0.4$

Figure 2.6: Asymptotic and numerical solutions of pressure profiles at complete combustion for various mixture strength.

2.5.3 Response curves: complete combustion to extinction

It is important to note that the extinction Damköhler number does not always correspond to the critical Damköhler number (the corresponding value of δ_c). They are only equal for the case of complete combustion unity Lewis numbers (or $h_f = 0$) when D is directly proportional to
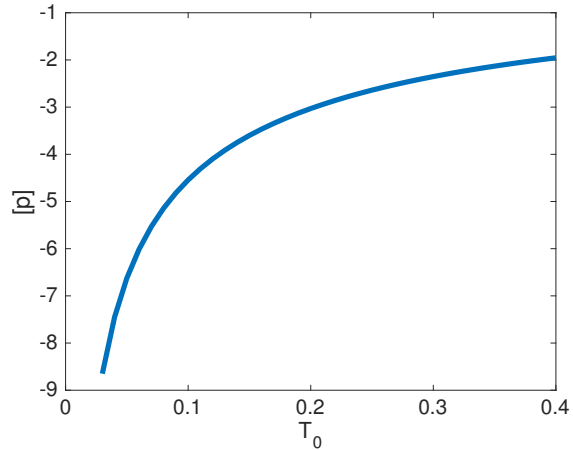
Figure 2.7: Pressure jump as a function of heat release (as included in T_0) when [$L_F = 1$, $L_O = 1$, $\phi = 0.4$

δ. Otherwise, there is an implicit relation between D and δ due to excess/deficiency in available enthalpy h_f at the reaction sheet (as seen in Eqn (2.21)). Therefore, Eqn (2.21) is used to iteratively solve for δ as a function of D or vice-versa. The relationship between D and δ is listed in [10] and discussed in [13].

The formulation adopted in this work is based on the general time-dependent and multi-dimensional asymptotic theory that exploits the limit of a large activation energy. Hence, if we increase θ, the difference between the exact (numerical) solution and asymptotic approximation should decrease as well. This should apply both to the constant and variable density formulations. In our analysis, we are primarily interested in how well the asymptotic solution predicts the extinction Damköhler number, flame temperature and flame position.

In Figure 2.8, we compare the asymptotic approximation with the numerical solution in both constant and variable density scenario for the configuration: $L_F = 1$, $L_O = 1$, $\phi = 1$ and $\theta = 20$. When the Lewis numbers and mixture strength are unity, the flame position, x_f is zero across all Damköhler number. Similarly, the fuel and oxidizer leakage are also equal to each other for unity Lewis numbers. It is clear that for both scenarios, the Burke-Schumann limit flame temperature is 0.634. For the constant density formulation, the asymptotic extinction Damköhler number is 0.27
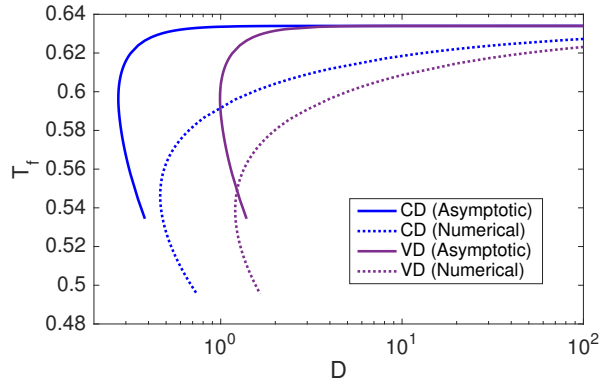
(a) Flame temperature
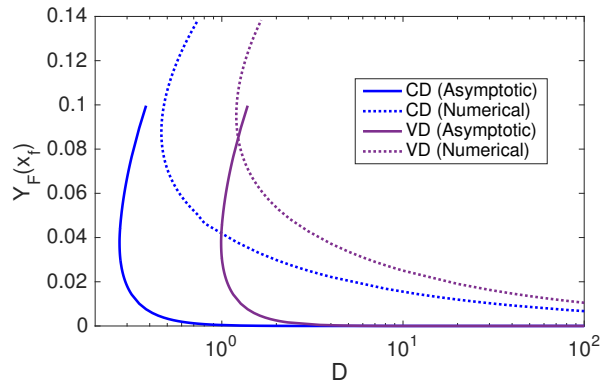
(b) Fuel leakage

Figure 2.8: Extinction profiles of uniform configuration with standard value for activation parameter ($L_F = 1$, $L_O = 1$, $\phi = 1$, $\theta = 20$).

with a flame temperature of 0.595 and a fuel leakage of 0.04; the numerical extinction Damköhler number is 0.46 with a flame temperature of 0.545 and a fuel leakage of 0.09. Similarly for the variable density formulation, the asymptotic extinction Damköhler number is 0.99 with the same flame temperature and fuel leakage as the constant density formulation; the numerical extinction Damköhler number is 1.2 with a flame temperature of 0.54 and a fuel leakage of 0.095. When comparing the asymptotic and numerical solutions, we see that extinction flame temperatures and fuel leakage match relatively well with a difference of 0.05. The asymptotic extinction Damköhler
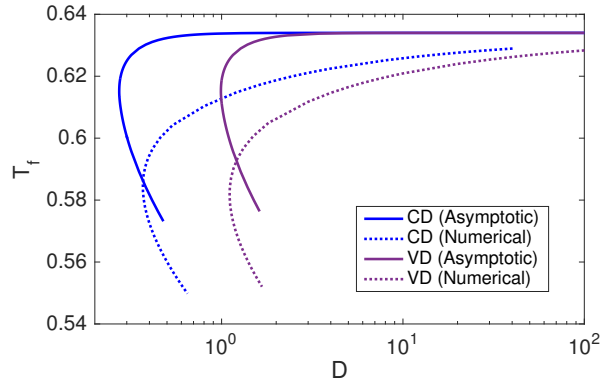
(a) Flame temperature
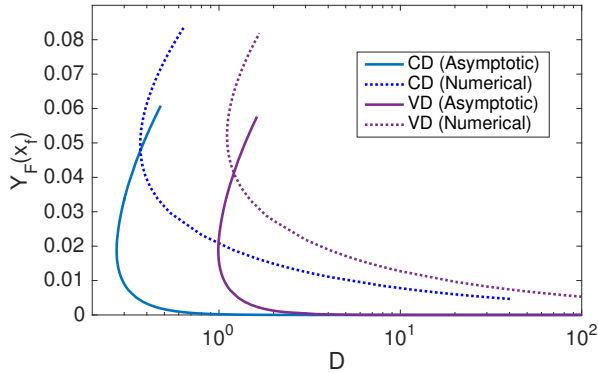
(b) Fuel leakage

Figure 2.9: Extinction profiles of uniform configuration with large activation parameter ($L_F = 1$, $L_O = 1$, $\phi = 1$, $\theta = 40$).

number is shown to match well with the numerical simulation.

In Figure 2.9, we compare the asymptotic approximation with the numerical solution for the configuration: $L_F = 1$, $L_O = 1$, $\phi = 1$ and $\theta = 40$. It is evident from the governing equations that the Burke-Schumann limit does not change with the activation energy parameter. For the constant density formulation, the asymptotic extinction Damköhler number is 0.27 with a flame temperature of 0.615 and a fuel leakage of 0.02; the numerical extinction Damköhler number is 0.37 with a flame temperature of 0.585 and a fuel leakage of 0.05. Similarly for the variable density formulation,

the asymptotic extinction Damköhler number is 0.99 with almost the same flame temperature and fuel leakage as the constant density formulation; the numerical extinction Damköhler number is 1.1 with a flame temperature of 0.58 and a fuel leakage of 0.053. When comparing the constant density asymptotic and numerical solutions, we see that extinction flame temperatures match relatively well with a slight difference of 0.03. Likewise, the asymptotic variable density extinction Damköhler number and flame temperature match well with the numerical solutions. This shows that as activation energy parameter increases, the difference between numerical and asymptotic solution decreases.

2.5.4   Lewis number variation

We are interested in comparing asymptotic approximation of extinction values to numerical simulation for large and small Lewis number in both constant and variable density formulations. In Figure 2.10, we present the solutions for large Lewis number scenario ($L_F = 2$). Unlike the unity Lewis number case, there is a small difference in Burke-Schumann flame temperature between the constant and variable density formulations. Since the numerical grid is discrete, the numerical flame position also progresses in discrete steps as Damköhler number varies. There is a small uncertainty associated with this approximation because the reaction zone is of finite length. For constant density formulation, the asymptotic extinction Damköhler number is 0.115 with a flame temperature of 0.535 and flame position of -0.1; the numerical extinction Damköhler number is 0.23 with a flame temperature of 0.48 and a flame position of -0.1. Similarly for variable density formulation, the asymptotic extinction Damköhler number is 0.43 with a flame temperature of 0.52 and a flame position of -0.06; the numerical extinction Damköhler number is 0.58 with a flame temperature of 0.465 and a flame position of -0.06. Once again, there is a good match between the asymptotic and numerical solutions of extinction Damköhler number for both formulations with the flame temperature having a difference on the order of θ^{-1}. The flame position is predicted well for both formulations.

In Figure 2.11, we analyze the asymptotic and numerical solutions for small Lewis number scenario ($L_F = 0.6$). The Burke-Schumann flame temperature decreases as Lewis number increases
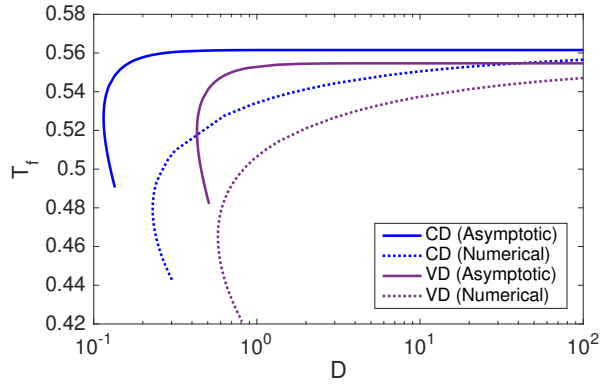
(a) Flame temperature
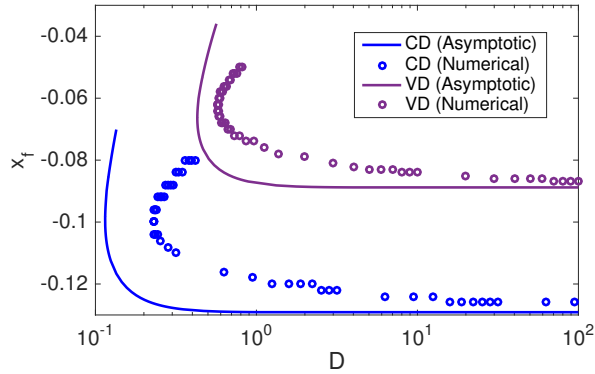
(b) Flame position

Figure 2.10: Extinction profiles of large Lewis number ($L_F = 2$, $L_O = 1$, $\phi = 1$, $\theta = 20$).

because of low species diffusivity. For constant density formulation, the asymptotic extinction Damköhler number is 0.55 with a flame temperature of 0.67 and flame position of 0.09; the numerical extinction Damköhler number is 0.83 with a flame temperature of 0.62 and a flame position of 0.09. Similarly for variable density formulation, the asymptotic extinction Damköhler number is 2.02 with a flame temperature of 0.68 and a flame position of 0.07; the numerical extinction Damköhler number is 2.26 with a flame temperature of 0.62 and a flame position of 0.07. As in the large Lewis number scenario, the variable density Burke-Schumann limit is slightly larger than the constant density formulation, which results in a lower extinction temperature. There is good agreement

26
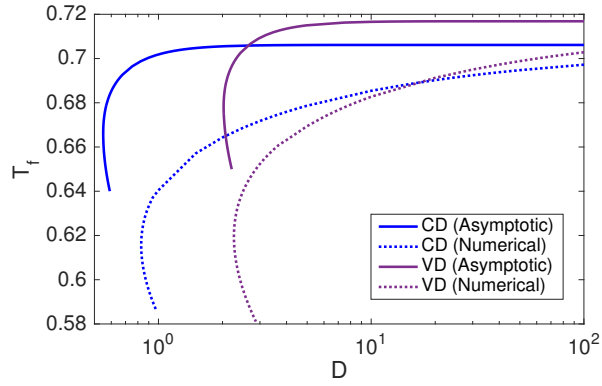
(a) Flame temperature
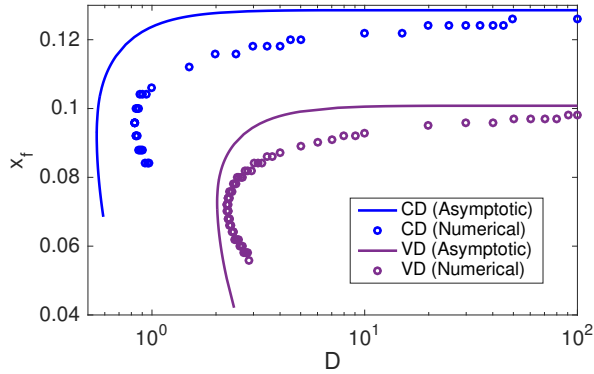
(b) Flame position

Figure 2.11: Extinction profiles of small Lewis number ($L_F = 0.6$, $L_O = 1$, $\phi = 1$, $\theta = 20$).

between the numerical and asymptotic flame position for both formulation.

2.5.5   Mixture strength variation

Finally, we analyze the effect of mixture strength variation on the comparison between numerical and asymptotic solutions for constant and variable density formulation. In Figure 2.12, the case of large mixture strength ($\phi = 4$) is analyzed. It is easily visible that, unlike Lewis number variation, there is no change in Burke-Schumann limit values between the two formulations. For constant density formulation, the asymptotic extinction Damköhler number is 0.043 with a flame temperature of

27
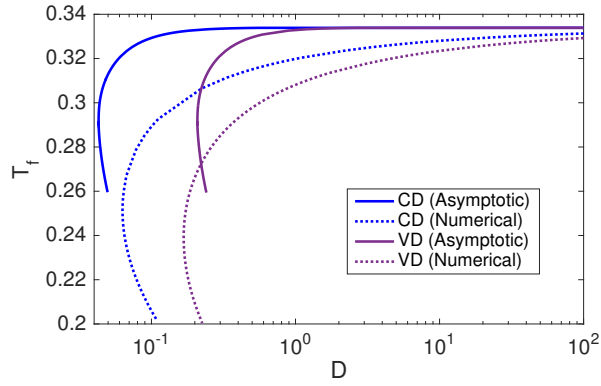
(a) Flame temperature
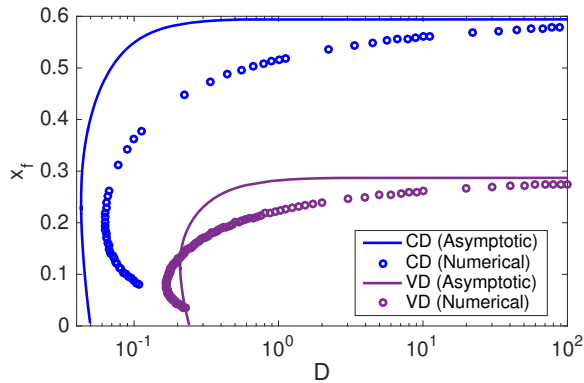
(b) Flame position

Figure 2.12: Extinction profiles of large mixture strength ($L_F = 1$, $L_O = 1$, $\phi = 4$, $\theta = 20$).

0.29 and flame position of 0.23; the numerical extinction Damköhler number is 0.063 with a flame temperature of 0.25 and a flame position of 0.20. Similarly for variable density formulation, the asymptotic extinction Damköhler number is 0.21 with a flame temperature of 0.29 and a flame position of 0.11; the numerical extinction Damköhler number is 0.17 with a flame temperature of 0.24 and a flame position of 0.08. It is evident that there is a strong consensus between numerical and asymptotic extinction values for constant and variable density formulations.

In Figure 2.13, the results for small mixture strength ($\phi = 0.4$) is presented. For constant density formulation, the asymptotic extinction Damköhler number is 0.58 with a flame temperature

28
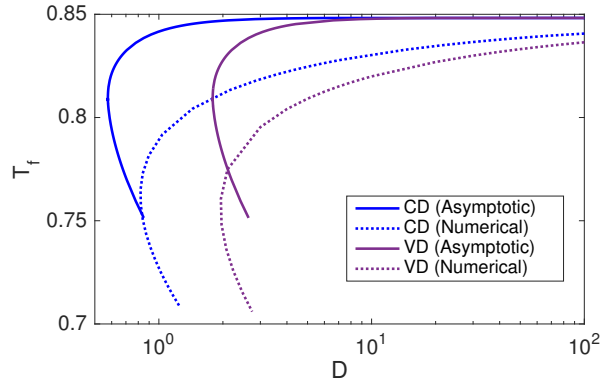
(a) Flame temperature
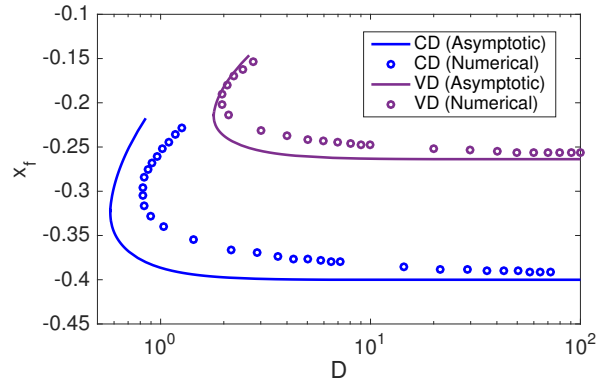
(b) Flame position

Figure 2.13: Extinction profiles of small mixture strength ($L_F = 1$, $L_O = 1$, $\phi = 0.4$, $\theta = 20$).

of 0.81 and flame position of -0.32; the numerical extinction Damköhler number is 0.82 with a flame temperature of 0.765 and a flame position of -0.30. For variable density formulation, the asymptotic extinction Damköhler number is 1.80 with a flame temperature of 0.81 and a flame position of -0.21; the numerical extinction Damköhler number is 1.95 with a flame temperature of 0.76 and a flame position of -0.2. The extinction flame temperature has an approximate difference of 0.05 between asymptotic and numerical solution. The match between the two formulations for extinction Damköhler number and flame position show similar trends as the previous cases.

2.6　Conclusion

The calculations presented in this chapter illustrates the effect of density variation on the extinction curves for a counterflow diffusion flame. The similarity solution was used for two-dimensional counterflow problem to simplify the governing equations. The values chosen lie within the range of methane-air combustion. We assume low Mach number approximation, which results in small pressure variations from the ambient state. The governing equations are analyzed using numerical solutions and asymptotic approximations. For numerical solutions, a fourth order Runge-Kutta is used for temporal discretization while a fourth-order central difference is used for spatial discretization. Since the solution is unstable near extinction point, we employed a version of continuation method to extend the response curve.

The asymptotic analysis of counterflow diffusion flame presented in this chapter is an application of the general theory presented by Cheatham and Matalon [13], which works under the assumption of large activation energy. We present the results of this theory in both constant and variable density formulation and compare it to numerical solutions for large/small Lewis numbers and mixture strengths. The asymptotic analysis of constant density formulation yields an analytical solution while the variable density formulation can only be computed by integrating the governing equations with appropriate jump conditions. In all considered cases, both formulations match almost exactly with each other at the complete combustion limit, which is used as a validation for the numerical procedure. It is worth nothing that the Burke-Schumann limit flame temperature for constant and variable density formulations differ only in the case of non-uniform Lewis numbers. The asymptotic extinction Damköhler number for both formulations matched well with the numerical solution. The extinction flame temperature and position also had good agreement between asymptotic and numerical solution for both formulations. Overall, the asymptotic analysis is shown to be relatively accurate for wide array of parameters.

Chapter 3

Modeling Extinction of Diffusion flames in Titanium-Boron Combustion

3.1 Introduction

A prominent example we have chosen to highlight in our following discussion, is nano-composite made from titanium and boron that reacts to make titanium diboride. The overall equilibrium reaction of titanium (Ti) and boron (B) to make titanium diboride (TiB_2), is

$$Ti + 2B \rightarrow TiB_2 \,. \tag{3.1}$$

with a heat of reaction of approximately -323.8 KJ/mol [5]. In the wider class of metal/metal oxide and metal/intermetallic pairs, this is a very high energy release reaction. The Ti/2B system offers an advantages over metal/metal oxide thermites, since it is possible to mix the reactants and make nano-scale composites safely without reaction, and consequently make a material that remains essentially inert until activated. Trunov et al. [32] describes the manufacture of nano-composite mixtures produced by arrested reactive milling. titanium and boron powders are placed in a ball mill and blended at cold temperature to prevent reaction while making the finely blended composite. Photomicrographs of a section in a region of the blended nano-composite shows fully dense regions of titanium adjacent to regions of boron at the 1 micron length scale. However even at that scale, one still observes distinct interfaces of pure titanium next to regions of pure boron. Mixing by ball milling produces large increases of the titanium/boron reaction surface that is likely orders of magnitudes larger than prior to ball milling.

Rogachev [33] identifies the nature of three different reaction waves that occur in multilayer

nanofilms. Self-propagating reaction waves (or self-sustained high-temperature synthesis SHS waves - 0.1 to 10 m s^{-1}) are observed in films separated from an inert substrate and the layer thickness is heavily dependent on the combustion rate. Very fast reaction waves (10 - 100 m s^{-1}) are initiated by a laser pulse in films deposited on a cold substrate. Slow reaction waves (less than 0.01 m s^{-1}) occur in films with thickness smaller than a micrometer and heated together with substrate. Adams and Weihs [34] [35] present an overview of current developments in the theoretical and experimental investigations into reactive multilayered energetic materials. They summarize the efforts on the effect of bilayer thickness on ignition and combustion velocities of many energetic compounds, including Ti/2B. Weihs also explores the experimental techniques to measure atomic diffusion in condensed phase reactive materials.

Reeves et al. [36] studied the effect of various gas environments and bilayer thickness in high-purity Ti/2B reactive multilayers. He found that for relatively large bilayer thickness samples (greater than 857 nm), the reaction failed to occur in very low pressure, while smaller thickness samples did not show such dependency on the surrounding air pressure. He also found that the oxidation of these thicker foils was able to augment intermixing between the Ti and B layers, primarily due to the reactivity of Ti layers with environmental gas.

Sraj et al. [37] studied the response of Ni/Al multilayered composites to shock compression. A simplified approach was adopted in which CTH calculations were first applied to estimate the impact of shock heating. The resulting predictions were then used to initialize the computations of the transient, adiabatic, behavior of the reaction initiated by the shock heating. In particular, the analysis aimed at investigating the effects of the bilayer thickness, shock velocity and orientation on the evolution of reaction and consumption of reactants. Zhao et al. [38] approaches the problem from a molecular dynamics perspective by analyzing the effect of porosity on initiation and energy release rate in Ni/Al nanolaminates.

Our modeling approach differs from the ones presented above in that we analyze the effect of a planar flame created through material deformation at high temperatures and low pressure. Also unlike the previous work, we have chosen to simultaneously analyze both the mechanical and chemical reactions. This inclusion of formation of products makes this a three-species model, while

32

Sraj et al. [37] considered only a two species model.

The basic formulation of diffusion that most literature follow is:

$$\frac{\partial C}{\partial t} = \nabla \cdot (D \nabla C) \tag{3.2}$$

$$\frac{\partial H}{\partial t} = K \frac{\partial^2 T}{\partial^2 x} - \frac{\partial Q}{\partial t} \tag{3.3}$$

with an atomic diffusion, D, given as:

$$D(T) = D_0 \exp \left(-\frac{E}{RT} \right) \tag{3.4}$$

Where, C describes mixing as a time dependent conserved scalar, H is the section averaged enthalpy and Q is the chemical energy source term.

Different types of nano-composite materials were burned in a Methane-air flame and we assessed the effect of the additives on the output of the resulting combustion products. Trunov et al. [32] found that the very high temperatures created by the burning of stoichiometric Ti/2B nano-composite was the most effective in the generation of heated gas products. Their work suggests that the Ti/2B nano-composite might be useful as an active ingredient in composite explosive fills that could be used for biocidal agent defeat. The basic concept for agent defeat is to add the Ti/2B nano-composite as an additive or fill along with another component, such as lithium perchlorate, that at high temperature evolves to a lethal biocidal gas like chlorine, which is able to defeat biological toxins and kill spores. Along these same lines, Glumac et al. [5] carried out a series of experiments in which Ti/2B powders and Ti/2B nano-composites. Ti/2B powders and Ti/2B nano-composites were pressed into pellets that were shock initiated with explosives. The quasi-static pressure in a small blast chamber was measured to assess the energy release output of pressed pellets. Once again, in a selection of variants of pressed pellets of titanium and boron mixtures that were mixed by different means, the stoichiometric, milled reactive Ti/2B nano-composite was the best performer with the highest observed temperatures and pressure outputs.

The engineering design of novel energetic and reactive materials requires that we have a funda-

33

mental understanding of the processes of chemical reactions of condensed phase reactants that are initially separated. In all the cases discussed above, the energetic material is a designed material where the micro scale features are defined by the manufacture of the material. The individual components are generally inert, and only react when they are exposed to thermal heating and or shock stimulus that leads to a chemical reaction at interfaces of adjacent components. Almost always the initial chemical reaction first takes place in the condensed phase, most often in a liquid melt and in an environment where the characteristic thermal diffusivity in the surrounding material is large compared to the mass diffusivity of the reactants. The reaction products can be gaseous or liquid but they evolve at least initially in the condensed phase environment.

3.1.1   Basic approach and summary

In this chapter we analyze a steady diffusion flame that arises at the interfaces of two condensed phase reactant streams that form an opposed counterflow. We assume that the flow is due to deformation from compaction or local heating and thermal expansion processes in the microscale environment of composite energetic materials. Figure 3.1 shows the planar configuration of the reaction front. Because of our interest in the applications described above, we have focused on the Ti/B system and describe it simply with three components; two reactants Ti and B, and the product TiB_2. The equation of state of the three components, and the formulation that defines the equilibrium equation of state of the mixture, is based on multicomponent thermodynamics formulations that are similar to those used in the study of metallurgy and materials [39]. As such, the formulation is based on Gibbs thermodynamic potentials where one assumes that at each point of the condensed phase mixture, there is a single stress state and temperature.

We make some simplifying assumptions in this first work. The chemical reactions take place at nearly constant pressure so that the stress is spherical and hence is represented by the hydrostatic pressure. Each isolated component is assumed to have its own distinct reference density, and we neglect thermal expansion in the components. This is consistent with the notion that the change in composition due to reaction is much larger than changes due to thermal expansion. As a result the mechanical equation of state for the mixture takes a simple form whereby the specific volume

of the mixture is simply a sum of the intrinsic densities weighted with the mass fraction of each component. This form of the mechanical equation of state stands in contrast with that for a mixture of reacting gases that is a relation between the specific volume, pressure, temperature and mass fractions. The diffusion model for the components is derived from an effective Fickean diffusion formulation as described by Curtiss [40] and Curtiss and Bird [41], whereby a Maxwell-Stefan law formulated in terms of binary diffusivities is expressed as a generalized Fick diffusion law with symmetric diffusion coefficients. The resulting diffusion coefficients used in our model are then chosen to be consistent with experiments reported in [32].

In this study we analyze the effect of density variation and diffusion on the reaction between titanium and boron. The microscale length and relative motion between the reactants provide the characteristic scales, and in particular the representative strain rate that determines the conditions that differentiate between vigorous and weak burning between titanium and boron. This is addressed first under the assumption of constant mixture density, which enables the construction of an analytical solution. We use that solution to estimate the binary diffusion coefficients required for a given adiabatic flame temperature, as well as estimate the strain rates that leads to extinction in reaction for the counterflow geometry. We then address the general case when the density of the mixture varies as it reflects the local composition of the mixtures. When comparing the constant and variable density formulation, the change in extinction strain rate is minimal. The viscous transport is neglected in our formulation during this first attempt and will be considered in the future.

3.2   Formulation

The counterflow geometry under consideration is shown in Figure 3.1, where far to the left (state 1) there is only titanium and far to the right (state 2) there is only boron; the intrinsic densities are denoted by $\hat{\rho}_{1_0}$ and $\hat{\rho}_{2_0}$, respectively. Under steady conditions, the material deformation may be described by a velocity field $\mathbf{v} = \{u(x), y\,\bar{\vartheta}(x)\}$. This "similarity solution" implies that the pressure gradient in the transverse direction y is necessarily linear and admits planar combustion

35

fronts such that all state variables, the mass fractions Y_i, the density ρ, and temperature T, are functions of x alone. The constituents in the combustion zone include titanium of mass fraction Y_1, boron of mass fraction Y_2, and titanium diboride products of mass fraction Y_3. An overall conservation of mass implies that

$$Y_1 + Y_2 + Y_3 = 1\,. \tag{3.5}$$

The conductivity k and specific heat (at constant pressure) c_p of the mixture (defined as mass-weighted averages) are, in general, functions of temperature but for simplicity will be considered here as constants. Finally, the chemical reaction (3.1) between Ti and B is assumed to proceed at a rate

$$\omega = \mathcal{B} Y_1 Y_2^2 \, e^{-E/RT} \tag{3.6}$$

where E is the activation energy, R is the universal gas constant and $\mathcal{B}$ is an appropriately defined pre-exponential factor. Diffraction reaction orders could be considered without difficulty; the present form that simplifies the reaction to one-step process was made for simplicity.

3.2.1 Conservation equations

The governing equations, describing conservation of mass, momentum, and energy under steady conditions simplify to

$$\frac{d}{dx}(\rho u) + \rho\,\bar{\vartheta} = 0 \tag{3.7}$$

$$\rho u \frac{d\bar{\vartheta}}{dx} + \rho\,\bar{\vartheta}^2 = C \tag{3.8}$$

$$\rho c_p u \frac{dT}{dx} - K \frac{d^2 T}{dx^2} = Q\omega \tag{3.9}$$

$$\rho u \frac{dY_1}{dx} + \frac{d}{dx}(\rho Y_1 V_1) = -W_1 \omega \tag{3.10}$$

$$\rho u \frac{dY_2}{dx} + \frac{d}{dx}(\rho Y_2 V_2) = -2 W_2 \omega \tag{3.11}$$

36
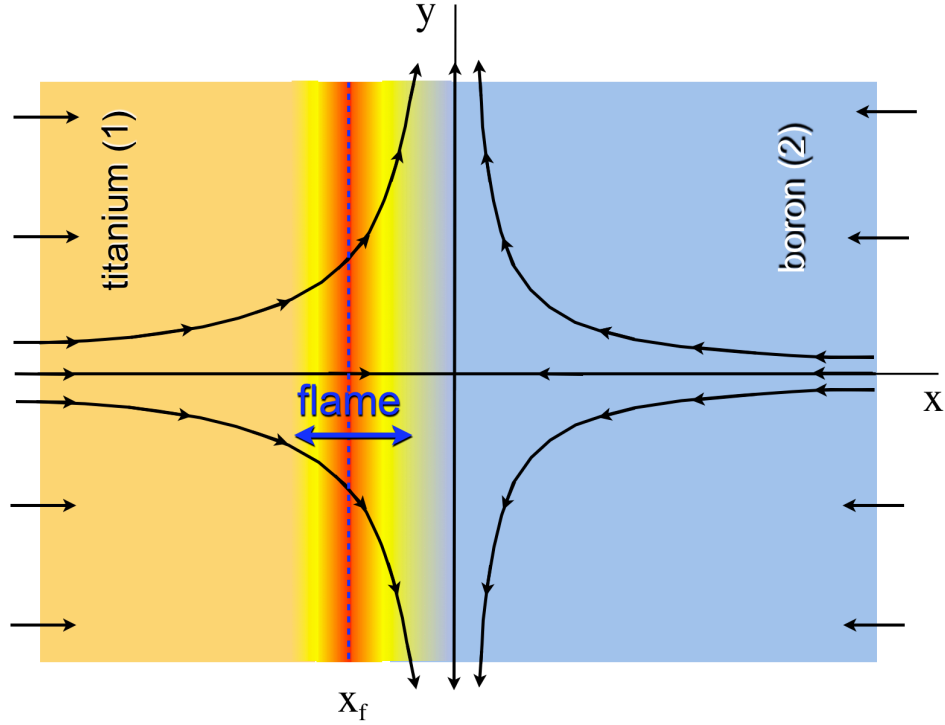
Figure 3.1: Schematic of the condensed phase counterflow diffusion flame, with titanium entering from the left and boron from the right.

where V_i, W_i stand for the diffusion velocity and molecular weight of species i, and Q is the overall heat release. As noted earlier, the pressure gradient in the transverse y-direction is linear, given by $\partial p / \partial y = -Cy$, where C is a constant determined by the far field conditions. Equation (3.8) implies that there is a relation between the densities and strain rates at the far ends, such that

$$\hat{\rho}_{1_0} \epsilon_1^2 = \hat{\rho}_{2_0} \epsilon_2^2 = C \,. \tag{3.12}$$

Hence the motion of the reactants impinging on each other is characterized by a single strain rate ϵ (in units of 1/s) which we choose as $\epsilon = \epsilon_1/2$; the factor of 2 is introduced solely to facilitate the form of the analytical asymptotic solution described below. The axial dependence of the pressure can be obtained a-posteriori by solving the x-component of the momentum equation (not written above).

37

Equations (3.7)-(3.11) must be supplemented with constitutive relations for the diffusion velocities and an equation of state for the mixture. Starting with the assumption that the Gibbs free energy of each component of the mixture can be summed, the Gibbs potential for the mixture which is a function of the pressure temperature and mixture composition is

$$g = \sum_{i=1}^{3} g_i(p, T) Y_i \,, \tag{3.13}$$

where the energies related to mixing has been neglected. The specific volume $v = 1/\rho$ of the mixture and individual components are given by the thermodynamic relation:

$$v = \left. \frac{\partial g}{\partial p} \right|_{T, Y_i} \quad \text{and} \quad v_i = \left. \frac{\partial g_i}{\partial p} \right|_{T} \,, \tag{3.14}$$

where v_i are the partial volumes or volume of the components. This leads to

$$v = \sum_{i=1}^{3} v_i(p, T) Y_i \,. \tag{3.15}$$

which is the mechanical equation of state for the mixture. If we further assume that the volume change under variation of pressure is small and we neglect the effect on temperature as well, then the component volumes v_i can be approximated by their reference values $\hat{v}_{i0}$. By expressing eqn (4.9) in terms of the densities, the mechanical equation of state becomes

$$\rho^{-1} = \sum_{i=1}^{3} Y_i \, \hat{\rho}_{i_0}^{-1} \tag{3.16}$$

where $\hat{\rho}_{i_0}$ is the intrinsic density and $\hat{\rho}_{i_0}^{-1}$ is the intrinsic specific volume, of the species i. Using (3.5) the equation of state simplifies to

$$\frac{1}{\rho} = \frac{1}{\hat{\rho}_{3_0}} + \left(\frac{1}{\hat{\rho}_{1_0}} - \frac{1}{\hat{\rho}_{3_0}} \right) Y_1 + \left(\frac{1}{\hat{\rho}_{2_0}} - \frac{1}{\hat{\rho}_{3_0}} \right) Y_2 \,. \tag{3.17}$$

The material properties, far to the left (denoted by subscript 1) and far to the right (denoted by subscript 2), are uniform such that the boundary conditions associated with (3.7)-(3.11) are:

38

$$du/dx \sim -2\epsilon \qquad \text{as } |x| \to \infty \,, \tag{3.18}$$

$$\rho = \hat{\rho}_{1_0}, \ \ Y_1 = 1, \ \ Y_2 = 0, \ \ T = T_\infty \qquad \text{as } x \to -\infty \,, \tag{3.19}$$

$$\rho = \hat{\rho}_{2_0}, \ \ Y_1 = 0, \ \ Y_2 = 1, \ \ T = T_\infty \qquad \text{as } x \to +\infty \,. \tag{3.20}$$

Note that there is no need to specify a condition for $\bar{\vartheta}$, because it is obtained by differentiation

$$\bar{\vartheta} = -\frac{1}{\rho}\frac{d}{dx}(\rho u) \,. \tag{3.21}$$

When note that density variations remain small, the equation of state (3.17) can be effectively replaced by $\rho =$constant, and the velocity field everywhere is given by

$$u = -2\epsilon x \,, \qquad v = 2\epsilon y \,. \tag{3.22}$$

The problem reduces to the reaction-diffusion system (3.9)-(3.11). The constant-density approximation will be used for simplicity in the asymptotic description described below. In general, variations in the density affect the overall velocity fields. In Section 3.5, numerical computations are carried out in order to assess the importance of density variations in condensed-phase combustion.

3.2.2 Diffusion

The most common expressions used for multi-component diffusion are the Maxwell-Stefan (MS) relations, [42]

$$\nabla X_i = \sum_j \frac{X_i X_j}{\mathscr{D}_{ij}}(\mathbf{V}_j - \mathbf{V}_i) \,, \tag{3.23}$$

where X_i is the molar fraction and $\mathbf{V_i}$ is the diffusion velocity vector of species i, $\mathscr{D}_{ij} = \mathscr{D}_{ji}$ is the binary diffusivity of a pair of species (i, j), and the summation is taken over all species present.

Although this relation was derived for a dilute ideal gas mixture, it has been often applied to condensed phase media [43].

The use of the Maxwell-Stefan relations is quite complicated because the diffusion velocities $\mathbf{V}_i$ are not expressed explicitly in terms of the concentration gradients. A common practice is to use the generalized Fick equations

$$\mathbf{V}_i = \sum_j \mathbb{D}_{ij} \nabla X_j \tag{3.24}$$

where coefficients $\mathbb{D}_{ij}$ referred to as *Fick diffusivities* are related to the binary diffusivities $\mathscr{D}_{ij}$, but they are concentration dependent and may not necessarily be all positive. They must satisfy the constraints

$$\mathbb{D}_{ij} = \mathbb{D}_{ji}, \quad \text{for all } i, j, \qquad \sum_i \mathbb{D}_{ij} Y_i = 0 \quad \text{for all } j.$$

The relation between the Fick diffusivities $\mathbb{D}_{ij}$ and binary diffusivities $\mathscr{D}_{ij}$ for a ternary mixture are given by

$$\mathbb{D}_{11} = -\frac{\dfrac{(Y_2 + Y_3)^2}{X_1\,\mathscr{D}_{23}} + \dfrac{Y_2{}^2}{\mathscr{D}_{13}\,X_2} + \dfrac{Y_3{}^2}{X_3\,\mathscr{D}_{12}}}{\dfrac{X_1}{\mathscr{D}_{12}\,\mathscr{D}_{13}} + \dfrac{X_2}{\mathscr{D}_{12}\,\mathscr{D}_{23}} + \dfrac{X_3}{\mathscr{D}_{13}\,\mathscr{D}_{23}}} \tag{3.25}$$

$$\mathbb{D}_{22} = -\frac{\dfrac{(Y_1 + Y_3)^2}{\mathscr{D}_{13}\,X_2} + \dfrac{Y_3{}^2}{X_3\,\mathscr{D}_{12}} + \dfrac{Y_1{}^2}{X_1\,\mathscr{D}_{23}}}{\dfrac{X_1}{\mathscr{D}_{12}\,\mathscr{D}_{13}} + \dfrac{X_2}{\mathscr{D}_{12}\,\mathscr{D}_{23}} + \dfrac{X_3}{\mathscr{D}_{13}\,\mathscr{D}_{23}}} \tag{3.26}$$

$$\mathbb{D}_{33} = -\frac{\dfrac{(Y_2 + Y_1)^2}{X_3\,\mathscr{D}_{12}} + \dfrac{Y_1^2}{X_1\,\mathscr{D}_{23}} + \dfrac{Y_2^2}{X_2\,\mathscr{D}_{13}}}{\dfrac{X_1}{\mathscr{D}_{12}\,\mathscr{D}_{13}} + \dfrac{X_2}{\mathscr{D}_{12}\,\mathscr{D}_{23}} + \dfrac{X_3}{\mathscr{D}_{13}\,\mathscr{D}_{23}}} \tag{3.27}$$

$$\mathbb{D}_{12} = \frac{\dfrac{Y_1(Y_2 + Y_3)}{X_1\,\mathscr{D}_{23}} + \dfrac{Y_2(Y_1 + Y_3)}{X_2\,\mathscr{D}_{13}} - \dfrac{Y_3^2}{X_3\,\mathscr{D}_{12}}}{\dfrac{X_1}{\mathscr{D}_{12}\,\mathscr{D}_{13}} + \dfrac{X_2}{\mathscr{D}_{12}\,\mathscr{D}_{23}} + \dfrac{X_3}{\mathscr{D}_{13}\,\mathscr{D}_{23}}} \tag{3.28}$$

$$\mathbb{D}_{13} = \frac{\dfrac{Y_3(Y_2 + Y_1)}{X_3 \mathscr{D}_{12}} + \dfrac{Y_1(Y_2 + Y_3)}{X_1 \mathscr{D}_{23}} - \dfrac{Y_2^2}{X_2 \mathscr{D}_{13}}}{\dfrac{X_1}{\mathscr{D}_{12}\mathscr{D}_{13}} + \dfrac{X_2}{\mathscr{D}_{12}\mathscr{D}_{23}} + \dfrac{X_3}{\mathscr{D}_{13}\mathscr{D}_{23}}} \tag{3.29}$$

$$\mathbb{D}_{23} = \frac{\dfrac{Y_2(Y_1 + Y_3)}{X_2 \mathscr{D}_{13}} + \dfrac{Y_3(Y_2 + Y_1)}{X_3 \mathscr{D}_{12}} - \dfrac{Y_1^2}{X_1 \mathscr{D}_{23}}}{\dfrac{X_1}{\mathscr{D}_{12}\mathscr{D}_{13}} + \dfrac{X_2}{\mathscr{D}_{12}\mathscr{D}_{23}} + \dfrac{X_3}{\mathscr{D}_{13}\mathscr{D}_{23}}} \tag{3.30}$$

Converting eq. (3.24) from mole to mass fraction yields:

$$Y_i V_i = a_i \nabla Y_1 + b_i \nabla Y_2, \quad i = 1, 2 \tag{3.31}$$

where

$$a_1 = \frac{W_1(Y_2 + Y_3)(-Y_2 W_3 - W_2 + Y_2 W_2)\mathscr{D}_{13}\mathscr{D}_{12} + Y_1 Y_2 W_2(W_1 - W_3)\mathscr{D}_{23}\mathscr{D}_{12}}{Y_1 W_2 W_3 \mathscr{D}_{23} + Y_2 W_1 W_3 \mathscr{D}_{13} + Y_3 W_2 W_1 \mathscr{D}_{12}} \\ - \frac{W_3 Y_1(W_2 - Y_2 W_2 + Y_2 W_1)\mathscr{D}_{23}\mathscr{D}_{13}}{Y_1 W_2 W_3 \mathscr{D}_{23} + Y_2 W_1 W_3 \mathscr{D}_{13} + Y_3 W_2 W_1 \mathscr{D}_{12}}$$

$$b_1 = -\frac{Y_1 W_1(Y_2 + Y_3)(W_2 - W_3)\mathscr{D}_{13}\mathscr{D}_{12} + Y_1 W_2(-W_1 + Y_1 W_1 - W_3 Y_1)\mathscr{D}_{23}\mathscr{D}_{12}}{Y_1 W_2 W_3 \mathscr{D}_{23} + Y_2 W_1 W_3 \mathscr{D}_{13} + Y_3 W_2 W_1 \mathscr{D}_{12}} \\ + \frac{Y_1 W_3(-Y_1 W_2 - W_1 + Y_1 W_1)\mathscr{D}_{23}\mathscr{D}_{13}}{Y_1 W_2 W_3 \mathscr{D}_{23} + Y_2 W_1 W_3 \mathscr{D}_{13} + Y_3 W_2 W_1 \mathscr{D}_{12}}$$

$$a_2 = -\frac{Y_2 W_1(-W_2 + Y_2 W_2 - Y_2 W_3)\mathscr{D}_{13}\mathscr{D}_{12} + Y_2 W_2(Y_1 + Y_3)(W_1 - W_3)\mathscr{D}_{23}\mathscr{D}_{12}}{Y_1 W_2 W_3 \mathscr{D}_{23} + Y_2 W_1 W_3 \mathscr{D}_{13} + Y_3 W_2 W_1 \mathscr{D}_{12}} \\ - \frac{Y_2 W_3(-Y_2 W_2 + Y_2 W_1 + W_2)\mathscr{D}_{23}\mathscr{D}_{13}}{Y_1 W_2 W_3 \mathscr{D}_{23} + Y_2 W_1 W_3 \mathscr{D}_{13} + Y_3 W_2 W_1 \mathscr{D}_{12}}$$

$$b_2 = \frac{Y_2 Y_1 W_1(-W_3 + W_2)\mathscr{D}_{13}\mathscr{D}_{12} + W_2(Y_1 + Y_3)(-W_1 + Y_1 W_1 - Y_1 W_3)\mathscr{D}_{23}\mathscr{D}_{12}}{Y_1 W_2 W_3 \mathscr{D}_{23} + Y_2 W_1 W_3 \mathscr{D}_{13} + Y_3 W_2 W_1 \mathscr{D}_{12}}$$
$$+ \frac{Y_2 W_3(-Y_1 W_2 - W_1 + Y_1 W_1)\mathscr{D}_{23}\mathscr{D}_{13}}{Y_1 W_2 W_3 \mathscr{D}_{23} + Y_2 W_1 W_3 \mathscr{D}_{13} + Y_3 W_2 W_1 \mathscr{D}_{12}}$$

The species equations (3.10)-(3.11) can then be written as

$$\rho u \frac{dY_1}{dx} + \frac{d}{dx}\left[\rho\left(a_1 \frac{dY_1}{dx} + b_1 \frac{dY_2}{dx}\right)\right] = -W_1 \omega, \tag{3.32}$$

$$\rho u \frac{dY_2}{dx} + \frac{d}{dx}\left[\rho\left(a_2 \frac{dY_1}{dx} + b_2 \frac{dY_2}{dx}\right)\right] = -2W_2 \omega. \tag{3.33}$$

A simplification that can be used for analytical convenience result from assuming equal molecular weights $W_1 = W_2 = W_3$, then

$$a_1 = -\mathscr{D}_{13}\frac{\mathscr{D}_{12} + (\mathscr{D}_{23} - \mathscr{D}_{12})Y_1}{(\mathscr{D}_{23} - \mathscr{D}_{12})Y_1 + (\mathscr{D}_{13} - \mathscr{D}_{12})Y_2 + \mathscr{D}_{12}}$$

$$b_1 = \frac{\mathscr{D}_{23}(\mathscr{D}_{12} - \mathscr{D}_{13})Y_1}{(\mathscr{D}_{23} - \mathscr{D}_{12})Y_1 + (\mathscr{D}_{13} - \mathscr{D}_{12})Y_2 + \mathscr{D}_{12}}$$

$$a_2 = \frac{\mathscr{D}_{13}(\mathscr{D}_{12} - \mathscr{D}_{23})Y_2}{(\mathscr{D}_{23} - \mathscr{D}_{12})Y_1 + (\mathscr{D}_{13} - \mathscr{D}_{12})Y_2 + \mathscr{D}_{12}}$$

$$b_2 = -\mathscr{D}_{23}\frac{\mathscr{D}_{12} + (\mathscr{D}_{13} - \mathscr{D}_{12})Y_2}{(\mathscr{D}_{23} - \mathscr{D}_{12})Y_1 + (\mathscr{D}_{13} - \mathscr{D}_{12})Y_2 + \mathscr{D}_{12}}$$

3.3 Asymptotic Solution - the Burke-Schumann limit

We first present analytical results in the limit of infinitely fast chemical reaction, which is known as the Burke-Schumann limit. The solutions obtained in this limit provide a simple illustration of the flame structure. A characteristic time may be defined based on a characteristic length between particles divided by a typical local microscale flow velocity due to deformation. The inverse of this time is the characteristic strain rate, and the fast chemistry limit corresponds to weak strain

rates.Therefore, the corresponding Damköhler number, or ratio of the flow-to-chemistry time scales is large. Although asymptotic methods that span a wider range of strain rates including flame extinction are available for the related gaseous problem [13], their extension to energetic materials will be discussed in a future publication. Here we rely on numerical methods to examine the dependence of the solution on the strain rate for steady combustion.

In the fast chemistry limit the chemical reaction occurs along a sheet, say at $x = x_f$, where the two reactants are in contact. Elsewhere, the chemical reaction is negligibly small and we are left solving the energy and species equations on either side of the sheet, with $\omega = 0$. The flame sheet separates a region where there is only titanium $(x < x_f)$, from a region where there is only boron $(x > x_f)$. Hence for $x < x_f$, since $Y_2 = 0$, we find

$$
a_1 = -\mathscr{D}_{13}\,, \qquad\qquad b_1 = \frac{\mathscr{D}_{23}(\mathscr{D}_{12} - \mathscr{D}_{13})Y_1}{\mathscr{D}_{23}Y_1 + \mathscr{D}_{12}(1 - Y_1)}\,,
$$

$$
a_2 = 0\,, \qquad\qquad b_2 = -\frac{\mathscr{D}_{23}\mathscr{D}_{12}}{\mathscr{D}_{23}Y_1 + \mathscr{D}_{12}(1 - Y_1)}\,.
$$

Similarly for $x > x_f$, since $Y_1 = 0$, we find

$$
a_1 = -\frac{\mathscr{D}_{13}\mathscr{D}_{12}}{\mathscr{D}_{13}Y_2 + \mathscr{D}_{12}(1 - Y_2)}\,, \qquad\qquad b_1 = 0\,,
$$

$$
a_2 = \frac{\mathscr{D}_{13}(\mathscr{D}_{12} - \mathscr{D}_{23})Y_2}{\mathscr{D}_{13}Y_2 + \mathscr{D}_{12}(1 - Y_2)}\,, \qquad\qquad b_2 = -\mathscr{D}_{23}\,.
$$

We note parenthetically that the simplification of the coefficients a_i, b_i applies even for unequal molecular weights. All variables must be continuous at the flame sheet, but the mass and energy fluxes must satisfy the jump relations

$$
\frac{\alpha}{Q/c_p}\left[\frac{dT}{dx}\right] = \frac{1}{W_1}\left[a_1\frac{dY_1}{dx} + b_1\frac{dY_2}{dx}\right] = \frac{1}{2W_2}\left[a_2\frac{dY_1}{dx} + b_2\frac{dY_2}{dx}\right]\,, \tag{3.34}
$$

43

obtained by integrating (3.9) and (3.32)-(3.33) across the sheet. Here the square brackets denote the jump, namely the difference between the values on the burned and unburned sides. These conditions imply that the fluxes of titanium and boron towards the flame sheet are in stoichiometric proportions, and they specify the proportion of heat from the total heat released conducted to one or the other side of the sheet.

For simplicity in this section, we have also adopted the constant density approximation. The mathematical problem on either side of the flame sheet then consists of

$$2\epsilon x \frac{dT}{dx} + \alpha \frac{d^2 T}{dx^2} = 0 \qquad \text{for } x \lessgtr x_f \qquad (3.35)$$

$$2\epsilon x \frac{dY_1}{dx} + \mathscr{D}_{13} \frac{d^2 Y_1}{dx^2} = 0 \qquad \text{for } x < x_f \qquad (3.36)$$

$$Y_1 \equiv 0 \qquad \text{for } x > x_f \qquad (3.37)$$

$$Y_2 \equiv 0 \qquad \text{for } x < x_f \qquad (3.38)$$

$$2\epsilon x \frac{dY_2}{dx} + \mathscr{D}_{23} \frac{d^2 Y_2}{dx^2} = 0 \qquad \text{for } x > x_f \qquad (3.39)$$

where $\alpha = k/\rho c_p$ is the thermal diffusivity, together with the boundary conditions (3.19)-(3.20) where ρ is assumed constant. At $x = x_f$,

$$[T] = [Y_1] = [Y_2] = 0 \qquad (3.40)$$

$$\frac{\alpha}{Q/c_p}\left[\frac{dT}{dx}\right] = -\frac{\mathscr{D}_{13}}{W_1}\left[\frac{dY_1}{dx}\right] = -\frac{\mathscr{D}_{23}}{2\,W_2}\left[\frac{dY_2}{dx}\right]. \qquad (3.41)$$

The solution of this problem is readily obtained as

$$
T = \begin{cases} T_\infty + (T_f - T_\infty)\dfrac{1 + \mathrm{erf}\left(\sqrt{\epsilon/\alpha}\,x\right)}{1 + \mathrm{erf}\left(\sqrt{\epsilon/\alpha}\,x_f\right)} & x < x_f \\[3mm] T_\infty + (T_f - T_\infty)\dfrac{1 - \mathrm{erf}\left(\sqrt{\epsilon/\alpha}\,x\right)}{1 - \mathrm{erf}\left(\sqrt{\epsilon/\alpha}\,x_f\right)} & x > x_f \end{cases}
$$

$$
Y_1 = \begin{cases} 1 - \dfrac{1 + \mathrm{erf}\left(\sqrt{\epsilon/\mathscr{D}_{13}}\,x\right)}{1 + \mathrm{erf}\left(\sqrt{\epsilon/\mathscr{D}_{13}}\,x_f\right)} & x < x_f \\[3mm] 0 & x > x_f \end{cases}
$$

$$
Y_2 = \begin{cases} 0 & x < x_f \\[3mm] 1 - \dfrac{1 - \mathrm{erf}\left(\sqrt{\epsilon/\mathscr{D}_{23}}\,x\right)}{1 - \mathrm{erf}\left(\sqrt{\epsilon/\mathscr{D}_{23}}\,x_f\right)} & x > x_f \end{cases}
$$

with the position x_f of the flame sheet and the adiabatic flame temperature T_f, defined as the value of T at the flame sheet, satisfying

$$
\frac{1 + \mathrm{erf}(\sqrt{\epsilon/\mathscr{D}_{13}}\,x_f)}{1 - \mathrm{erf}(\sqrt{\epsilon/\mathscr{D}_{23}}\,x_f)} = \nu \sqrt{\frac{\mathscr{D}_{13}}{\mathscr{D}_{23}}}\,\frac{e^{\epsilon x_f^2/\mathscr{D}_{23}}}{e^{\epsilon x_f^2/\mathscr{D}_{13}}} \tag{3.42}
$$

$$
T_f = T_\infty + \frac{1}{2}\frac{Q/c_p}{W_1}\sqrt{\frac{\mathscr{D}_{13}}{\alpha}}\,\frac{1 - \mathrm{erf}^2(\sqrt{\epsilon/\alpha}\,x_f)}{1 + \mathrm{erf}(\sqrt{\epsilon/\mathscr{D}_{13}}\,x_f)}\,\frac{e^{\epsilon x_f^2/\alpha}}{e^{\epsilon x_f^2/\mathscr{D}_{13}}} \tag{3.43}
$$

where $\nu = 2W_2/W_1$ is a mass-weighted stoichiometric ratio. The position x_f is determined from the transcendental equation (3.42) using an iterative process. We note that for a given strain rate ϵ the position x_f depends only on the binary diffusivities Ti-TiB$_2$ and B-TiB$_2$ and independent of the diffusivity of Ti-B, since there is no boron in the titanium region and vice-versa. Once x_f is determined, the flame temperature can be calculated from (3.43) by direct evaluation. Evidently, the latter depends on the heat released Q and thermal diffusivity α.

For equal diffusivities $\mathscr{D}_{13} = \mathscr{D}_{23} \equiv \mathscr{D}$, eq. (3.42) reduces to

$$\mathrm{erf}\left(\sqrt{\epsilon/\mathscr{D}}\,x_f\right) = \frac{\nu - 1}{\nu + 1}\,.$$

For the titanium-boron reaction the mass-weighted stoichiometric ratio $\nu \approx 0.45$, implying that $x_f \approx -0.41\sqrt{\mathscr{D}/\epsilon}$ and the flame sheet lies on the titanium side of the stagnation plane. If the Lewis number is assumed equal to one, i.e., $\mathscr{D} = \alpha$, the flame temperature is given by

$$T_f = T_\infty + \frac{Q/c_p W_1}{1 + \nu}\,.$$

In the absence of differential (unity Lewis number) and preferential (unequal mass diffusivities) diffusion the flame temperature results from a simple energy balance.

3.4   Results from the Asymptotic Calculations
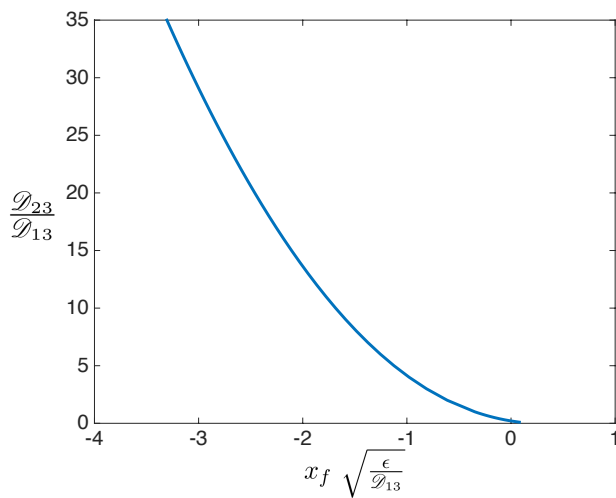
Figure 3.2: Variation of the position of the flame sheet with variations of the thermal diffusivities.

Table 1 lists representative values of physical parameters based on a literature survey. Some values required by the model are easier to estimate than others and are obtained fromt standard thermal properties measurements. Table 1 lists values for the constant pressure heat capacity, c_p,

(a)

(b)
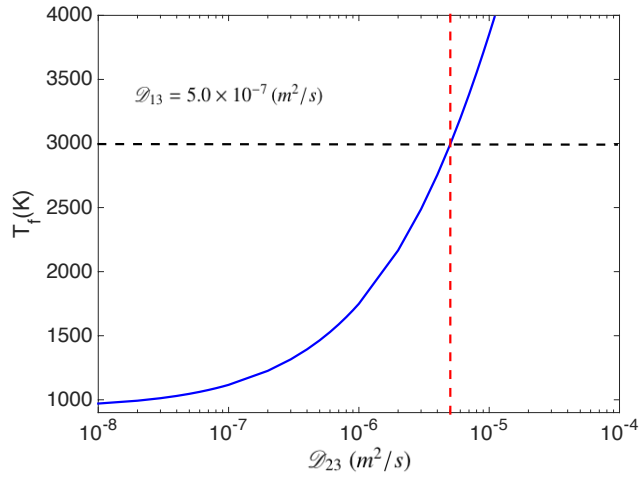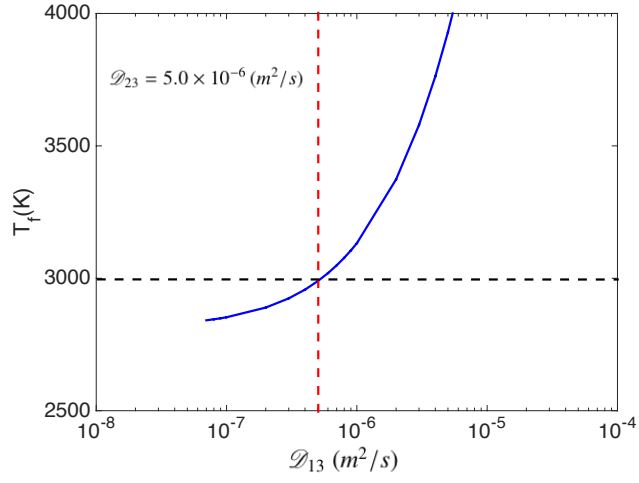
Figure 3.3: Variation of the adiabatic flame temperature (a) with $\mathscr{D}_{13}$ for given $\mathscr{D}_{23}$, and (b) with $\mathscr{D}_{23}$ for given $\mathscr{D}_{13}$.

and thermal conductivity, k, that represent averaged values for the mixture. However determination of values for the binary mass diffusivities, is more problematic. Experimental values for $\mathscr{D}_{13}$ and $\mathscr{D}_{23}$ have been obtained [44] [45], but not at conditions that are present in the reaction zone structure. Figure 3.2 is drawn by using formulas (3.42)-(3.43), for a fixed ν and displays how the scaled flame

sheet location varies with the ratio $\mathscr{D}_{23}/\mathscr{D}_{13}$. This ratio is typically larger than one, since boron atoms have an effectively smaller atomic radius and hence diffuse more readily through titanium-diboride than does the titanium atom, [44] [45]. We find that the flame sheet location will generally reside on the titanium side of the stagnation plane and move further to the left when the diffusivity of boron the product titanium-diboride increases, relative to that of titanium.

The values for the mass diffusivities are not well-known or measured, especially for the condition near the reaction zone. Thus we use known facts about the experimentally observed flame temperature. Trunov et al., [32] measured adiabatic flame temperature to be approximately between 2400-3300 K, when titanium and boron react. We expect that both mass diffusivities, $\mathscr{D}_{13}$ and $\mathscr{D}_{23}$ must be much less than the thermal diffusivities, and we expect that the boron diffusivity is significantly larger than the titanium diffusivity, in titanium diboride, i.e. we expect $\mathscr{D}_{23} >> \mathscr{D}_{13}$, similar to that that is found verified experimentally at lower temperatures [45]). Specifically we take $\mathscr{D}_{23}/\mathscr{D}_{13} = 10$ as a base-line model value, and a base-line estimate of the flame-sheet temperature to be 3000K. Then formulas (3.42)-(3.43) are used to estimate these coefficients based on our description being required to be consistent with the observed flame temperature. Then the base-line mass diffusivitiies are found to be $\mathscr{D}_{13} \approx 5 \times 10^{-7}\,\mathrm{m}^2/\mathrm{s}$ and $\mathscr{D}_{23} \approx 5 \times 10^{-6}\,\mathrm{m}^2/\mathrm{s}$. Figure 3.3(a) and (b) correspond to change in flame temperature with binary diffusivities $\mathscr{D}_{13}$ and $\mathscr{D}_{23}$ relative to the base-line values for the fixed ratio of $\mathscr{D}_{13}/\mathscr{D}_{23}$.

3.5   Numerical solution - finite-rate chemistry

To examine the effects of finite-rate chemistry, the boundary value problem consisting of (3.7)-(3.9) and (3.32)-(3.33) subject to the boundary conditions (3.18)-(3.20) is solved numerically. The numerical procedure is described in the Appendix and we present the results pertaining to titanium-boron combustion in the next section.

Property	Symbol	Value
Heat release	Q	-323.8 kJ/mol [46]
Molar mass of Ti	W_1	47.87 g/mol
Molar mass of B	W_2	10.81 g/mol
Molar mass of TiB$_2$	W_3	69.85 g/mol
Averaged molar mass	W_c	50 g/mol
Intrinsic density of Ti	$\hat{\rho}_{1_0}$	4.5 g/cc
Intrinsic density of B	$\hat{\rho}_{2_0}$	2.34 g/cc
Intrinsic density of TiB$_2$	$\hat{\rho}_{3_0}$	4.52 g/cc
Averaged density	$\hat{\rho}_{c_0}$	3.8 g/cc
Heat capacity	c_p	900 J/(kg K) [46]
Thermal conductivity	k	36 W/(m K) [47] [48] [49]
Pre exponential factor	B	7.6e16 mol/(m^3 s) [50]
Activation energy	E_a	318 kJ/mol [50]
Binary diffusivity of Ti-B	$\mathscr{D}_{12}$	0.2 m^2/s [51]

Table 3.1: Propperty values used for the for Ti-B problem

3.6 Numerical Results

3.6.1 Low strain rates

We start by presenting results pertaining to low strain rates, where the solution can be compared directly to the asymptotic solution discussed above. Since the latter was obtained under the constant density assumption, we selected an average value of $\rho = 3.8$ g/cc while abandoning thewidth=2.8in equation of state (3.17). However, the expressions for the diffusion coefficients were used *without* resorting to the approximation of equal molecular weights, since the reduced form of these relations led to nearly identical results.

Figures 3.4(a)-(b) show a comparison of the temperature and mass fraction profiles between the computed solution for $\epsilon = 0.01 \, \mathrm{s}^{-1}$ and the corresponding asymptotic expressions. The spatial coordinate has been normalized with the thermal diffusion length $l_d = \sqrt{\alpha/\epsilon} = 3.2410^{-4}$ cm. For such low values of strain rate combustion is nearly complete, with both reactants consumed in a very thin reaction zone. There is excellent agreement between the computed and asymptotic profiles except for very small changes near the reaction zone, as shown in the inserts. It should be noted that for finite ϵ, however small, the reaction zone has a finite thickness and Figure 3.4(c)

(a) Temperature profile

(b) Mass fractions profiles
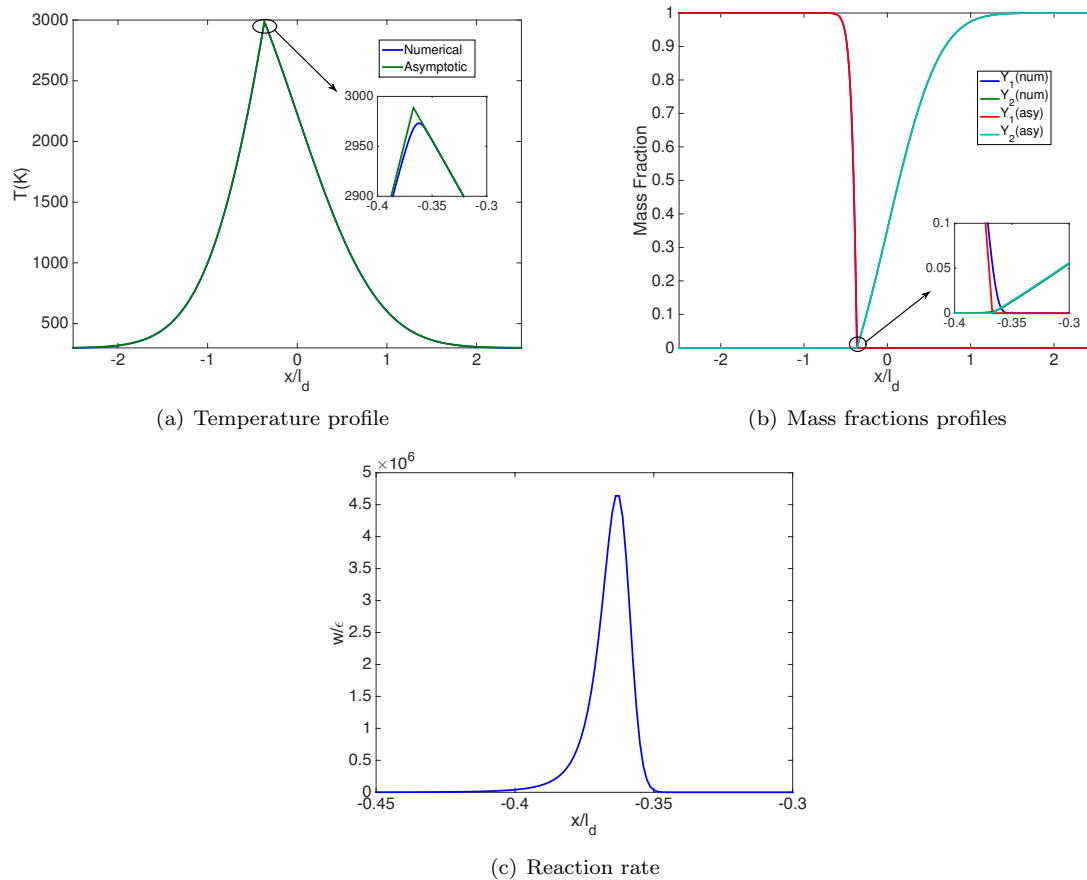
(c) Reaction rate

Figure 3.4: Comparison between the numerical solution and asymptotic solutions for a small strain rate $\epsilon = 0.01\ s^{-1}$

shows that our numerical grid is sufficiently dense to capture the reaction zone adequately. The excellent agreement between the numerical and asymptotic solutions also serves as a validation of our numerical methodology that properly accounts for the stiffness of the governing equations arising from the exponential Arrhenius term.

3.6.2   Moderate strain rates - constant density

Next we consider the entire response of the flame to increasing strain rates, from complete combustion corresponding to low strain rates to flame extinction occurring at significantly higher values

of ϵ. We first examine the difference in the solution obtained using the two diffusion formulations: The complete expressions for the diffusion coefficients a_i, b_i and the simplified form resulting from equal molecular weights. We note that the general diffusion expressions add increased nonlinearity to an already very stiff problem. To facilitate the computations we have therefore retained the constant-density approximation, which effectively decouples the flow and combustion fields; variable density solutions will be presented in the next subsection. Figure 3.5 shows a comparison of the flame position and flame temperature using the two diffusion formulations. The flame position x_f is defined as the location where the temperature reaches its maximum value, the flame temperature T_f. Figure 3.6 shows the mass fractions evaluated at the flame position x_f, which represent the amount of unconsumed reactants, as a function of the strain rate for the two formulations. We note that the precise evaluation of the flame position, and consequently the solutions evaluated at this location, depend on the step size used in the computations and on the value of the thermal diffusion length l_d, which decreases from $3.24 \cdot 10^{-5}$ cm to $1.3 \cdot 10^{-6}$ cm as the strain rate increases from $\epsilon = 0.01 \, \mathrm{s}^{-1}$ to $\epsilon = 6.5 \, \mathrm{s}^{-1}$ (which is very near extinction). Therefore, a Matlab Curve Fit [28] tool was used to fit the numerical data to a smoothing spline. The same tool was also used to fit a smoothing spline curve to the discrete numerical results presented in all figures.

From the response curves of Figures 3.5-3.6 the following physical picture emerges. At low strain rates the chemical reaction time is much smaller than the flow time and consequently, the reaction proceeds immediately as titanium and boron get in contact. The reaction occurs in a very thin zone (or a sheet), where the reactants are completely consumed. The flame temperature then reaches its maximum value. Upon increasing the strain rate, the flow time relative to the chemical reaction time is shortened and some titanium escapes to mix with boron leaking through the reaction zone, and vice-versa. As a result of incomplete combustion, the flame moves towards the boron side and the flame temperature drops. The relatively larger leakage of titanium as opposed to boron stems from the fact that $\mathscr{D}_{13} \ll \mathscr{D}_{23}$, which implies much larger fluxes of boron towards the reaction zone and consequently more complete combustion of boron. When the unconsumed mass fractions exceed a critical threshold, the flame temperature has been lowered significantly and steady burning is no longer possible. The critical state, represented by the turning point on the response curves,

51
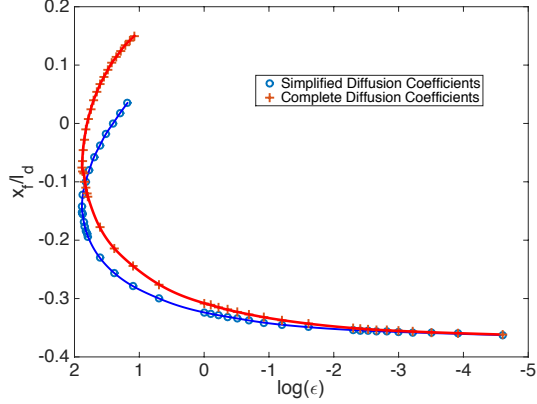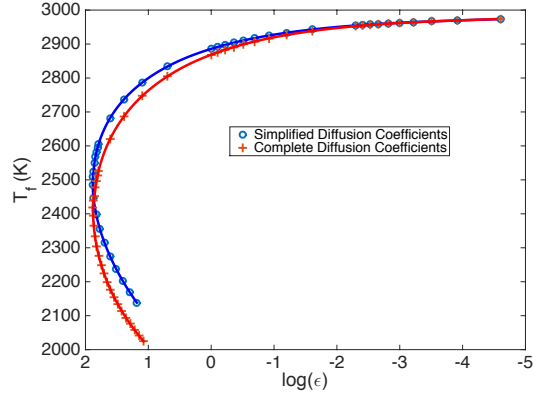
(a) Flame position

(b) Flame temperature

Figure 3.5: Response curves of (a) flame position and (b) flame temperature versus strain rate. The two curves (red/blue) correspond to the complete and simplified diffusion formulations.

identifies flame extinction. We believe the lower branch on the temperature response curve and the upper branches in Figure 3.6 to be unstable and therefore physically inaccessible.

The two diffusion formulations lead to identical results at low strain rates and predict the exact same extinction strain rates. There are small, insignificant differences in flame temperature at and near extinction, which can be traced to the slight difference in flame location. Being influenced primarily by the binary diffusivity $\mathscr{D}_{13} \ll \mathscr{D}_{23}$, the simplified diffusion formulation predicts a flame position that is slightly tilted towards the titanium ($x < 0$) side. Due to the negligible difference between the two formulations, the simplified diffusion formulation will be used in the following
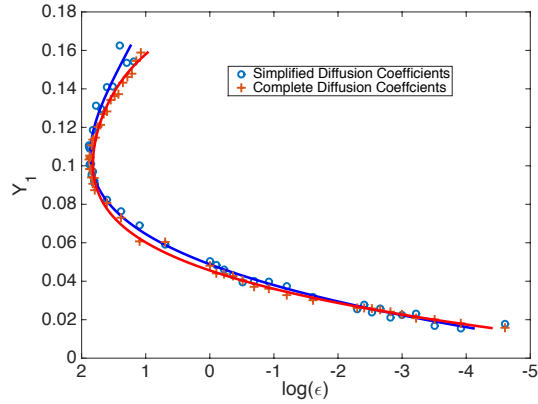
(a) Unconsumed titanium mass fraction
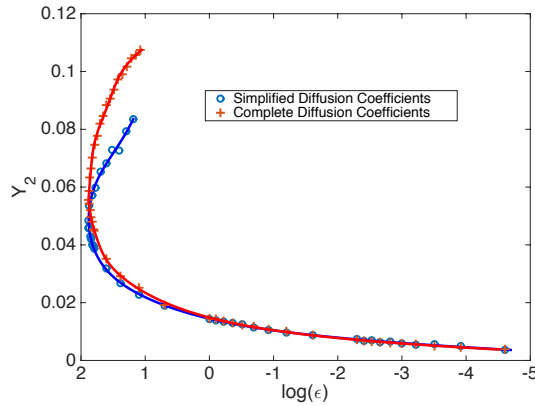
(b) Unconsumed boron mass fraction

Figure 3.6: The extent of unconsumed reactants leaking through the reaction zone. The two curves (red/bliue) correspond to the complete and simplified diffusion formulations.

section in order to save computational time.

3.6.3 Moderate strain rates - variable density

When variations in density are accounted for, the flow field no longer satisfies (3.22) and must be obtained by solving eq. (C.1) with ρ given by (3.17). The boundary condition (3.18) implies that $\bar{\vartheta}$ is approximately constant, as $|x| \to \infty$, with the asymptotes subject to the constraint (3.12). Figure 3.7 shows profiles of $\bar{\vartheta}$ computed for two values of ϵ, the low strain rate corresponding to conditions close to the Burke-Schumann solution and the larger strain rate corresponding to near-
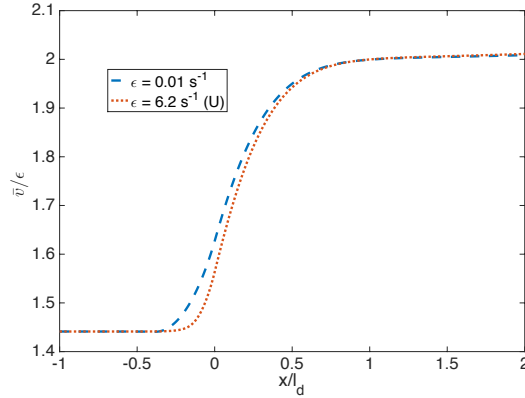
Figure 3.7: Profiles of the transverse velocity $\bar{\vartheta}$ across the combustion zone for two values of strain rates.

extinction conditions. In both cases the solution behaves as expected: at low x, the solution does not change but at large x there is a slight variation due to density variation.
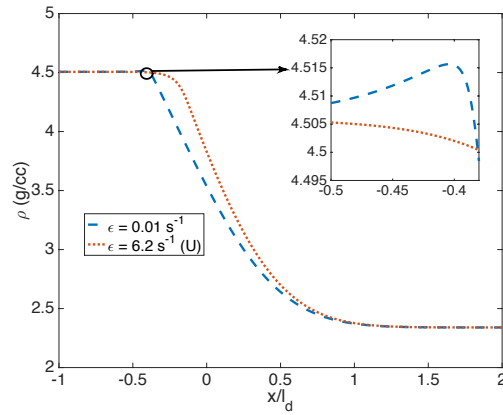
Figure 3.8: Density profiles across the combustion zone for two values of strain rates

Density profiles are shown in Figure 3.8 for the same two values of ϵ. Due to the density of TiB_2 being only slightly higher than Ti, we have a noticeable jump in density only at lower strain rates. At lower strain rates, the reaction rate is higher, thus the production of TiB_2 is also higher. At higher strain rates, because of increased diffusion, the density curve gradually decays from titanium to boron due to decrease in production of TiB_2.

Response curves of flame position and temperature vs strain rates, for constant and variable

density conditions, are shown in Figure 3.9. The flame temperature $T_f = 3000\,\mathrm{K}$ at the Burke-Schumann limit for the constant density case is slightly higher than for the variable density case, where $T_f = 2950\,\mathrm{K}$. This difference is due to the selected mean density adopted in the constant density formulation. Elsewhere the two solutions are very close indicating that the composition effect on density is of little significance, for practically all strain rate values. The flame temperature at extinction, for both constant and variable density formulation, is approximately $2500\,\mathrm{K}$, corresponding to a drop in approximately $500\,\mathrm{K}$ from the adiabatic fame temperature.
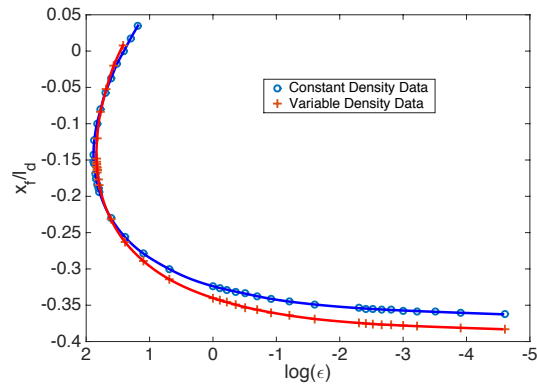
(a) flame psotition
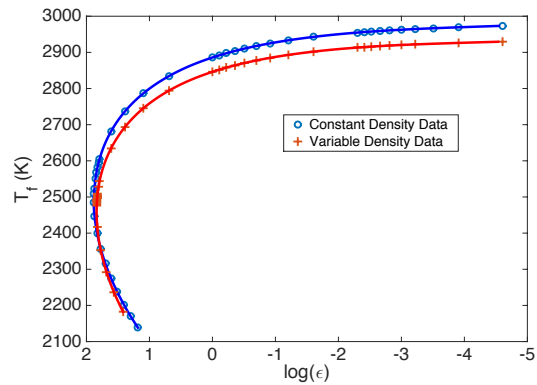
(b) flame temperature

Figure 3.9: Comparison of flame position and temperature between constant and variable density conditions.

The flame position between the two flame formulations is compared in Figure 9(a). As in the constant density case, the flame position is an arbitrary concept because the reaction zone is of
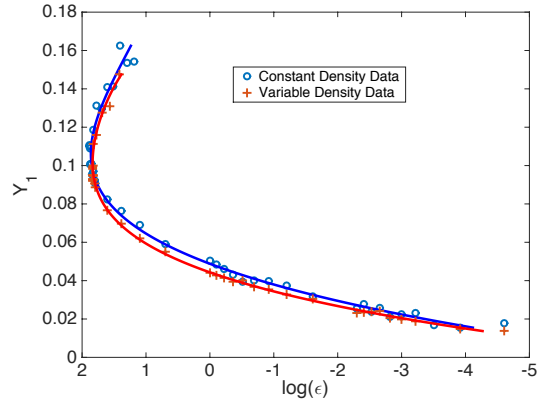
(a) Unconsumed titanium mass fraction
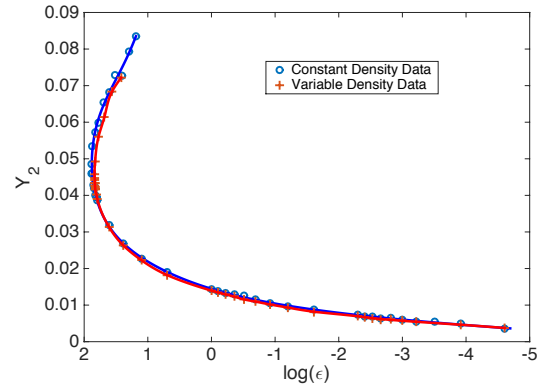
(b) Unconsumed boron mass fraction

Figure 3.10: Y_1 response curve comparison between constant and variable density approximations

finite length in the numerical simulation. To maintain consistency, x_f is chosen at the location of flame temperature. The variable density solution has a lower x_f than the constant density solution. This is once again due to the chosen parameters and the density variation in the species equation. As seen through the asymptotic analysis, the temperature equation has little effect on the flame position at the complete combustion limit. Therefore, the reason for the slight variation between the two flame position graphs at this limit could be directly attributed to the dependence of species equation on density. As with the flame temperature case, x_f at extinction between the two formulations are almost exactly the same, with the difference between them being less than 0.1%.

As mentioned before, one parameter of leakage through the reaction zone is the value of Y_1 and Y_2 at x_f. In Figure 3.10, we compare the leakage of titanium and boron between the two formulations. In both scenarios, there is a strong match at low strain rates. But as the strain rate increases, the variable density solutions for both Y_1 and Y_2 show a slight deviation from the constant density solutions. This is more evident in the case of Y_1 because the diffusion region for titanium is much smaller than that of boron, thus causing a sharper response to the density dependence. The difference between the two solutions at extinction is about 0.005 for Y_2 and 0.05 for Y_1. The differences are approximately 10% of the actual extinction value.

3.7   Conclusion

In this chapter, we use a multi-component mixture theory to describe condensed phase diffusive combustion, in particular for a counterflow geometry. The traditional Fick diffusion model is informed by binary diffusion constants that are defined by the Maxwell-Stefan model of diffusion. Low temperature measurement of binary diffusion coefficients $\mathscr{D}_{23}$ range from 10^{-13} to 10^{-20} m^2/s [52], [44] while $\mathscr{D}_{13}$ is predicted to be three orders of magnitude lower than that of $\mathscr{D}_{23}$, [45]. But the temperature dependence of these coefficients is not known at high temperatures. Trunov et al. [32] predicts the combustion temperature of Ti-B nano-composite around 3000K, for states where diffusion coefficients are unavailable. With asymptotic analysis we have made an estimate of these diffusion coefficients that are consistent with respect to Trunov et al. [32] macroscopically observed adiabatic flame temperatures.

The proposed diffusion expressions are cumbersome to handle numerically. Therefore a reduced diffusion expressions were proposed by assuming equal molecular weights. The comparison between the two diffusion models, is carried using the constant density formulation. The numerical solution is validated by comparing it to the analytical limit of complete combustion at the lowest chosen strain rate. The analytical solution does not vary between two diffusion expression since both of them go to the same value at this limit. The response curve of flame temperature, position

and leakage of titanium and boron with respect to strain rate is computed using both diffusion expressions. Explicit numerical methods are difficult to implement for this model due to large stiffness in the governing equations. Therefore an implicit method is used and combined with continuation algorithm to compute the extinction point and the unstable solutions. We find that both diffusion expressions yield almost the same extinction strain rate of $6.5\,s^{-1}$. The response curves between the two diffusion expressions are identical to each other at large strain rates and vary to about less than 2% near extinction. Thus, we found we could safely use the constant molecular weight approximations in the diffusion terms with minimal loss in accuracy, while saving computational time and complexity.

We then proceed to compute the full flow problem with varying density. The mixture equation of state is simply assumed to be weighted summation of the species reference density. The two dimensional counterflow is simplified by using a similarity solution for the x and y component of velocity. The numerical procedure for density variation formulation is different than constant density due to integration of continuity equation to compute x-velocity, which increases the computational time to achieve convergence. Once again, the response curves mentioned above were computed for the variable density solution and compared with the constant density. Because of the chosen values for parameters, the complete combustion limit for the two solutions are different by about 50K with the constant density plot being greater than that of variable density. The difference in extinction strain rate is about $0.2\ s^{-1}$ which is less than 0.5 % of the strain rate value of 6.5 s^{-1}. The extinction flame temperature between the two formulation is almost exactly the same at 2500 K. There is similar behavior in the analysis of the flame position. When comparing the leakage of Y_1 and Y_2 between the two formulation, we notice that they are very close to each other with little difference at both the complete combustion limit and extinction. Although the two formulations are close to each other, different set of parameters can lead to a larger more significant difference. It is important to note that the adiabatic flame temperature used in this chapter differs from the values presented by Fisher and Grubelich [53], which is approximately 3500K. This means that the binary diffusivities used in the model might be larger than predicted but it does not change the methods used in this calculation.

Chapter 4

Theoretical and Experimental Investigations of Fast Ignition/Quenching in Al/CuO Thermite

4.1 Introduction

An alternative to the well-structured layered composites are agglomerated materials made of a mixture of reactive and inert components. Glumac et al. [7] have recently reported results of shock compaction experiments on porous materials that are initially composed of two reactive components. Systems that have been studied include the aluminum (Al), copper oxide (CuO) thermite, and the metal/intermetallic system composed of titanium, silicon, and titanium, boron. A typical shock compaction experiment is carried out for 80% porous, stoichiometric mixture of components, with the initial mass fractions based on the overall equilibrium products. For the Al-CuO system the stoichiometric reaction is

$$2\text{Al} + 3\text{CuO} \rightarrow \text{Al}_2\text{O}_3 + 3\text{Cu} \tag{4.1}$$

The reactive material sample is placed in a striker assembly, and compacted by the action of two metal bars that are shock loaded by the firing of detonators on each end. A sustained heterogeneous front was found to propagate at an average speed of approximately 6-20 cm/sec. High speed microscopic photography was used to record the emitted light seen through a small observation window. On a length scale of 10 to 200 μm, one observes the sudden formation and disappearance of intense spots of light, corresponding to intense and weak chemical reactions recurring within

59

a time interval of approximately 100 μs. These experiments clearly demonstrate that the overall combustion process is highly unsteady. While the lead reactive front after shock compaction is observed to propagate at a well-defined average velocity, measurable and robust, time-dependent heterogeneous reaction-diffusion processes occur on the micro-scale, corresponding to the initial size of the reactive component particles, before and after the passage of the lead shock. Since the component materials and their reactants are very hot and experience significant thermal expansion, the chemically reacting material experiences a distribution of local flow velocities and strain rates, primarily at the material interface of the reacting components.

The theoretical modeling approach for the finely-space laminate, or regular structured materials, can be summarily described as an approach that lumps, or relies on cross-sectional averages for all transport phenomena, such as bulk heat transfer and diffusion, and for all material properties of the laminate/arrays [34]. These reduced models seem to appropriately describe observed phenomena that depend on average properties of the system, such as bulk temperature and reaction extent, or the self-propagation speed of a reactive front propagating along the axis of the plane of the plies. They do not explicitly describe the reaction-diffusion phenomena at material interfaces, and cannot delineate separate molecularly distinct reactants. The focus in this work is exactly on the processes taking place on a small-scale of the the initially-separated component materials that comprise the mixtures, that are not necessarily layered or structured. Our approach delineates separate molecularly distinct reactants and employs a multicomponent, thermodynamic formulation with separated reactants and products, each with their own properties. While we employ some simplifications, we do not use a lumped, averaged formulation in the same sense of the reduced models found in the analysis of finely-spaced laminates or arrays. Fundamental understanding of these local events will serve as a basis for future modeling of time-dependent reaction processes in both classes of energetic materials, agglomerated composites and finely-spaced, structured or layered composites.

The phase change in the system consists of melting and refreezing of Al, CuO, Cu and Al_2O_3 (which will be called AlOx for the rest of the chapter). It is important to note that we have neglected the reaction between CuO and Al_2O_3, which produces $CuAl_2O_4$. In the model presented

here, the different phases of a material are treated as separate species. Therefore, the phase change is treated similar to reaction. We propose a set of 10 reactions as seen in Equation (4.11), in which the two exothermic reactions only progress forward. All four materials can melt or freeze depending on the local temperature which results in a total of 8 species. The material diffusion between the constituent materials is described using a Maxwell-Stefan diffusion model, which is formulated in terms of binary diffusivities. In order to simplify the analysis, we assumed that solid-solid diffusion is negligible while all solid-liquid and liquid-liquid diffusion are equal. Each isolated component is assumed to have its own distinct reference density, and we neglect thermal expansion in the components. This is consistent with the notion that the change in composition due to reaction is much larger than changes due to thermal expansion. As a result the mechanical equation of state for the mixture takes a simple form whereby the specific volume of the mixture is simply a sum of the intrinsic densities weighted with the mass fraction of each component. This form of the mechanical equation of state stands in contrast with that for a mixture of reacting gases that is a relation between the specific volume, pressure, temperature and mass fractions.

We propose a slab geometry with a mixing region of 100 μm between the initial reactants. By creating a thermal impulse at one end of the domain, this results in melting of Al and CuO which in turn causes the reaction. Two different thermal impulses (3000K and 2000K) were studies to analyze the effect of local temperature on the reaction. In the case of 2000K, once sufficient time passes post ignition, the product AlOx re-freezes, which does not occur in the 3000K case.

4.2   Experimental setup

The experiments were preformed by Glumac's group at the University of Illinois [7]. The material tested was a stoichiometric thermite mixture of aluminum and copper oxide. The copper oxide has a -325 mesh designation and the aluminum is nominally 3 μm flake. The components of the thermite are blended by hand and then ultrasonically mixed under hexane for 20 minutes. Once consistent mixing is achieved, the hexane is removed through a vacuum drying process. Upon preparation, the reactive material was subjected to cold pressing in a 50 ton press to achieve an 80% theoretical
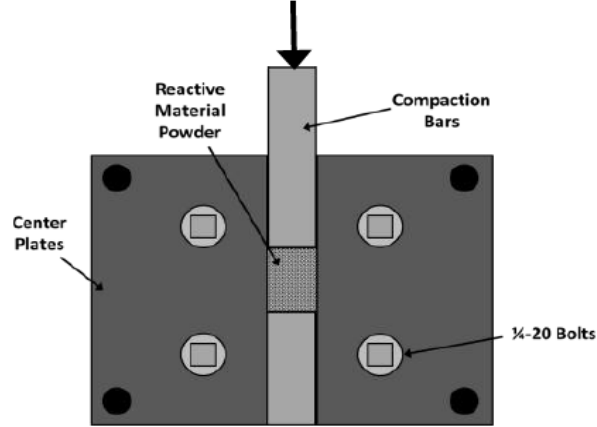
Figure 4.1: Schematic of sample die with front plate removed

mass density (TMD). The sample die consists of a back plate, two center plates, and a front plate, all of which are created using 4142 alloy steel. The center plates, once attached to the back plate, leave a channel where the material powder is compacted by two square steel bars, each 3/8 inches to a side. This arrangement creates a cube of reactive material with a constant volume of 0.8641 cm^3. A diagram of this die is shown in Figure 4.1. The loose powder was loaded into the sample die and compacted. Once the reactive material cube is pressed, the front plate of the sample die is replaced with the viewing window plate and the compaction bars are replaced with longer collision driver rods for the experimental setup. The experimental setup, as shown in Figure 4.2 consists of the sample holder and shock drivers, a telephoto lens, the high speed camera, and a flash lamp. The sample holder doubles as the sample die, but with a modified front plate that contains a viewing window for high speed imaging. There are two 3/8-inch square 4142 steel bars that are 1.5 inches in length, housed in the channel between the center plates. On one end the rods contact the reactive material cube, and on the other end the detonators are mounted flush against the rod ends. The detonators are housed in a cylinder of low-density polyethylene (LDPE), which absorbs much of the detonator fragmentation after initiation. The entire sample holder is mounted in a 4142 steel base, which is then fixed to an optical table for rigidity. The shock initiation of the reactive material sample is imaged using a Nikon AD-EF 80-200 mm telephoto lens. The telephoto lens is reversed

62
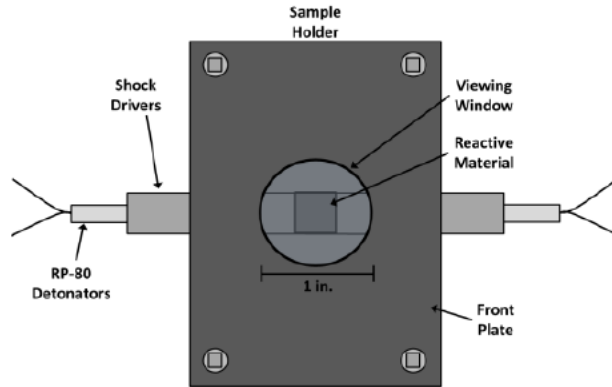
Figure 4.2: Schematic of experimental setup [7]

and detached from the imaging camera in order to produce a higher magnification when viewing the reactive material at short distances. In this magnified viewing arrangement the zoom of the lens can be selected in order to produce viewing windows that are on the order of 4 mm wide. The detector used for this study is a Phantom 5 high speed imaging camera from Vision Research. The images analyzed for quantitative data were taken with a 42 μs interval and 2μs exposure. This rate was achieved using a reduced portion of the chip (256 x 104 pixels). An image sequence is shown in Figure 4.3 below. This is a series of images from a stoichiometric Al-CuO thermite test with an entire face of the RM cube in the FOV. In this sequence, the first image shows the unreacted sample cube (outlined in red) while the second image shows the 'crush up' of the 80% TMD reactive material just after the detonators are initiated at time t = 0 ms. The remaining images show the reaction that takes place after shock loading has occurred. According to the timing of the images, there is a rather long delay between the material crush up and the initiation of the reaction at 23 ms. This shows that the reaction is indeed shock assisted, rather than shock induced, for the aluminum-copper oxide thermite. In Figure 4.4, the high speed image sequences demonstrated localized bright spots that flicker which is correlated to an ignition and quenching processes. To analyze the emissive behavior of hot spots in these images, an algorithm(which was developed by Christopher Murzyn of Prof. Glumac's group at University of Illinois) was written to select a very small region around any spot in the image, and integrate the 16 bit pixel intensity vales within the

63
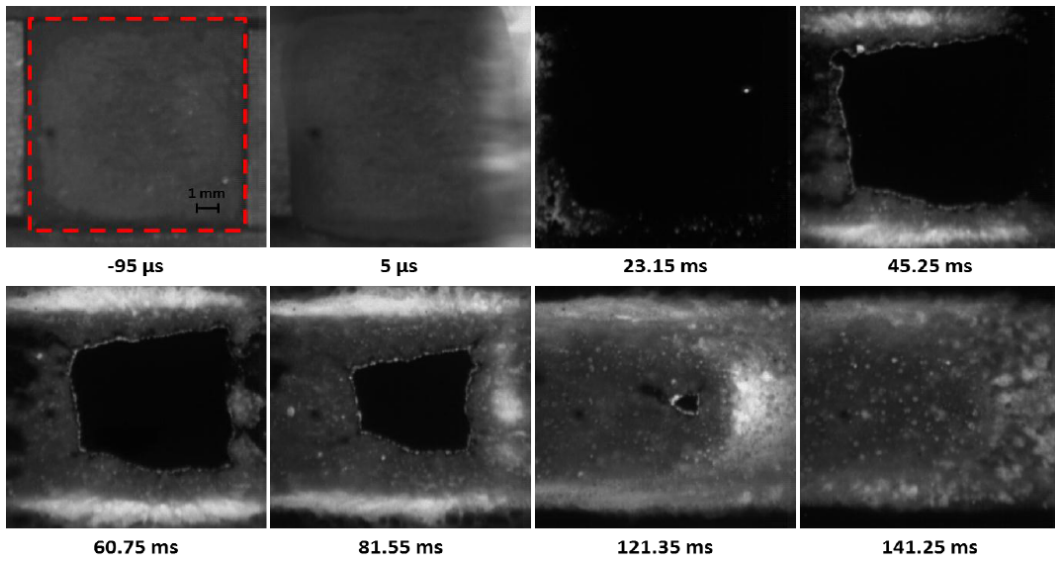
Figure 4.3: Image sequence of Al/CuO thermite reaction progress [7]
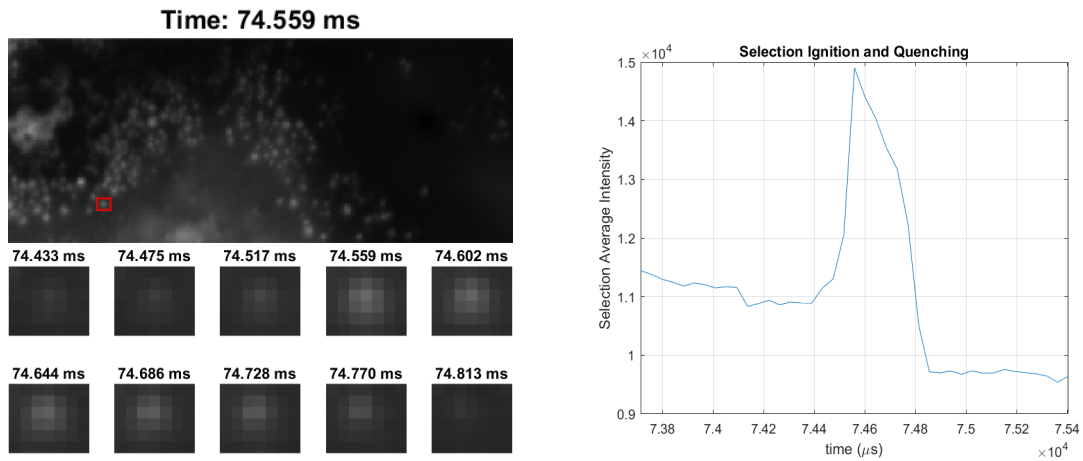
Figure 4.4: Targeted image sequence of a localized ignition/quenching event (left), averaged intensity analysis in select region (right) [7].

cropped region of each picture. From these values we can see the relative change in spot emission corresponding to each frame in the high speed video.

4.3 Formulation

We used the recently developed [54], Gibbs formulation, to model an ignition event that is motivated by the experiment, where ignition of reaction occurs via rapid heating of thin one dimensional laminate of initially separated solid Al and CuO reactants. This numerical framework is developed in collaboration with Kibaek Lee, another member of Prof. Stewart's group. The Gibbs formulation assumed that there is a single, well-defined stress tensor, and temperature at any point in the material that is defined by the assumption of local equilibrium (EQB). Chemical changes and phase changes are not assumed to be in EQB, and the formulation thus is based on non-EQB thermodynamics, well-grounded in the principles of classical Physical Chemistry. All components including different phases of the same molecular material must have a complete EQB potential. Unlike classical phase field theory, that uses an order parameter or differences in molecular density to switch the constitutive description of the phases, the mass fraction is the order parameter(s), and equilibrium EOS descriptions for the multi-component materials are derived in a straightforward way.

Consideration of the basic processes of a thermite, that generates two products by oxygen exchange, from two reactants with consideration of the importance of phase change (melting from solid to liquid), leads to model that minimally has eight components. For our example and the experiment these would be Al-solid and liquid, CuO-solid and liquid, Cu-solid and liquid and Al_2O_3-solid and liquid. In the limit of sufficiently slow phase and chemical changes, the thermal and reaction extent is uncoupled from the stress/displacement field. And when inertial effects are insignificant, one can ignore the advection contribution to the material rate of change. Once the thermal field is solved for, the stress displacement field can be solved for, if needed. In the simplest case, the model leads to energy equation for temperature (T) that is coupled to mass fraction (Y_i) equations, i.e.

$$\rho c_p \frac{\partial T}{\partial t} = -\sum_i \omega_i h_0^{(i)} + \frac{\partial}{\partial x}\left(K \frac{\partial T}{\partial x}\right) \tag{4.2}$$

$$\rho \frac{\partial Y_i}{\partial t} = \omega_i - \nabla \cdot (\rho Y_i V_i) \tag{4.3}$$

where ρ, c_p and K are the density, constant pressure heat capacity and thermal conductivity of the mixture. $h_0^{(i)}$, ω_i, and V_i represent the enthalpy of formation, reaction rate, and diffusion velocity of species i respectively. The mass fraction and diffusion velocities are subject to the constraint:

$$\sum_i^8 Y_i = 1 \tag{4.4}$$

$$\sum_i^8 Y_i V_i = 0 \tag{4.5}$$

The constant pressure heat capacity and thermal conductivity are modeled by mass-weighted summation of intrinsic values of individual components. Hence,

$$c_p = \sum_i^8 c_{p,i} Y_i \quad \text{and} \quad K = \frac{1}{\sum_i^8 Y_i \, \rho / (k_i \, \rho_i)} \tag{4.6}$$

where, $c_{p,i}$ and k_i are the constant pressure heat capacity and thermal conductivity of species i, which are assumed constant. In order to capture the density variation, we start with the assumption that the Gibbs free energy of each component of the mixture can be summed. The Gibbs potential for the mixture, which is a function of the pressure temperature and mixture composition, is

$$g = \sum_{i=1}^8 g_i(p, T) Y_i \,, \tag{4.7}$$

where the energies related to mixing has been neglected. The specific volume $v = 1/\rho$ of the mixture and individual components are given by the thermodynamic relation:

$$v = \left. \frac{\partial g}{\partial p} \right|_{T, Y_i} \quad \text{and} \quad v_i = \left. \frac{\partial g_i}{\partial p} \right|_T, \tag{4.8}$$

where v_i are the partial volumes or volume of the components. This leads to

$$v = \sum_{i=1}^{8} v_i(p, T) Y_i. \tag{4.9}$$

which is the mechanical equation of state for the mixture. If we further assume that the volume change under variation of pressure is small and we neglect the effect on temperature as well, then the component volumes v_i can be approximated by their reference values $\hat{v}_{i0}$. Hence, the density variation can be described as:

$$\rho^{-1} = \sum_{i=1}^{8} Y_i \, \hat{\rho}_{i_0}^{-1} \tag{4.10}$$

where $\hat{\rho}_{i_0}$ is the intrinsic density and $\hat{\rho}_{i_0}^{-1}$ is the intrinsic specific volume, of the species i.

4.3.1 Reaction

In what follows $Y_{1,2}$ refers to solid/liquid aluminum, $Y_{3,4}$ solid/liquid copper oxide, $Y_{5,6}$ solid/liquid copper, and $Y_{7,8}$ solid/liquid aluminum oxide, respectively. For the kinetic scheme, we assume all materials can melt and freeze and only the reaction between liquid aluminum and cooper oxide creates solid or liquid aluminum oxide. Thus

$$
\begin{aligned}
Al_{(s)} &\rightleftharpoons Al_{(l)} \\
CuO_{(s)} &\rightleftharpoons CuO_{(l)} \\
Cu_{(s)} &\rightleftharpoons Cu_{(l)} \\
AlOx_{(s)} &\rightleftharpoons AlOx_{(l)} \\
2Al_{(l)} + 3CuO_{(l)} &\rightarrow 3Cu_{(l)} + AlOx_{(s)} \\
2Al_{(l)} + 3CuO_{(l)} &\rightarrow 3Cu_{(l)} + AlOx_{(l)}
\end{aligned}
\tag{4.11}
$$
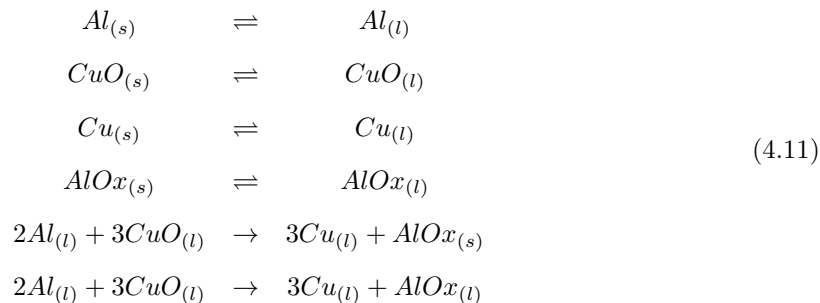
The freezing rate (i.e. the production of solid) of the components is assumed to be simply proportional to the mass fraction of its liquid if the temperature is below its melting point, and proportional to the negative of the mass fraction of the solid if the temperature is above its melting point. The melting rate of the component is the negative of its freezing rate. The rate of depletion of liquid

aluminum and liquid copper oxide have contributions from the reactions that produce liquid copper, and solid/liquid aluminum oxide. Similarly for the rate of production of liquid copper and solid/liquid aluminum oxide. Hence, the global rates for the eight components, according to the assumed reaction set are:

$$\omega_1 = W_{Al}\left[-\omega^{(1)} + \omega^{(2)}\right] , \tag{4.12}$$

$$\omega_2 = W_{Al}\left[\omega^{(1)} - \omega^{(2)} - 2\omega^{(9)} - 2\omega^{(10)}\right] , \tag{4.13}$$

$$\omega_3 = W_{CuO}\left[-\omega^{(3)} + \omega^{(4)}\right] , \tag{4.14}$$

$$\omega_4 = W_{CuO}\left[\omega^{(3)} - \omega^{(4)} - 3\omega^{(9)} - 3\omega^{(10)}\right] , \tag{4.15}$$

$$\omega_5 = W_{Cu}\left[-\omega^{(5)} + \omega^{(6)}\right] , \tag{4.16}$$

$$\omega_6 = W_{Cu}\left[\omega^{(5)} - \omega^{(6)} + 3\omega^{(9)} + 3\omega^{(10)}\right] \tag{4.17}$$

$$\omega_7 = W_{AlOx}\left[-\omega^{(7)} + \omega^{(8)} + \omega^{(9)}\right] , \tag{4.18}$$

$$\omega_8 = W_{AlOx}\left[\omega^{(7)} - \omega^{(8)} + \omega^{(10)}\right] \tag{4.19}$$

where, W_i is the molecular weight of species i. The individual reaction rates for the reactions are modeled by a dependence on concentration and a reaction coefficient k_i. In the model, we assume that the reaction coefficients are constant and independent of temperature. We further assume that the melting and freezing reaction rates are equal to each other, k_{rate}. The reaction that produces $AlOx_{(s)}$ and $AlOx_{(l)}$ are governed by the reaction rate coefficients, $k_{react}^{(AlOx_{(s)})}$ and $k_{react}^{(AlOx_{(l)})}$ respectively.

$$\omega_1 = k_{rate}^{(Al)}W_{Al}\begin{cases} Y_2 & \text{if } T < T_m^{(Al)} \\ -Y_1 & \text{if } T \geq T_m^{(Al)} \end{cases} \tag{4.20}$$

$$\omega_2 = k_{rate}^{(Al)}W_{Al}\begin{cases} -Y_2 & \text{if } T < T_m^{(Al)} \\ Y_1 & \text{if } T \geq T_m^{(Al)} \end{cases} - 2k_{react}^{(AlOx_{(s)})}W_{Al}Y_2Y_4 - 2k_{react}^{(AlOx_{(l)})}W_2Y_2Y_4 \tag{4.21}$$

68

$$\omega_3 = k_{rate}^{(CuO)} W_{CuO} \begin{cases} Y_4 & \text{if } T < T_m^{(CuO)} \\ -Y_3 & \text{if } T \geq T_m^{(CuO)} \end{cases} \tag{4.22}$$

$$\omega_4 = k_{rate}^{(CuO)} W_{CuO} \begin{cases} -Y_4 & \text{if } T < T_m^{(CuO)} \\ Y_3 & \text{if } T \geq T_m^{(CuO)} \end{cases} - 3k_{react}^{(AlOx_{(s)})} W_{CuO} Y_2 Y_4 - 3k_{react}^{(AlOx_{(l)})} W_{CuO} Y_2 Y_4 \tag{4.23}$$

$$\omega_5 = k_{rate}^{(Cu)} W_{Cu} \begin{cases} Y_6 & \text{if } T < T_m^{(Cu)} \\ -Y_5 & \text{if } T \geq T_m^{(Cu)} \end{cases} \tag{4.24}$$

$$\omega_6 = k_{rate}^{(Cu)} W_{Cu} \begin{cases} -Y_6 & \text{if } T < T_m^{(Cu)} \\ Y_5 & \text{if } T \geq T_m^{(Cu)} \end{cases} + 3k_{react}^{(AlOx_{(s)})} W_{Cu} Y_2 Y_4 + 3k_{react}^{(AlOx_{(l)})} W_{Cu} Y_2 Y_4 \tag{4.25}$$

$$\omega_7 = k_{rate}^{(AlOx)} W_{AlOx} \begin{cases} Y_8 & \text{if } T < T_m^{(AlOx)} \\ -Y_7 & \text{if } T \geq T_m^{(AlOx)} \end{cases} + k_{react}^{(AlOx_{(s)})} W_{AlOx} Y_2 Y_4 \tag{4.26}$$

$$\omega_8 = k_{rate}^{(AlOx)} W_{AlOx} \begin{cases} -Y_8 & \text{if } T < T_m^{(AlOx)} \\ Y_7 & \text{if } T \geq T_m^{(AlOx)} \end{cases} + k_{react}^{(AlOx_{(l)})} W_{AlOx} Y_2 Y_4 \tag{4.27}$$

4.3.2 Diffusion

The most common expressions used for multi-component diffusion are the Maxwell-Stefan (MS) relations, [42]

$$\nabla X_i = \sum_j \frac{X_i X_j}{\mathscr{D}_{ij}} (V_j - V_i), \tag{4.28}$$

where X_i is the molar fraction and V_i is the diffusion velocity vector of species i, $\mathscr{D}_{ij} = \mathscr{D}_{ji}$ is the binary diffusivity of a pair of species (i, j), and the summation is taken over all species present. It is important to note that this model neglects self diffusion. Although this relation was derived for

69

a dilute ideal gas mixture, it has been often applied to condensed phase media [43].

The use of the MS relations is quite complicated because the diffusion velocities V_i are not expressed explicitly in terms of the concentration gradients. In order to simplify the analysis, we assume that there is no solid-solid diffusion and equal molecular weight. Furthermore, we assume that all solid-liquid diffusion are equal ($\mathscr{D}_{SL}$) and all liquid-liquid diffusion are equal ($\mathscr{D}_{LL}$). Therefore, we must root-solve Equation (4.28) with the constraint (4.5) to find:

$$V_i = a_i \nabla Y_1 + b_i \nabla Y_2 + c_i \nabla Y_3 + d_i \nabla Y_4 + e_i \nabla Y_5 + f_i \nabla Y_6 + g_i \nabla Y_7 \tag{4.29}$$

The coefficients a_i, b_i, c_i, d_i, e_i, f_i and g_i are provided in the Appendix.

4.4   Numerical procedure

4.4.1   Physical parameters

Before we proceed on to the numerical procedure, we must first find the appropriate parameters needed for the governing equations.

Species	ρ_0 [g/cc]	c_p [J/(kg K)]	k [W/(m K)]	h_0 [kJ/mol]
Al_s	2.7 [55]	24.2 [46]	236 [56]	0 [46]
Al_l	2.375 [57]	31.59 [46]	91 [56]	10.74 [58]
CuO_s	6.315 [55]	42.3 [46]	6 [59]	-162 [60]
CuO_l	5.7 [61]	50.76 [46]	3	-160 [58]
Cu_s	8.94 [55]	24.443 [46]	401 [56]	0 [46]
Cu_l	8.02 [57]	32.844 [46]	166 [56]	13.2 [58]
$AlOx_s$	3.97 [62]	79.038 [46]	30 [63]	-1675.7 [46]
$AlOx_l$	3.053 [64]	138.934 [58]	15	-1620.6 [58]

Table 4.1: Property values of representative physical parameters used in the computations

In Table 4.1, we list representative values found in literature for constituent species in both solid and liquid phases. The melting point of Al, CuO, Cu and AlOx are 933K, 1600K, 1350K and 2327K [46]. The enthalpy, density, and thermal conductivity of liquid phase of materials are taken at the melting point. There is no available thermal conductivity data of liquid CuO and liquid

AlOx. Therefore, a conservative estimate of 50% of solid thermal conductivity values is taken as an approximation for its liquid thermal conductivity.

The mass diffusion between these materials have not been studied enough to obtain individual binary-diffusion coefficients. Therefore, we have qualitatively categorized the interactions into three phase: solid-solid diffusion, solid-liquid diffusion and liquid-liquid diffusion. Solid-solid binary diffusivities typically range between $10^{-20} - 10^{-48}$ cm^2/s [65], which are small and therefore neglected from our model. Liquid-liquid binary diffusivities ($\mathscr{D}_{LL}$) are on the order of 10^{-5} cm^2/s [65] while solid-liquid binary diffusivities ($\mathscr{D}_{SL}$) are on the order of 10^{-9} cm^2/s [66].

4.4.2 Numerical implementation

The governing equations (4.2-4.3) are solved by a parallel finite-difference solver, which uses a fourth order central difference scheme for spatial discretization and fourth order Runge-Kutta methods for temporal discretization. Equation (4.20-4.27) as implemented would cause extreme stiffness around the melting point due to phase change. Therefore, a 'tanh' function is used in order to make the reaction rates continuous in temperatures through the melting point. For example, Equation (4.20) is rewritten as:

$$\omega_1 = W_2\, k_{rate}^{Al} \left(Y_2 \frac{1 - \tanh(\frac{T - T_m^{(Al)}}{\epsilon})}{2} - Y_1 \frac{1 + \tanh(\frac{T - T_m^{(Al)}}{\epsilon})}{2} \right) \tag{4.30}$$

where, the factor ϵ corresponds to the length of the region that the 'tanh' function takes to go from 1 to -1. For our analysis, we use $\epsilon = 10$, which is illustrated in Figure 4.5 for the case of aluminum ($T_m = 933$K).

4.5 Results

4.5.1 Domain and rate characterization

As it can be seen in Figure 4.3, there are many fast ignition/quenching events across the sample after the burning front passes through. To simplify the analysis to a 1-D system of equations, a
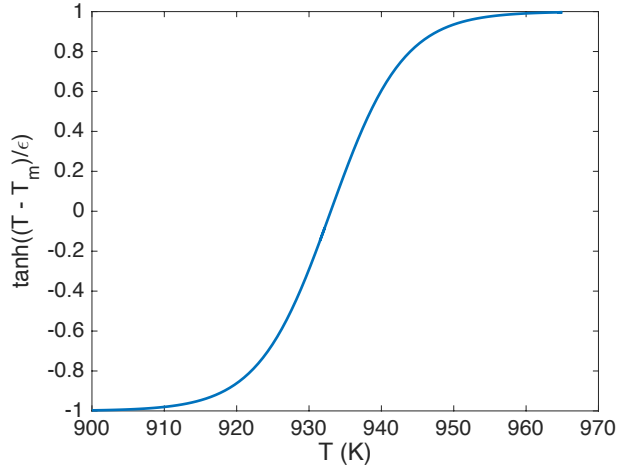
Figure 4.5: Function used to make phase change in reaction rate continuous. The graph presented here represents phase change in Al.

sample ignition event was chosen to find the reaction zone length. In Figure 4.6 (left), we see that the length of reaction zone is approximately 100 μm. Therefore, we constructed a computational domain (1-D slab) with a mixing region between the reactants approximately equaling 100 μm. Therefore the initial condition for species is:

$$Y_1(x, t = 0) = \frac{1}{2} \left(1 - tanh(30(x - 0.15))\right) \tag{4.31}$$

$$Y_3(x, t = 0) = \frac{1}{2} \left(1 - tanh(30(x - 0.15))\right) \tag{4.32}$$

$$Y_i(x, t = 0) = 0 \, (i \neq 1, 3) \tag{4.33}$$

The temperature across the domain is set at room temperature initially.

Due to conservation of mass, which neglects infulx/outflux of species outside of the domain, we set the boundary condition at both ends to be:

$$\frac{dY_i}{dx}\big|_{x=0} = 0 \tag{4.34}$$

$$\frac{dY_i}{dx}\big|_{x=l} = 0 \tag{4.35}$$
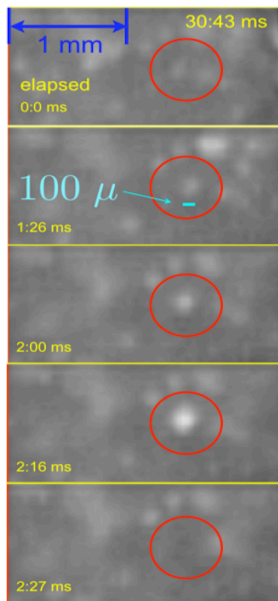
Figure 4.6: A sample ignition/quenching event is presented with the reaction length being 100 μm (left). A representative sample of 10 ignition/quenching event in normalized intensity vs time (right) [7].
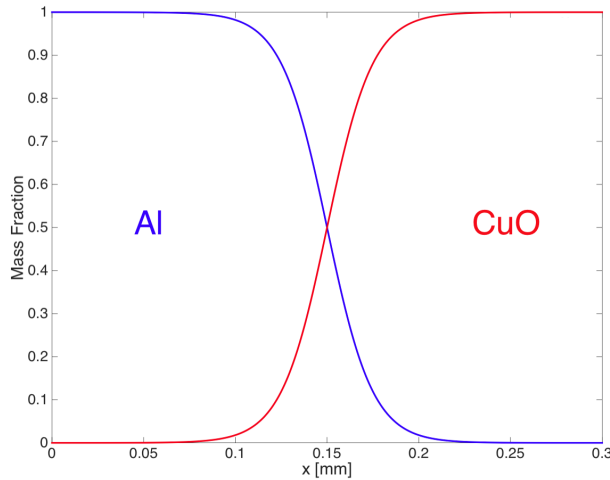
Figure 4.7: Slab domain characterization of the profile between initial reactants

We chose two different types of boundary condition for temperature; 1. 3000K at the left-end, 2. 2000K at the left-end. Both of them have adiabatic conditions at the right-end. These two cases display different physics, which will be discussed in the upcoming sections.
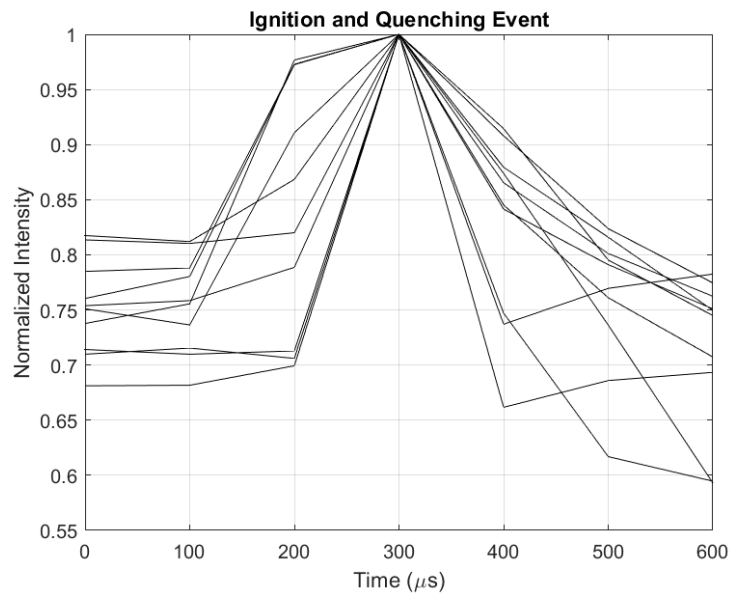
The reaction and melting/freezing rates for the set of proposed reaction in this chapter are not well known to our knowledge. Therefore, we have assumed that at high temperatures, the melting and reaction rate coefficients are equal to each other. This rate is then found by matching the ignition time in experiments, which is shown in Figure 4.6 (right). To capture the ignition time of approximately 100 μs, the rate coefficient (k_i) need to be approximately 500 mol/(mm^3 ms).

4.5.2 Comparison between numerical solution and experimental results

The first attempt at simulation of Al-CuO thermite combustion was to pick a thermal impulse which is larger than all melting temperatures of constitutive species. Therefore, a temperature of 3000K is used as a boundary condition at the left end in Figure 4.8. In Figure 4.8a, we see that aluminum starts melting due to the thermal impulse and diffusion has caused an increase in temperature across the domain. CuO has not started to melt because the temperature is not high enough yet. As time passes (Figure 4.8b), the temperature diffusion ensures that almost all the aluminum has melted.
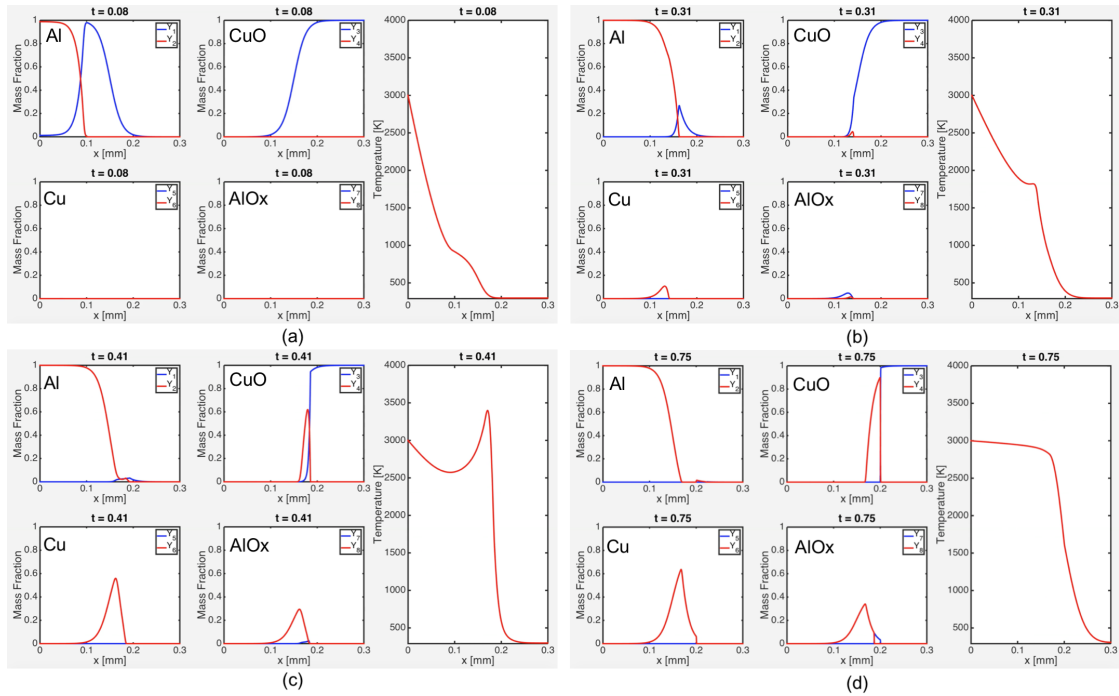
Figure 4.8: Image sequence of ignition/quenching simulation for the initial temperature case of 3000K

The temperature increase has also started to melt CuO, which results in the start of the reaction and production of Cu and AlOx. The onset of ignition is observed in the temperature profile due to exothermic nature of the reaction. Because of the chosen reaction rate coefficient observed from experiments, the total ignition time is approximately 100 μs (as seen Figure 4.8c). At this point, the maximum temperature is seen to be 3500K. Due to the stoichiometric ratio, it is observed that there is more Cu produced than AlOx. Due to the low thermal diffusivity of CuO and high thermal diffusivity of Al, temperature to the left of ignition increases at a significiantly faster pace than the CuO portion of the domain. The thermal spike due to ignition rapidly disappears by the quenching event. After the initial fast quenching, the rate at which the temperature decreases is considerably lowered due to thermal diffusivity of CuO.

By analyzing the local maximum temperature near the ignition event, the rapid ignition/quenching event can be easily observed, as seen in Figure 4.9. This graph is divided into four regions: 1) pre-

75
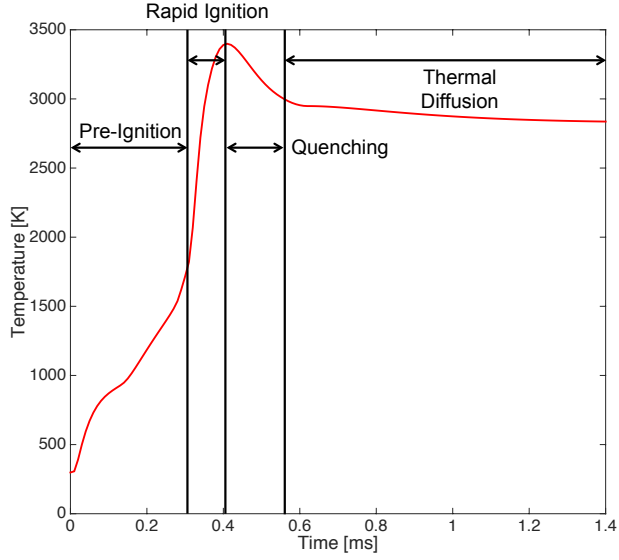
Figure 4.9: Local maximum temperature around ignition vs time for the initial temperature case of 3000K

ignition 2) rapid ignition 3) quenching 4) thermal diffusion. The pre-ignition event is the time until both Al and CuO melt. The rapid ignition and quenching correspond to the fast increase and decrease in temperature due to reaction and thermal diffusivity. The quenching even is characterized by:

$$\left| \frac{\frac{\partial T}{\partial t}|\mathrm{p.i}}{\frac{\partial T}{\partial t}|\mathrm{max}} \right| < 5\% \tag{4.36}$$

where, p.i stands for post ignition. Thus, the quenching time is approximately 170 μs. Finally, the thermal diffusion is where temperature equilibrates to the environment.

By decreasing the initial temperature to a value less than the melting temperature of AlOx, we can observe more phenomenon. Hence, a value of 2000K was chosen as the boundary condition at the left end in Figure 4.10. Due to the lower initial temperature, it can be clearly seen that it takes longer to melt both Al and CuO (Figure 4.10 a-b). This results in a longer pre-ignition event. When compared to 3000K case, the slightly lower ignition time and larger thermal spike is due to the local mixture at the interface (Figure 4.10 b-c). After fast quenching, the temperature is further lowered due to thermal diffusion. Eventually, the temperature drops below 2350K, which causes AlOx to
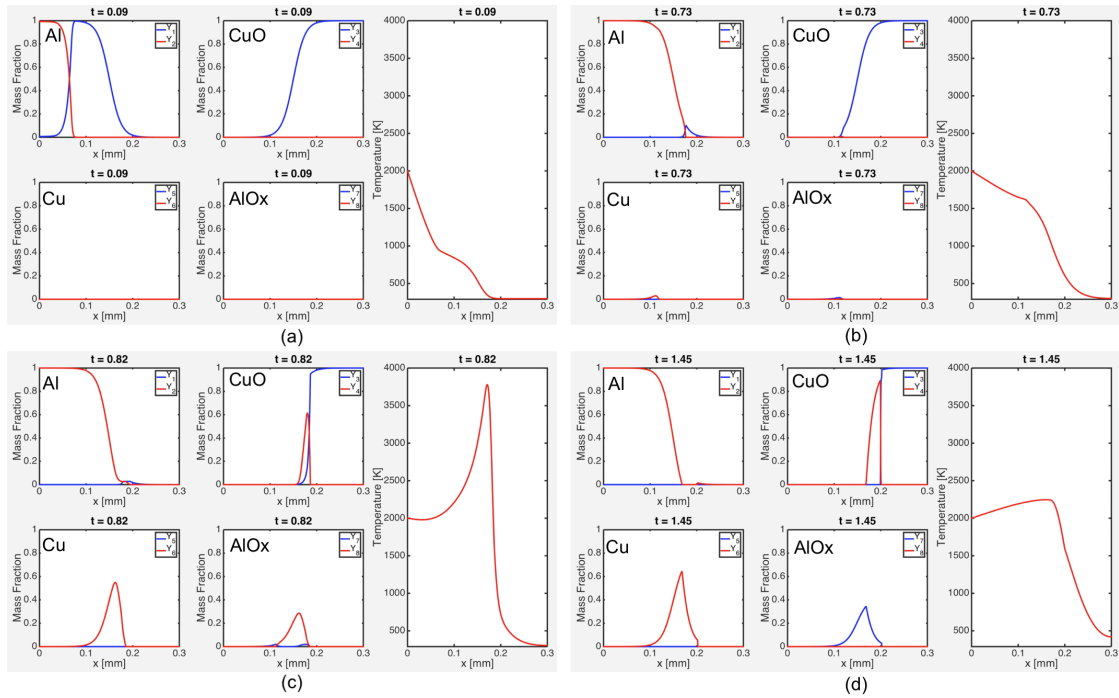
Figure 4.10: Image sequence of ignition/quenching simulation for the initial temperature case of 2000K

re-freeze (Figure 4.10 d). Similar to the 3000K case, we analyzed the local maximum temperature around ignition in Figure 4.11. We found the quenching time to be approximately 260 μs with Equation (4.36).

4.6   Conclusion

An experiment was performed using a stoichiometric thermite mixture aluminum (Al) and copper oxide (CuO), which are blended by hand and the ultrasonically mixed under hexane until consistency is achieved. The mixture is then cold pressed to achieve 80% TMD. The sample is ignited by two shock drivers with RP-80 detonators attached at the end of it. A Nikon AD-EF 80-200 is used to view the shock initiation of the reactive material. A Phantom 5 high speed imaging camera detector from Vision Research is used for this study. This is used to produce a series of images from
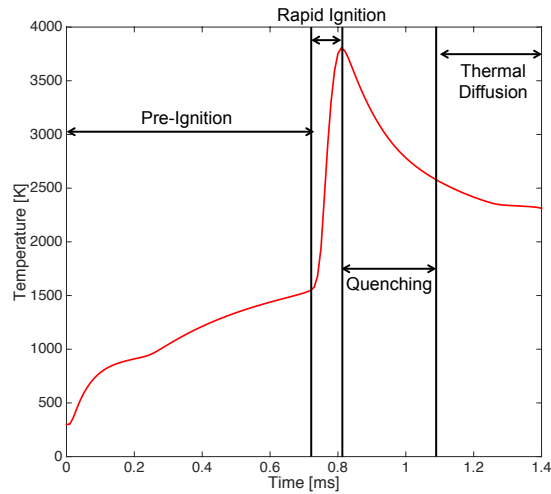
Figure 4.11: Local maximum temperature around ignition vs time for the initial temperature case of 2000K

an Al-CuO thermite test. The images show a propagating front with many fast igntion/quenching events (hot spots) behind it. An algorithm is used to compute the image intensity values around a localized small hot spot. From this analysis, we can see the ignition and quenching time of these events.

A multi-component multi-phase mixture theory is used to describe condensed phase ignition in Al and CuO reaction. The solid and liquid phase of each species is treated as a separate material. The phase change in materials is characterized as a reaction and incorporated in the reaction rate. Therefore, there are 8 species in the model which involve the solid and liquid phase of Al, CuO, Cu and AlOx. The reaction takes place when both Al and CuO melt to produce liquid copper and either solid or liquid AlOx. The Maxwell-Stefan (MS) model for multicomponent mixtures is informed by the binary diffusivities of any pair of species comprising the mixture. The use of MS relations is quite complicated because of the nonlinear relationship between diffusion velocities and concentration gradients. To simplify the analysis, we assume that there is no solid-solid diffusion and that all solid-liquid diffusion are equal while all liquid-liquid diffusion are equal. By analyzing a sample hot spot, we picked a slab domain with the reaction region between the initial reactants

equaling 100 μm. The ignition time seen in the experiment is used to characterize the reaction rate coefficients.

The ignition event is modeled by a thermal impulse set at the left end of the boundary with an adiabatic condition on the other end. Two different thermal impulse was analyzed: 3000K and 2000K. In each of these cases, Al and CuO melt and react to produce an ignition event and the maximum flame temperature observed is around 3500K. To compare the simulation with the experiment, the local maximum temperature near the ignition event is plotted as a function of temperature. The plots are separated into 4 regions: pre-ignition, rapid ignition, quenching and thermal diffusion. The quenching time for the 3000K and 2000K case are 170 μs and 260 μs respectively, which are within the observed experiment region. The ignition is characterized by the reaction rates while quenching is due to the thermal diffusivity of local mixture. In the 2000K case, once sufficient time has passed post ignition, the AlOx re-freezes from liquid to solid due to low temperature. The model presented in this chapter matches well with experimental data and could be used to predict hot spots in condensed phase reactive material simulations that captures both phase change and material diffusion. The analysis of ignition can be made more accurate by choosing to include pressure variations. Also, the initial conditions could be fine tuned to better capture the scenario which exists after the reaction front passes through the Al/CuO sample.

Chapter 5

Summary and Future Work

This dissertation proposes a model and computational framework for ignition and extinction in condensed phase combustion. The theory proposed here is based on a recently developed Gibbs formulation [54], and it is expanded to analyze ignition and extinction in initially separated reactants. The model takes into account phase change, multiple species as well as inter-species diffusion. The chapters presented in this thesis describe the model as it is carried out at increasing levels of complexities.

The second chapter analyses extinction due to strain rate in counterflow gas combustion. An asymptotic approximation to governing equations at large activation energy is compared with numerical solution for constant and variable density formulations. A low Mach number approximation is used, which accounts for small pressure variations from the ambient state. The analysis is carried out for large/small Lewis number and mixture strength variations. The asymptotic approximation is shown to match well with numerical solutions for all cases considered.

The thrid chapter explores the effect of strain rate in counterflow condensed phase combustion with application to Titanium/boron system. There are only three species and the reaction is modeled as a one-step Arrhenius kinetics. The traditional Fickean diffusion model is informed by binary diffusion constants that are defined by the Maxwell-Stefan model of diffusion. Through asymptotic analysis we have made an estimate of these diffusion coefficients that are consistent with respect to macroscopically observed adiabatic flame temperatures. A constant density approximation is first analyzed to understand the behavior of the diffusion model. Finally, the full flow problem is computed with varying density. The model is able to predict reaction zone length at varying strain rates and the criteria for extinction.

Finally, the fourth chapter extends the theory presented in chapter 3 to incorporate multiple reactions and phase change. This theory is applied to understand the fast ignition/quenching event witnessed in aluminum/copper oxide experiments [7]. The solid and liquid phase of each species is treated as a separate material. By analyzing a sample hot spot, a slab domain is picked with the reaction region between the initial reactants equaling 100 μm. The ignition event is modeled by a thermal impulse at the aluminum side of the boundary. The ignition time in the experiment is used to characterize the reaction rate coefficients. The phase change in materials is characterized as a reaction and incorporated in the reaction rate. The simulation is shown to closely match the ignition/quenching time seen in the experiments.

The research presented here lays the foundation for analysis of condensed phase combustion. These models can easily be transitioned to 2D and 3D geometries. A full shock ignited hot spot formulation simulation must be carried out to understand the full mechanics of such energetic materials. Some systems of interest include TATB, HMX, RDX, and Al/Al_2O_3. In particular, the aluminum droplet combustion is generating interest in the scientific community. The interaction between aluminum and oxygen and the formation of oxide layer is key for many applications.

For many materials of interest, the experimental data required for running such simulations are scarce. Therefore, data derived from Molecular Dynamics (MD) simulations is a good approach to filling this gap. For example, a mirrored atomistic and continuum framework is used to describe the ignition of energetic materials at high-pressure phase of RDX [67]. The model presented in this thesis, in conjunction with the method presented by Lee et al. [67], can be instrumental in tackling the current needs of the energetic materials community.

Appendix A

Application of Gibbs Free Energy Equation of State

A.1 Formulation

The Gibbs free energy equation of state, proposed by Fried and Howard [68] is based on an explicit functional form for G(P,T), which yields accurate results for pressures between $0 \leq P \leq 600$ GPA, and temperatures between $300K \leq T \leq 15,000K$:

$$G\left(P,T\right) = G_0\left(T\right) + \Delta G\left(P,T\right)$$

Where, G_0 is the reference portion while ΔG is the equation of state portion of the EOS. The reference portion is defined as follows:

$$G_0\left(T\right) = H_0\left(T\right) - TS_0\left(T\right)$$

The functions $H_0(T)$ and $S_0(T)$ are expressed in terms of the constant pressure heat capacity, $C_{p,0}(T)$, at 1 atm.

$$H_0\left(T\right) = \Delta H_0 + \int_{T_0}^{T} C_{P,0}\left(T\right)\,\mathrm{d}T$$

and

$$S_0\left(T\right) = \Delta S_0 + \int_{T_0}^{T} \frac{C_{P,0}\left(T\right)}{T}\,\mathrm{d}T$$

ΔH_0 and ΔS_0 are the standard entropy and standard enthalpy of formation at $T_0 = 298K$. The specific heat at constant pressure is represented by the sum of two Einstein oscillators and a linear

term:
$$C_{P,0}(T) = \sum_{i=1}^{2} a_i E\left(\frac{\Theta}{T}\right) + a_3 T$$

Where the Einsten form is represented as,

$$E(x) = \frac{x^2 \exp(x)}{(\exp(x) - 1)^2}$$

Thus, we have:

$$H_0(T) = \Delta H_0 + \sum_{i=1}^{2} a_i \theta_i \left[\frac{1}{\exp(x) - 1}\right]_{(x_{i0})}^{(x_i)} + a_3 T$$

and

$$S_0(T) = \Delta S_0 + \sum_{i=1}^{2} a_i \left[\frac{x}{\exp(x) - 1} - \log(1 - \exp(x))\right]_{x_{i0}}^{x_i} + a_3(T - T_0)$$

We have now completely defined $G_0(T)$. Now we must obtain an equation for $\Delta G(P,T)$, the EOS portion. Since $dG = V dP - S dT$, $\Delta G(P,T)$ is defined by estimating a form for $V(P,T)$:

$$\Delta G(P,T) = \int_{P_0}^{P} V(P,T) \, dP$$

Where, $V(P,T)$ is the modified Murnaghan form:

$$V(P,T) = V_0 \left(n\kappa_0 P + f(T)\right)^{-1/n}$$

Where, κ_0 is the inverse of Bulk modulus at room temperature and n is the first derivative of the Bulk modulus. The functional form of $f(T)$ is chosen to reproduce the thermal expansion of the material at zero pressure. The following form is suggested to by Fried:

$$f(T) = \exp\left[-n(g(T) - g(T_0))\right]$$

Where,

$$g(T) = \alpha_0 T + \alpha_1 \left(T - \frac{T^*}{2}\{\exp[-T/T^*] - 2\}^2\right)$$

83

Thus, we find an expression for $\Delta G(P,T)$:

$$\Delta G(P,T) = \frac{V_0}{(n-1)\kappa_0}[\eta^{n-1} - \eta_0^{n-1}]$$

Where,

$$\eta = \frac{V_0}{V} = [n\kappa_0 P + f(T)]^{1/n}$$

We define η_0 as $\eta_0 = \eta(T, P_0)$.

The coefficient of thermal expansion is found to be:

$$\alpha = \frac{1}{V}\frac{\partial V}{\partial T}\bigg|_P = g'(T)\eta^{-n}f(T)$$

For small expansion and when $T << 1/\alpha$, $\eta \approx 1$, and $f(T) \approx 1$. Thus, we can determine that the thermal expansion is dominated by $g'(T)$. In order to accurately model the coefficient of thermal expansion, $g'(T)$ is chosen as:

$$g'(T) = \alpha_0 + \alpha_1(1 - \exp[-T/T^*])^2$$

As we can see, this function increases from α_0 to $\alpha_1 + \alpha_0$ as T increases from 0 to ∞. The rate of increase is controlled by T^*, which makes it easy to program and model any given thermal expansion data.

Thus, we can use the following steps to calculate all the necessary parameters for the EOS:

Step 1: Find the standard heat of formation and standard entropy values for the given state of the material. Fit the constant pressure heat capacity values to the following equations:

$$C_{P,0}(T) = \sum_{i=1}^{2} a_i E\left(\frac{\Theta}{T}\right) + a_3 T$$

$$E(x) = \frac{x^2 \exp(x)}{(\exp(x) - 1)^2}$$

This will gives us, ΔH_0, ΔS_0, a_0, a_1, a_3, θ_1, and θ_2.

84

Step 2: Find the Bulk Modulus and its pressure derivative, B_0 and n, from a room temperature isotherm. If these terms were debated, we can fit the modified Murnaghan EOS to the isotherm to determine the two parameters:

$$V(P,T) = V_0 (n\kappa_0 P + 1)^{-1/n}$$

Thus, we can find V_0, B_0 and n.

Step 3: The coefficient of thermal expansion is modeled by:

$$\alpha = \frac{1}{V} \left.\frac{\partial V}{\partial T}\right|_P = g'(T)\eta^{-n}f(T)$$

$$g'(T) = \alpha_0 + \alpha_1(1 - \exp[-T/T^*])^2$$

Thus, we can get α_0, α_1 and T^*.

With all the parameters now found, it would be a simple matter to construct the phase diagram for any material. The phase boundaries and transition is governed by the chemical potential, μ. For a one component system, the molar Gibbs energy, G_m, and the chemical potential are equal. A system wanted to have the lowest Gibbs energy possible for any given P and T. The slope of phase transition is given by the Clapeyron equation:

$$\frac{dP}{dT} = \frac{\Delta S_m}{\Delta V_m} = \frac{S_{\beta,m} - S_{\alpha,m}}{V_{\beta,m} - V_{\alpha,m}}$$

We can set:
$$\left(\frac{\partial G_m}{\partial T}\right)\bigg|_P = -S_m$$

$$\left(\frac{\partial G_m}{\partial P}\right)\bigg|_T = V_m$$

For any phase α and β to be in equilibrium, we must have:

$$\mu_\alpha(P,T) = \mu_\beta(P,T)$$

85

An example phase diagram of carbon derived using this method is shown in Figure A.1.
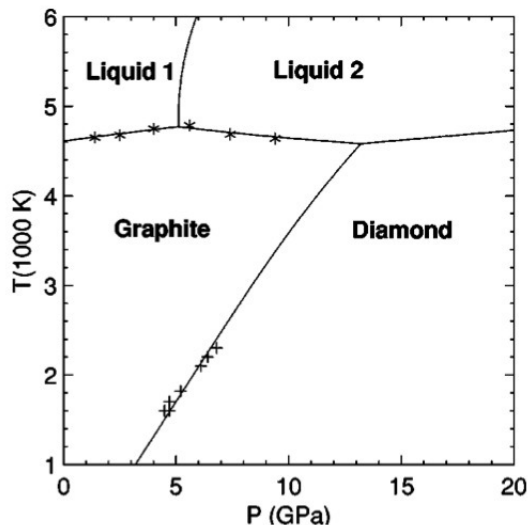

Figure A.1: Phase Diagram of Carbon [68]

A.2   Equation of state of Aluminum

In this section, we will focus on the results of applying this EOS procedure to Aluminum. We have one solid phase and one liquid phase and the parameters are found in the literature. The matching between the thermal expansion is given below, as well as the matching between constant pressure heat capacity models. The models are fit to a high degree of precision ($r^2 > 0.99$). The algorithm for fitting the model to experiment is derived by iterating various values for the fitting parameters and then calculating the r^2 values of each of these iterations. The range of values accepted for each of these fitting parameters is predicted through the values used for Carbon. These procedures are similarly replicated for liquid Aluminum as well. For liquid Aluminum, we could not find the data for coefficient of thermal expansion. Instead, we used thermal expansion data at constant pressure to find the necessary fitting parameters.

Figures A.2 and A.3 show the thermal expansion and constant pressure heat capacity graph
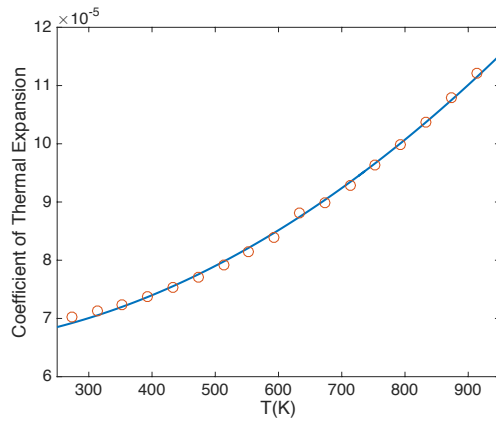
Figure A.2: EOS - Thermal expansion fit to experimental data [69] for solid Aluminum at 1 atm
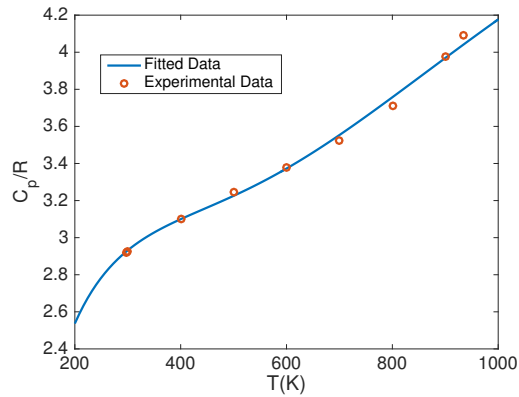

Figure A.3: EOS - Constant pressure heat capacity fit to experimental data [46] for solid Aluminum

for solid Aluminum. Figures A.4 and A.5 show the thermal expansion and constant pressure heat capacity graph for liquid Aluminum. The density, bulk modulus and pressure derivative were found in [71] and [72]. After following the procedure, we have found all the necessary values for Aluminum and they are given below in Tables A.1 and A.2.

After finding the necessary values, it is relatively easy to solve for the Hugoniot and compare it to experiments performed by Marsh [73]. Both the solid and liquid model match the Hugoniot well, as seen in Figures A.6 and A.7, thus validating this approach. Since the bulk modulus and
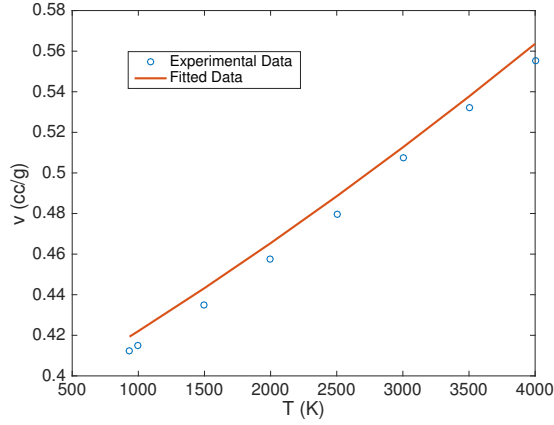
Figure A.4: EOS - Thermal expansion fit to experimental data [70] for liquid Aluminum at 1 atm
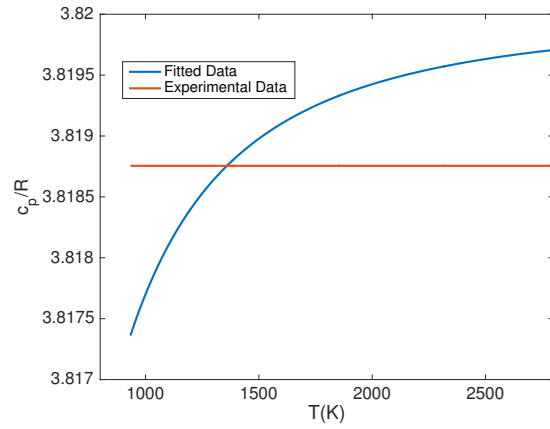
Figure A.5: EOS - Constant pressure heat capacity fit to experimental data [46] for liquid Aluminum

Phase	V_0(cc/mol)	B_0(GPa)	n	α_0 (K^{-1})	α_1 (K^{-1})	T^*(K)
Solid	9.99 [55]	72.7 [72]	4.3 [72]	6.5×10^{-5}	17.01×10^{-2}	54815
Liquid	11.36 [70]	72.7	4.3	-0.99×10^{-2}	1.0×10^{-2}	94

Table A.1: EOS values for Aluminum

its pressure derivative are not known for liquid-Al, they are assumed to be equal to the solid-Al values. The solid-Al Hugoniot matches the experiment well for lower pressures while the liquid-Al

88
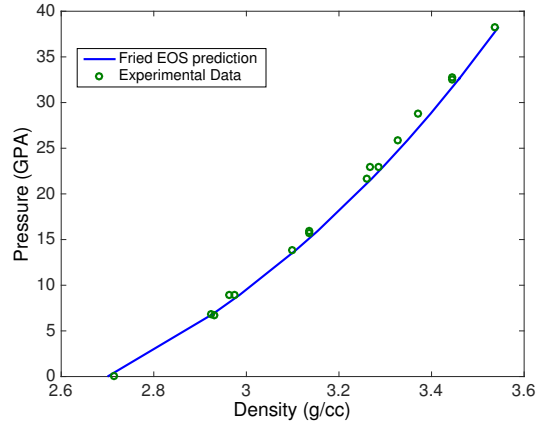
Figure A.6: Hugoniot comparison between Fried-Howard EOS prediction to experimental data [73] for solid Aluminum
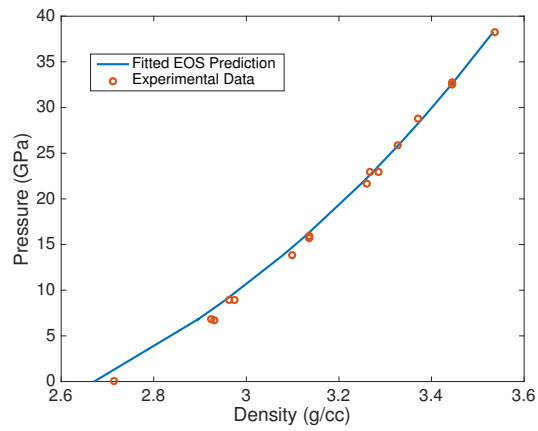
Figure A.7: Hugoniot comparison between Fried-Howard EOS prediction to experimental data [73] for liquid Aluminum

Phase	ΔH_0(kJ/mol)	ΔS_0(J/mol K)	a_1/R	θ_1 (K)	a_2/R	θ_2 (K)	a_3/R
Solid	0 [46]	28.3 [46]	3.3	360	3	4000	0
Liquid	28.837 [46]	71.408 [46]	3.82	85	0	0	0

Table A.2: Reference values for Aluminum

Hugoniot matches the experiment well for higher pressures.

The next step is to calculate the phase diagram for Aluminum but they are not presented here because the temperature calculated does not seem to be the correct temperature. Once this issue is resolved, we can easily compute this phase diagram and find the transition line between solid and liquid Al and match it to experiments.

A.3   Equation of state of Aluminum Oxide

Solid Al_2O_3:

- The coefficient of thermal expansion data is used to get α_0, α_1 and T^* for this phase of Al_2O_3 [74]. It is compared in Figure A.8.

- The constant pressure heat capacity data is used to get a_1, θ_1, a_2, θ_2, and a_3 [46]. This graph is shown in Figure A.9.

- From literature, we are able to find the bulk modulus and its pressure derivative for this phase [75].

- Using this EOS, we are able to compare the shock Hugoniot produced by this model with the experiments by Marsh [73]. This graph is shown in Figure A.12.

- The standard heat of formation and standard entropy is given in literature [76].

Liquid Al_2O_3:

- The thermal expansion data is used to get α_0, α_1 and T^* for this phase of Al_2O_3 [77]. It is compared in Figure A.10.

- The constant pressure heat capacity data is used to get a_1, θ_1, a_2, θ_2, and a_3 [46]. This graph is shown in Figure A.11.

- The bulk modulus and its pressure derivative are found in literature [78].

- Using this EOS, we are able to compare the shock Hugoniot produced by this model with the experiments [73]. This graph is shown in Figure A.12.

- The standard heat of formation and standard entropy is given in literature. Al_2O_3 melts at 2360 K [76].

The final EOS and reference tables for Boron(both liquid and solid) that contains all the parameters for the Fried EOS are listed in Tables A.3 and A.4.
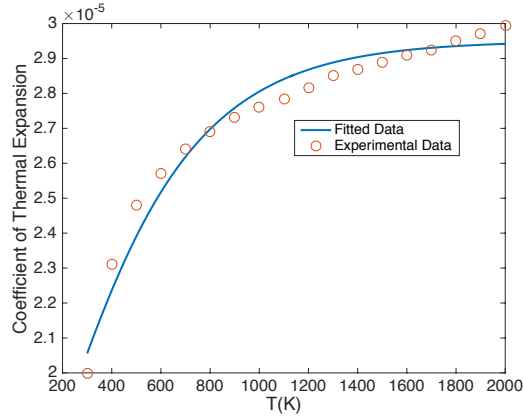

Figure A.8: EOS - Thermal expansion fit to experimental data [74] for solid Al_2O_3 at 1 atm

Phase	V_0(cc/mol)	B_0(GPa)	n	α_0 (K^{-1})	α_1 (K^{-1})	T^*(K)
Solid	25.64 [74]	255.9 [75]	4.92 [75]	1.6×10^{-5}	1.35×10^{-5}	345
Liquid	29.55 [77]	36 [78]5	9.27 [78]	-178×10^{-5}	214×10^{-5}	410

Table A.3: EOS values for Al_2O_3

Phase	ΔH_0(kJ/mol)	ΔS_0(J/mol K)	a_1/R	θ_1 (K)	a_2/R	θ_2 (K)	a_3/R
Solid	-1675.7 [76]	51 [76]	5	250	10	950	0.8×10^{-3}
Liquid	-1620.6 [76]	67.3 [76]	23.15	96	0	0	0

Table A.4: Reference values for Al_2O_3
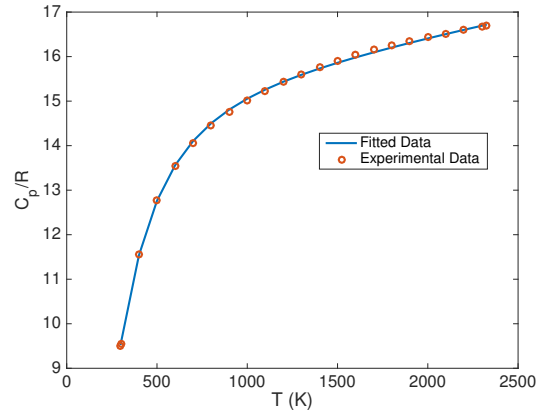
Figure A.9: EOS - Constant pressure heat capacity fit to experimental data [46] for solid Al_2O_3
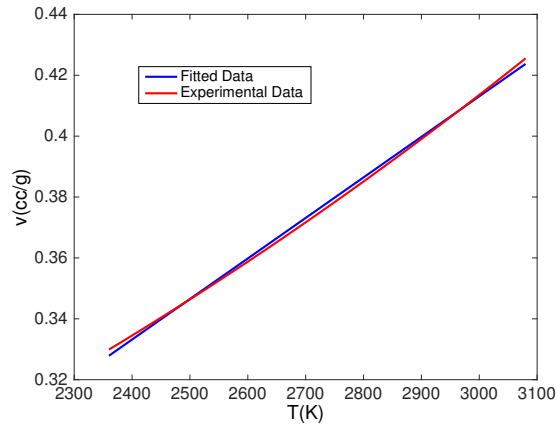
Figure A.10: EOS - Thermal expansion fit to experimental data [77] for liquid Al_2O_3 at 1 atm

A.4 Equation of state of Titanium

Solid Titanium (α):

- The coefficient of thermal expansion data is used to get α_0, α_1 and T^* for this phase of Titanium [79]. It is compared in Figure A.14.

- The constant pressure heat capacity data is used to get a_1, θ_1, a_2, θ_2, and a_3 [46]. This graph

Figure A.11: EOS - Constant pressure heat capacity fit to experimental data [46] for liquid Al_2O_3

Figure A.12: Hugoniot comparison between Fried-Howard EOS prediction to experimental data [73] for solid Al_2O_3

is shown in A.15.

- From literature, we are able to find the bulk modulus and its pressure derivative for this phase [80].

- Now, we are able to compare the shock Hugoniot produced by this model with the experiments [73]. This graph is shown in A.20.

Figure A.13: Hugoniot comparison between Fried-Howard EOS prediction to experimental data [73] for liquid Al_2O_3

- The standard heat of formation and standard entropy is given in literature [76].

Solid Titanium (β):

- The thermal expansion data is used to get α_0, α_1 and T^* for this phase of Titanium [81]. It is compared in Figure A.16.

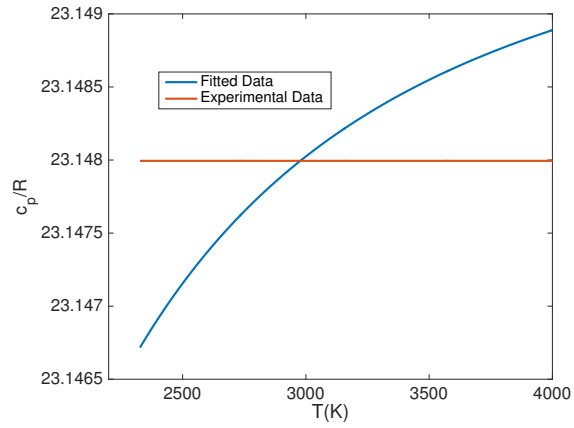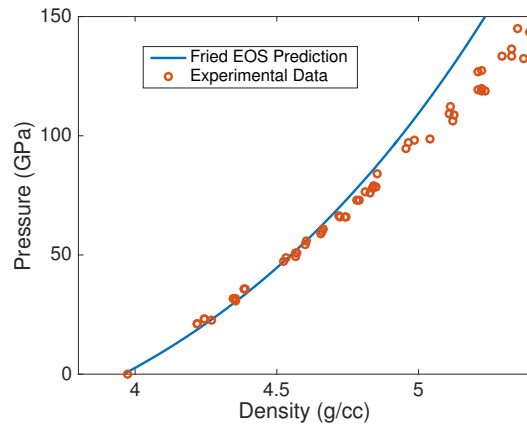- The constant pressure heat capacity data is used to get a_1, θ_1, a_2, θ_2, and a_3 [46]. This graph is shown in Figure A.17.

- From literature, we are able to find the bulk modulus and its pressure derivative for this phase [80].

- Using this EOS, we are able to compare the shock Hugoniot produced by this model with the experiments [73]. This graph is shown in Figure A.21.

- The standard heat of formation and standard entropy is given in literature. α-Ti goes to β-Ti at 1166 K [76].

Liquid Titanium:

- The thermal expansion data is used to get α_0, α_1 and T^* for this phase of Titanium [81]. It is compared in Figure A.18.

- The constant pressure heat capacity data is used to get a_1, θ_1, a_2, θ_2, and a_3 [46]. This graph is shown in Figure A.19.

- The bulk modulus and the pressure derivative is assumed to be same as the one for β-Titanium.

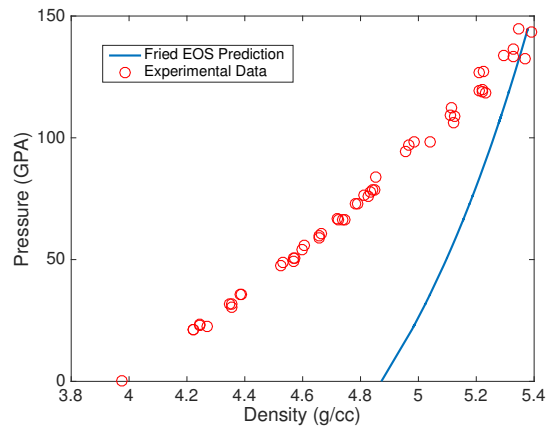- Thus, we are able to compare the shock Hugoniot produced by this model with the experiments [73]. This graph is shown in Figure A.22.

- The standard heat of formation and standard entropy is given in literature. β-Ti goes to liquid Ti at 1939 K [76].

The final EOS and reference tables for Titanium(both solid and liquid) that contains all the parameters for the Fried EOS are listed in Tables A.5 and A.6.
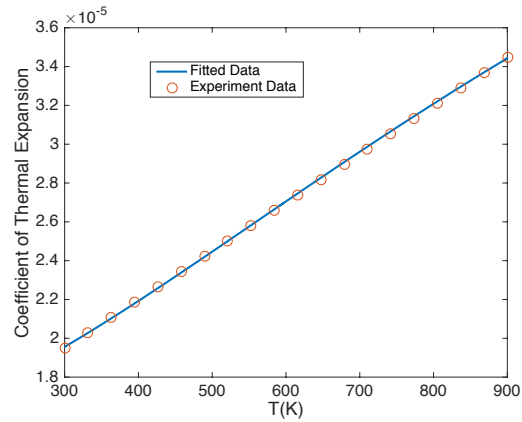
Figure A.14: EOS - Thermal expansion fit to experimental data [79] for solid α-Titanium at 1 atm

A.5   Equation of state of Boron

Solid Boron (β):

Figure A.15: EOS - Constant pressure heat capacity fit to experimental data to experimental data [46] for solid α-Titanium at 1 atm
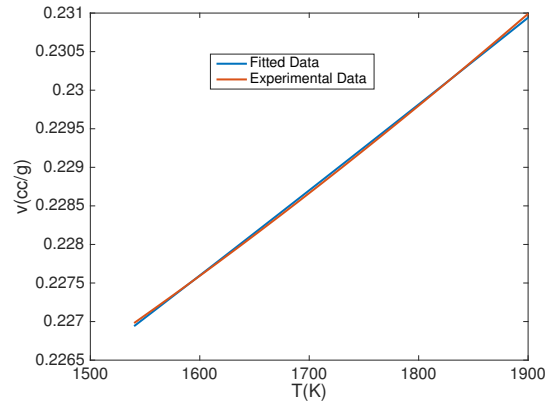
Figure A.16: EOS - Thermal expansion fit to experimental data [81] for solid β-Titanium at 1 atm

Phase	V_0(cc/mol)	B_0(GPa)	n	α_0 (K^{-1})	α_1 (K^{-1})	T^*(K)
α-Solid	10.574 [79]	110 [80]	3.48 [80]	1.55×10^{-5}	4.15×10^{-5}	800
β-Solid	10.596 [81]	105 [80]	3.25 [80]	-1.45×10^{-5}	8.65×10^{-5}	890
Liquid	11.38 [81]	105	3.25	-2.25×10^{-5}	15.45×10^{-5}	560

Table A.5: EOS values for Titanium

96
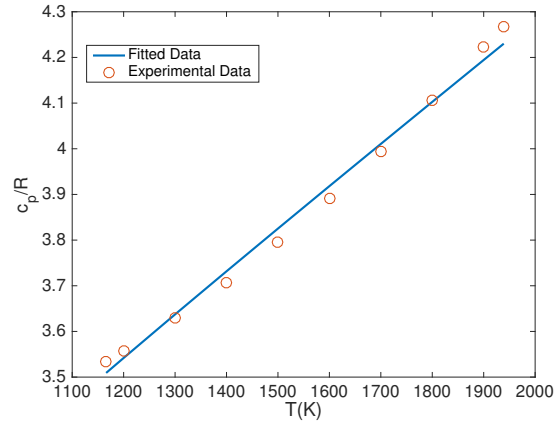
Figure A.17: EOS - Constant pressure heat capacity fit to experimental data to experimental data [46] for solid β-Titanium at 1 atm
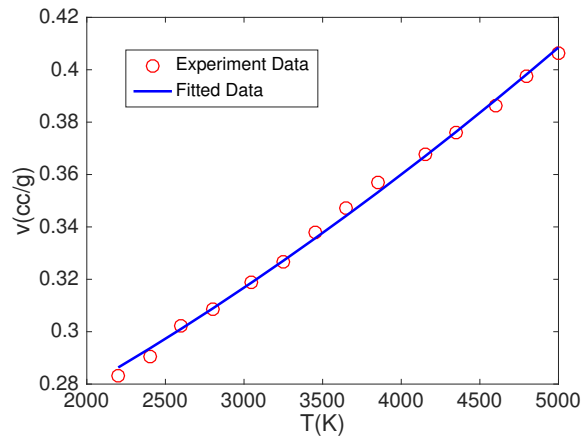
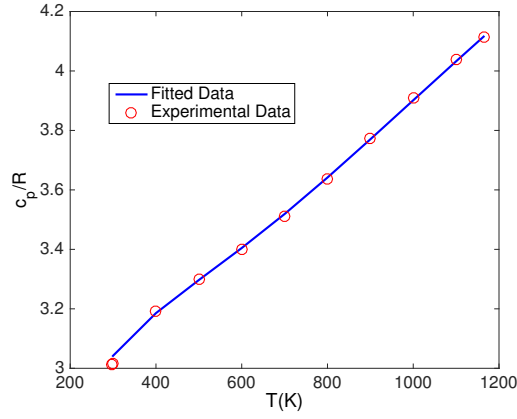Figure A.18: EOS - Thermal expansion fit to experimental data [81] for liquid Titanium at 1 atm

Phase	ΔH_0(kJ/mol)	ΔS_0(J/mol K)	a_1/R	θ_1 (K)	a_2/R	θ_2 (K)	a_3/R
α-Solid	0 [76]	30.759 [76]	3	250	1	4600	0.7×10^{-3}
β-Solid	26.8 [76]	70.8 [76]	2	115	0.5	1150	0.9×10^{-3}
Liquid	66.7 [76]	94.8 [76]	5.7	465	0	0	0

Table A.6: Reference values for Titanium
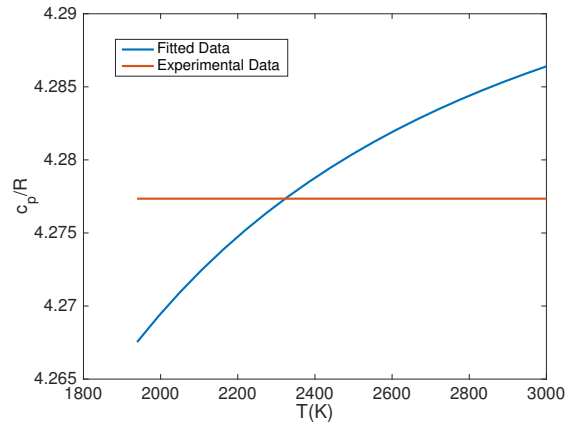
Figure A.19: EOS - Constant pressure heat capacity fit to experimental data to experimental data [46] for liquid Titanium at 1 atm
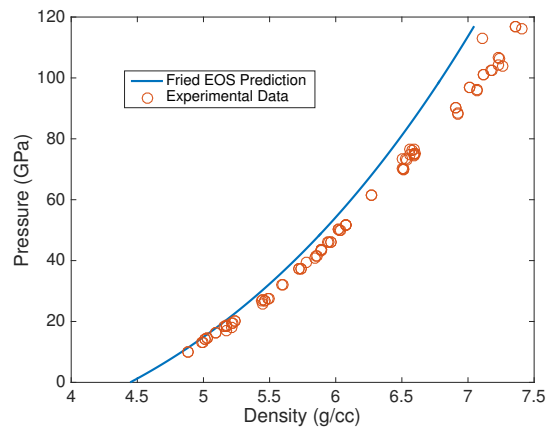
Figure A.20: Hugoniot comparison between Fried-Howard EOS prediction to experimental data [73] for solid α-Titanium

- The coefficient of thermal expansion data is used to get α_0, α_1 and T^* for this phase of Boron [82]. It is compared in Figure A.23.

- The constant pressure heat capacity data is used to get a_1, θ_1, a_2, θ_2, and a_3 [46]. This graph is shown in Figure A.24.

98
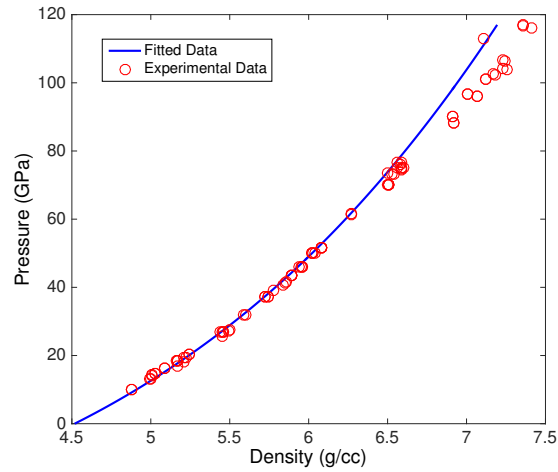
Figure A.21: Hugoniot comparison between Fried-Howard EOS prediction to experimental data [73] for solid β-Titanium
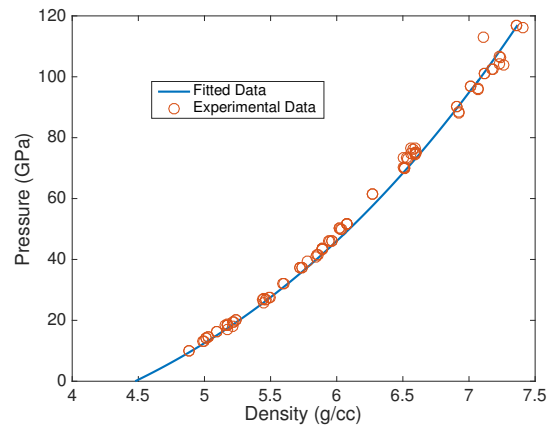
Figure A.22: Hugoniot comparison between Fried-Howard EOS prediction to experimental data [73] for liquid Titanium

- From literature, we are able to find the bulk modulus and its pressure derivative for this phase [83].

- Using this EOS, we are able to compare the shock Hugoniot produced by this model with the

experiments by Marsh [73]. This graph is shown in Figure A.27.

- The standard heat of formation and standard entropy is given in literature [76].

Liquid Boron:

- The coefficient of thermal expansion data is used to get α_0, α_1 and T^* for this phase of Boron [84]. It is compared in Figure A.25.

- The constant pressure heat capacity data is used to get a_1, θ_1, a_2, θ_2, and a_3 [46]. This graph is shown in Figure A.26.

- The bulk modulus and its pressure derivative are assumed to be the same as that of β-Boron.

- Using this EOS, we are able to compare the shock Hugoniot produced by this model with the experiments [73]. The experimental data is for titanium in general. This graph is shown in Figure A.27.

- The standard heat of formation and standard entropy is given in literature. Boron melts at 2349 K [76].

The final table for Boron(both liquid and solid) that contains all the parameters for the Fried EOS are listed in Tables A.7 and A.8.

Phase	V_0(cc/mol)	B_0(GPa)	n	α_0 (K^{-1})	α_1 (K^{-1})	T^*(K)
Solid	4.6 [82]	210 [83]	2.23 [83]	0.2×10^{-5}	2.45×10^{-5}	370
Liquid	4.982 [84]	210	2.23	5.65×10^{-5}	7.8×10^{-5}	1170

Table A.7: EOS values for Boron

Phase	ΔH_0(kJ/mol)	ΔS_0(J/mol K)	a_1/R	θ_1 (K)	a_2/R	θ_2 (K)	a_3/R
Solid	0 [76]	50.936 [76]	2.5	970	0.3	980	0.4×10^{-3}
Solid	28.837 [76]	339.655 [76]	3.82	190	0	0	0

Table A.8: Reference values for Boron

Figure A.23: EOS - Thermal expansion fit to experimental data [82] for solid Boron at 1 atm
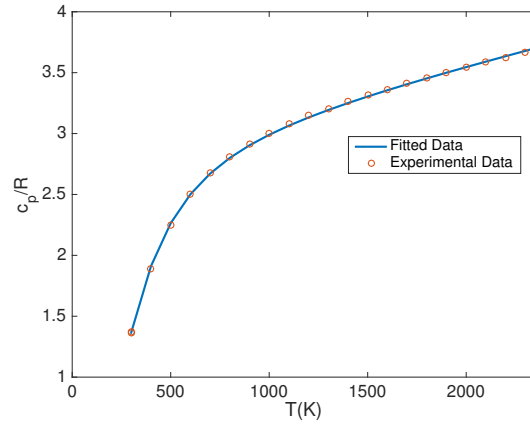
Figure A.24: EOS - Constant pressure heat capacity fit to experimental data [46] for solid Boron

A.6   Equation of state of Titanium Diboride

Solid TiB$_2$:

- The thermal expansion data is used to get α_0, α_1 and T^* for this phase of TiB$_2$ [85]. It is compared in Figure A.29.

- The constant pressure heat capacity data is used to get a_1, θ_1, a_2, θ_2, and a_3 [46]. This graph

Figure A.25: EOS - Thermal expansion fit to experimental data [84] for liquid Boron at 1 atm
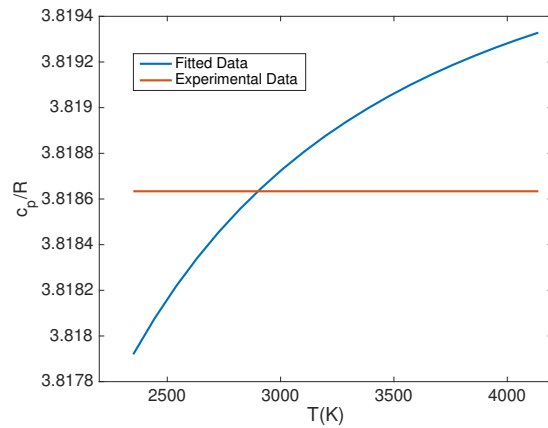
Figure A.26: EOS - Constant pressure heat capacity fit to experimental data [46] for liquid Boron

is shown in Figure A.30.

- From literature, we are able to find the bulk modulus and its pressure derivative for this phase [86].

- Using this EOS, we are able to compare the shock Hugoniot produced by this model with the experiments [73]. This graph is shown in Figure A.31.
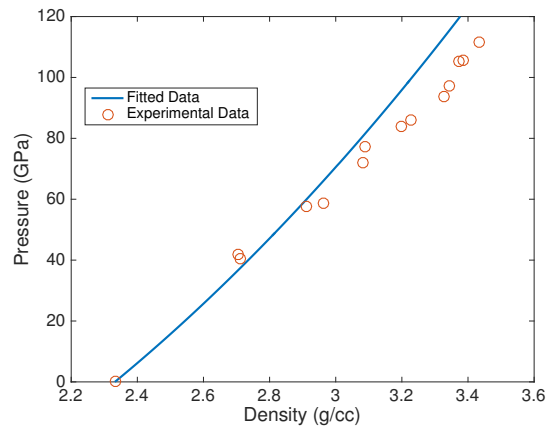
Figure A.27: Hugoniot comparison between Fried-Howard EOS prediction to experimental data [73] for solid β-Boron
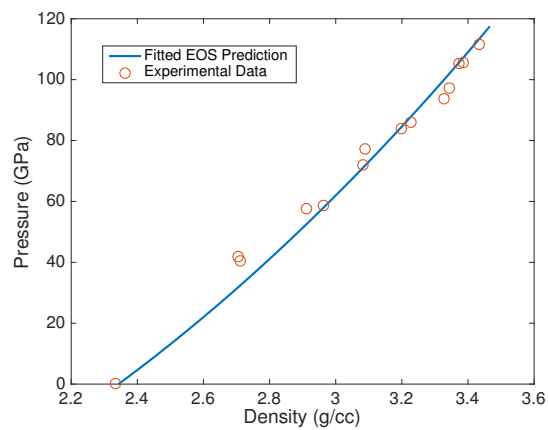
Figure A.28: Hugoniot comparison between Fried-Howard EOS prediction to experimental data [73] for liquid Boron

- The standard heat of formation and standard entropy is given in literature [76].

Liquid TiB$_2$:

- There is not enough data to conduct a complete EOS for this phase of TiB$_2$. Thus, this part will be updated as we get more data.

The final table for TiB$_2$ that contains all the parameters for the Fried EOS are listed in Tables A.9 and A.10.
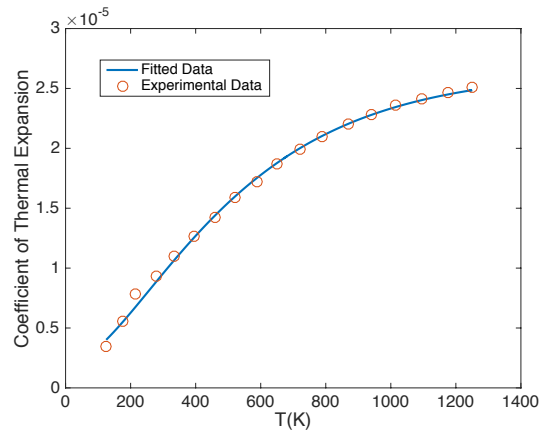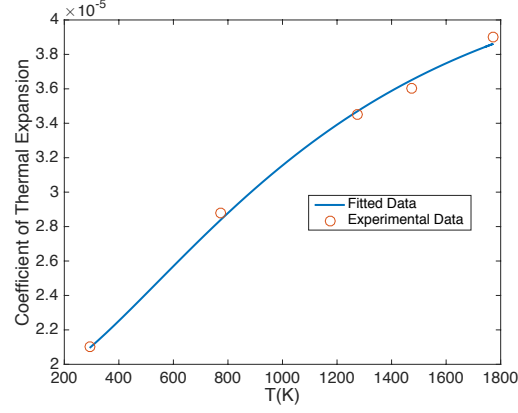

Figure A.29: EOS - Thermal expansion fit to experimental data [85] for solid TiB$_2$ at 1 atm
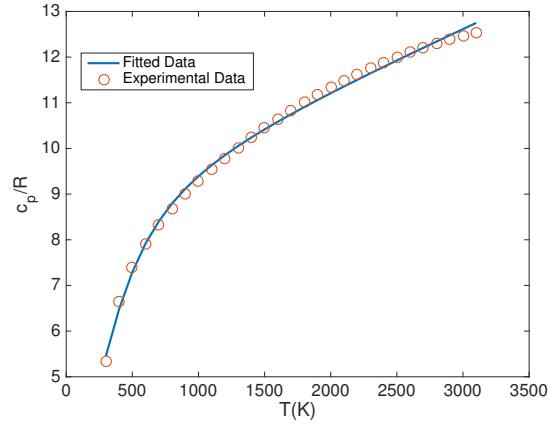
Figure A.30: EOS - Constant pressure heat capacity fit to experimental data [46] for solid TiB$_2$

Phase	V$_0$(cc/mol)	B$_0$(GPa)	n	α_0 (K^{-1})	α_1 (K^{-1})	T^*(K)
Solid	15.37 [49]	292 [86]	3.34 [86]	1.85×10^{-5}	2.5×10^{-5}	780

Table A.9: EOS values for TiB$_2$
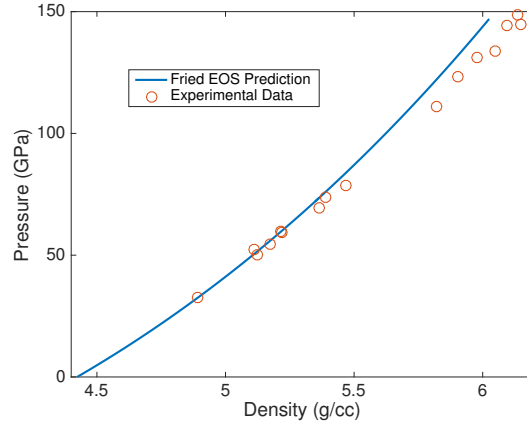
Figure A.31: Hugoniot comparison between Fried-Howard EOS prediction to experimental data [73] for solid TiB$_2$

Phase	ΔH_0(kJ/mol)	ΔS_0(J/mol K)	a_1/R	θ_1 (K)	a_2/R	θ_2 (K)	a_3/R
Solid	-315.9 [76]	28.5 [76]	5	360	3.8	1520	1.3×10^{-3}

Table A.10: Reference values for TiB$_2$

A.7 Equation of state of Titanium Monoboride

Solid TiB:

- The coefficient of thermal expansion data is used to get α_0, α_1 and T^* for this phase of TiB [87]. It is compared in Figure A.32.

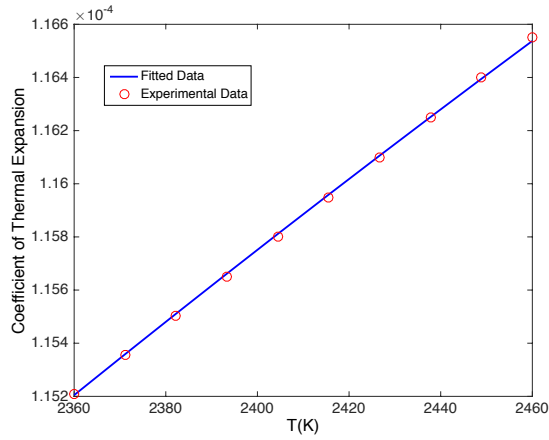- The constant pressure heat capacity data is used to get a_1, θ_1, a_2, θ_2, and a_3 [46]. This graph is shown in Figure A.33

- From literature, we are able to find the bulk modulus and its pressure derivative for this phase [87]. The reference density is given by Decker and Kasper [88].

- The experimental shock Hugoniot is not available for TiB. Hence, we make a prediction for Hugoniot in Figure A.34.

The final table for TiB_2 that contains all the parameters for the Fried EOS are listed in Tables A.11 and A.12.
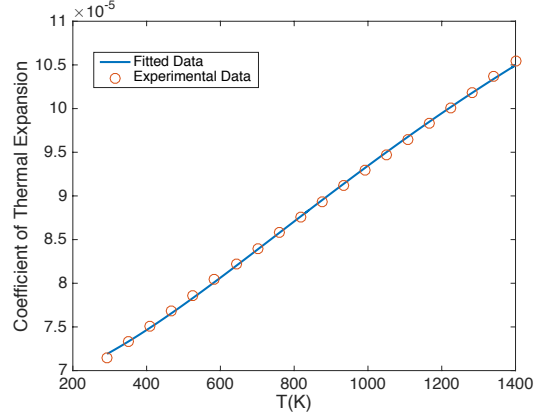
Figure A.32: EOS - Thermal expansion fit to experimental data [87] for solid TiB at 1 atm
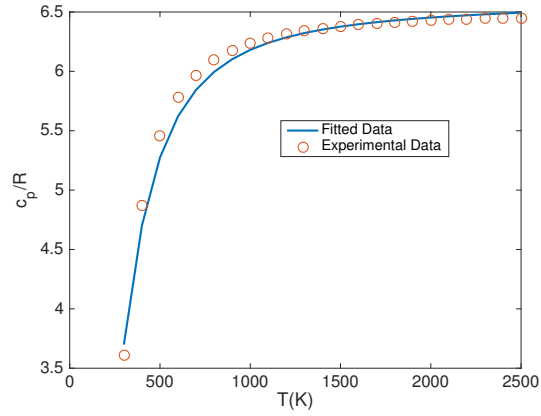
Figure A.33: EOS - Constant pressure heat capacity fit to experimental data [46] for solid TiB

Phase	V_0(cc/mol)	B_0(GPa)	n	α_0 (K^{-1})	α_1 (K^{-1})	T^*(K)
Solid	12.87 [88]	320 [87]	4 [87]	7.1×10^{-5}	6.8×10^{-5}	1095

Table A.11: EOS values for TiB

106
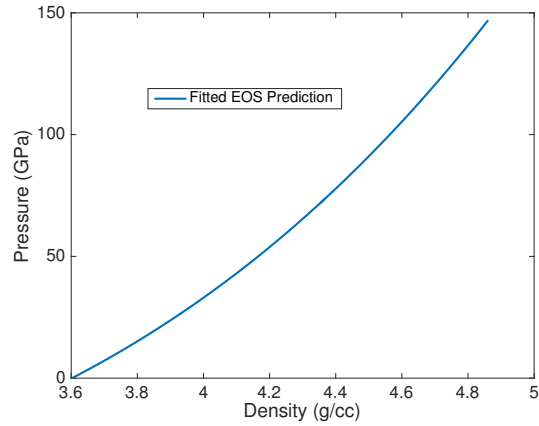
Figure A.34: Hugoniot Prediction for solid TiB

Phase	ΔH_0(kJ/mol)	ΔS_0(J/mol K)	a_1/R	θ_1 (K)	a_2/R	θ_2 (K)	a_3/R
Solid	-160.2 [46]	34.7 [46]	3.8	820	2.7	780	0.02×10^{-3}

Table A.12: Reference values for TiB

A.8 Phase diagram for Ti-B system

The experimental phase diagram for the Ti-B system is provided by Murray et al [89], shown in Figure A.35. The phase diagram depicts temperature as a function of molar fraction of Boron. There are other species included in Murray's work that we are not interested in, such as Ti_3B_4. By working with just four species (Ti, B, TiB_2, and TiB), the experimental phase diagram can be approximated using Fried and Howard's equation of state. This is done by minimizing the Gibbs free energy of the mixture. The mixture of species and phases which yields the lowest Gibbs free energy is the local stable state. Figure A.36 shows the comparison between the phase diagram predicted by Fried-Howard EOS and the experimental data. It is clear that Fried-Howard's EOS matches well with experimental data.
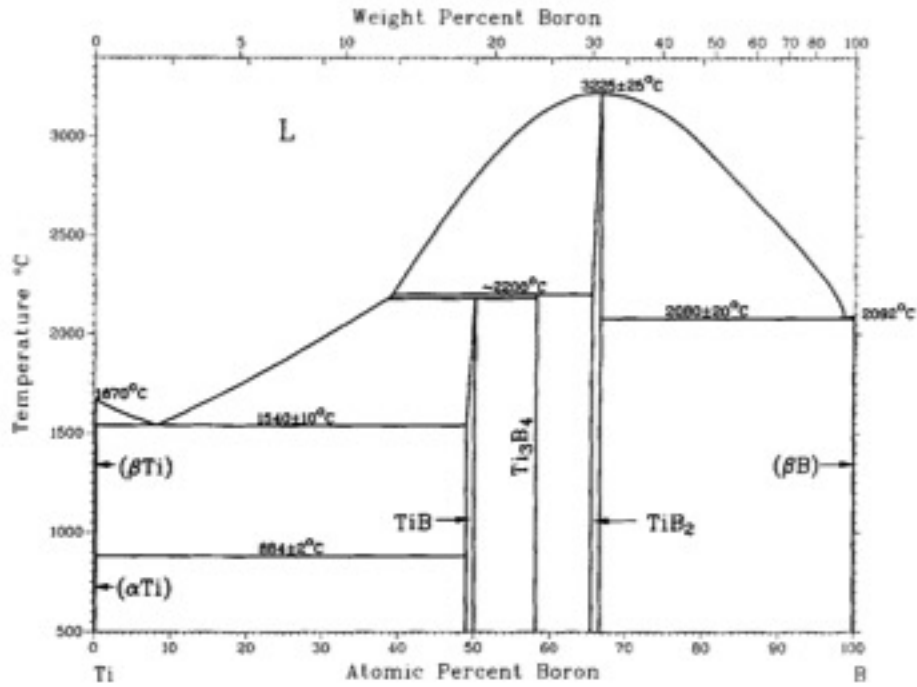
Figure A.35: Experimental phase diagram for the Ti-B system [89]

A.9   Conclusion

As shown through these examples, we can construct a very high quality equation of state through the method proposed by Fried and Howard [68]. This can be applied to any system of interest and used in continuum simulations of energetic materials. This method does have a downside in that it relies heavily on heat capacity and thermal expansion data at room temperature. Also, it is important to have information on the bulk modulus and its pressure derivative. The EOS of a material cannot be approximated without these data.
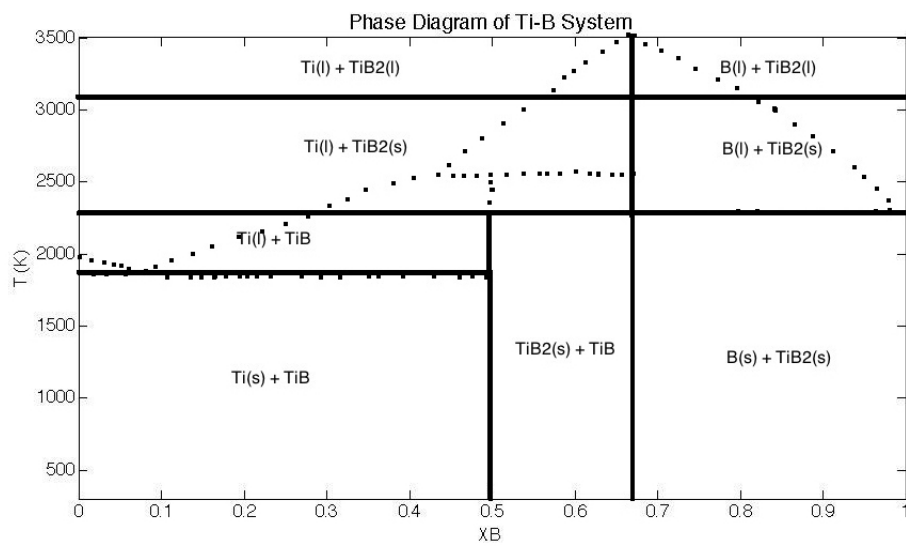
Figure A.36: Comparison between experimental [89] and fitted data of the phase diagram for the Ti-B system. XB represents the molar fraction of Boron. The dotted line represents the experimental data while solid line represents the data using Fried-Howard [68] model.

Appendix B

Diffusion Coefficients in Al/CuO

The diffusion velocities, V_i, in Equation (4.29) are a function of mass fractions. The diffusion coefficients for each V_i are listed below.

Diffusion coefficients of V_1:

$$a_1 = c_1 = e_1 = g_1 = -\frac{\mathscr{D}_{SL}}{Y_1 + Y_3 + Y_5 + Y_7}$$

$$b_1 = d_1 = f_1 = 0$$

Diffusion coefficients of V_2:

$$a_2 = c_2 = e_2 = g_2 = -\frac{\mathscr{D}_{SL}(\mathscr{D}_{LL}Y_2 - \mathscr{D}_{SL}Y_2)}{Y_2(\mathscr{D}_{SL} + \mathscr{D}_{LL}Y_1 + \mathscr{D}_{LL}Y_3 + \mathscr{D}_{LL}Y_5 + \mathscr{D}_{LL}Y_7 - \mathscr{D}_{SL}Y_1 - \mathscr{D}_{SL}Y_3 - \mathscr{D}_{SL}Y_5 - \mathscr{D}_{SL}Y_7)}$$

$$b_2 = -\frac{\mathscr{D}_{LL}\mathscr{D}_{SL}}{Y_2(\mathscr{D}_{SL} + \mathscr{D}_{LL}Y_1 + \mathscr{D}_{LL}Y_3 + \mathscr{D}_{LL}Y_5 + \mathscr{D}_{LL}Y_7 - \mathscr{D}_{SL}Y_1 - \mathscr{D}_{SL}Y_3 - \mathscr{D}_{SL}Y_5 - \mathscr{D}_{SL}Y_7)}$$

$$d_2 = f_2 = 0$$

Diffusion coefficients of V_3:

$$a_3 = c_3 = e_3 = g_3 = -\frac{\mathscr{D}_{SL}}{Y_1 + Y_3 + Y_5 + Y_7}$$

$$b_3 = d_3 = f_3 = 0$$

Diffusion coefficients of V_4:

$$a_4 = c_4 = e_4 = g_4 = -\frac{\mathscr{D}_{SL}(\mathscr{D}_{LL}Y_4 - \mathscr{D}_{SL}Y_4)}{Y_4(\mathscr{D}_{SL} + \mathscr{D}_{LL}Y_1 + \mathscr{D}_{LL}Y_3 + \mathscr{D}_{LL}Y_5 + \mathscr{D}_{LL}Y_7 - \mathscr{D}_{SL}Y_1 - \mathscr{D}_{SL}Y_3 - \mathscr{D}_{SL}Y_5 - \mathscr{D}_{SL}Y_7)}$$

$$d_4 = -\frac{\mathscr{D}_{LL}\mathscr{D}_{SL}}{Y_4(\mathscr{D}_{SL} + \mathscr{D}_{LL}Y_1 + \mathscr{D}_{LL}Y_3 + \mathscr{D}_{LL}Y_5 + \mathscr{D}_{LL}Y_7 - \mathscr{D}_{SL}Y_1 - \mathscr{D}_{SL}Y_3 - \mathscr{D}_{SL}Y_5 - \mathscr{D}_{SL}Y_7)}$$

$$b_4 = f_4 = 0$$

Diffusion coefficients of V_5:

$$a_5 = c_5 = e_5 = g_5 = -\frac{\mathscr{D}_{SL}}{Y_1 + Y_3 + Y_5 + Y_7}$$

$$b_5 = d_5 = f_5 = 0$$

Diffusion coefficients of V_6:

$$a_6 = c_6 = e_6 = g_6 = -\frac{\mathscr{D}_{SL}(\mathscr{D}_{LL}Y_6 - \mathscr{D}_{SL}Y_6)}{Y_6(\mathscr{D}_{SL} + \mathscr{D}_{LL}Y_1 + \mathscr{D}_{LL}Y_3 + \mathscr{D}_{LL}Y_5 + \mathscr{D}_{LL}Y_7 - \mathscr{D}_{SL}Y_1 - \mathscr{D}_{SL}Y_3 - \mathscr{D}_{SL}Y_5 - \mathscr{D}_{SL}Y_7)}$$

$$f_6 = -\frac{\mathscr{D}_{LL}\mathscr{D}_{SL}}{Y_6(\mathscr{D}_{SL} + \mathscr{D}_{LL}Y_1 + \mathscr{D}_{LL}Y_3 + \mathscr{D}_{LL}Y_5 + \mathscr{D}_{LL}Y_7 - \mathscr{D}_{SL}Y_1 - \mathscr{D}_{SL}Y_3 - \mathscr{D}_{SL}Y_5 - \mathscr{D}_{SL}Y_7)}$$

$$b_6 = d_6 = 0$$

Diffusion coefficients of V_7:

$$a_7 = c_7 = e_7 = g_7 = -\frac{\mathscr{D}_{SL}}{Y_1 + Y_3 + Y_5 + Y_7}$$

$$b_7 = d_7 = f_7 = 0$$

The diffusion coefficients for V_8 can be found by using Equation (4.5). Therefore:

$$V_8 = -(Y_1V_1 + Y_2V_2 + Y_3V_3 + Y_4V_4 + Y_5V_5 + Y_6V_6 + Y_7V_7)/Y_8$$

Appendix C

Numerical Procedure of Ti-B Counterflow Equations

The numerical procedure is based on the time-dependent equations

$$\rho \frac{\partial \bar{\vartheta}}{\partial t} + \rho u \frac{\partial \bar{\vartheta}}{\partial x} + \rho \bar{\vartheta}^2 = C \tag{C.1}$$

$$\rho \frac{\partial Y_1}{\partial t} + \rho u \frac{\partial Y_1}{\partial x} + \frac{\partial}{\partial x}\Big[\rho\Big(a_1 \frac{\partial Y_1}{\partial x} + b_1 \frac{\partial Y_2}{\partial x}\Big)\Big] = -W_1\,\omega \tag{C.2}$$

$$\rho \frac{\partial Y_2}{\partial t} + \rho u \frac{\partial Y_2}{\partial x} + \frac{\partial}{\partial x}\Big[\rho\Big(a_2 \frac{\partial Y_1}{\partial x} + b_2 \frac{\partial Y_2}{\partial x}\Big)\Big] = -2W_2\,\omega \tag{C.3}$$

$$\rho c_p\Big(\frac{\partial T}{\partial t} + u\frac{\partial T}{\partial x}\Big) - K\frac{\partial^2 T}{\partial x^2} = Q\omega\,, \tag{C.4}$$

with u obtained from

$$\rho\bar{\vartheta} = -\frac{d}{dx}(\rho u) \tag{C.5}$$

and ρ from (3.17). Initially, we solved the equations using an explicit time marching method until the solution converges to its equilibrium state. The integration in time starts with an initial guess, taken here as the asymptotic solution discussed in the previous section. We used a fourth order approximation to compute the first order and second order space derivatives and a fourth order Runge-Kutta (RK4) method for time stepping. The extent of the numerical domain depends on the strain rate value, with lower strain rates requiring a larger domain. This, however, can be overcome by normalizing x with the thermal diffusion length $l_d = \sqrt{\alpha/\epsilon}$, as is also evident from the analytical form of the asymptotic solution. Due to large stiffness arising from the Arrhenius exponential in the reaction rate term, we found that the time step in general could not exceed 10^{-9} and to properly describe the solution at low strain rates where the reaction zone becomes extremely thin, a fine grid is also required. As a result, the convergence was very slow even after parallelizing

the numerical code. Determining the solution over a wide range of strain rate conditions requires a faster converging algorithm.

Thus, Implicit time relaxation methods were implemented to overcome the computational stiffness, and are described next. First and second order spatial derivatives are approximated by second order finite difference schemes on a uniform grid. For time stepping we use a backward Euler method such that a generic equation of the form

$$\frac{\partial \phi}{\partial t} = f(t, \phi),$$

is approximated by

$$\phi^{n+1} = \phi^n + \Delta t\, f(t^{n+1}, \phi^{n+1}),$$

where n denotes the time step and Δt the time increment. A damped Newton-Raphson solver is then used for solving this nonlinear system at each time step. We used a relaxation value of 0.1 during each iterative update to limit the fluctuations that occur due to stiffness in the governing equations, which causes sharp gradients in the Jacobian matrix. Therefore, without the relaxation parameter the numerical solution may diverge due to strong fluctuations. The PetSC sparse solver [90] is used for the system that arises during the Newton-Raphson iteration. We note that this approach has significantly reduced the time step relative to the explicit scheme from 10^{-9} required to 10^{-2}, for the same spatial grid distribution.

An objectives is to generate solutions for increasing values of the strain rate ϵ and draw response curves of quantities of interest (e.g., flame temperature, mass fraction of unconsumed reactants, etc.) as a function of ϵ. We start with a small strain rate value of $\epsilon = 0.01\,\mathrm{s}^{-1}$, using the asymptotic solution as an initial guess and advance in time until the incremental changes in the solution at all points in the domain of integration are less than a tolerance error, here taken as 10^{-3}.

This direct approach works well for small values of ϵ but fails at larger values when the solution becomes multi-valued, and the response curve develops a turning point with stable and unstable branches. Near the turning point we adopted an approach continuation proposed by Kurdyumov

113

and Matalon [29], whereby the time-dependent equations were solved with an additional constraint that the temperature remains constant at some reference point, say $T(x^*) = T^*$. The constraint is used to iterate on the value of ϵ, until both the strain rate and the space distribution of solution do not vary significantly from one time step to the next. By selecting T^* judiciously, this procedure converges to a solution that may be stable or unstable, allowing us to generate the entire response curve.

It is important to note that the time steps must be adaptively changed while keeping the damped newton iterations to achieve convergence. This is iteratively done by trial and error. At the start of simulation, a time step is guessed and the solution is closely watched over the first few iterations. If these solutions are not stable, then the time is decreased; otherwise, the time step is increased until the solutions in the few iterations become unstable. This determines the maximum time step that the problem allows us to take at the start of the simulation, which in this Ti-B case is approximately 10^{-6}. Then, after the first few iterations at this time step, it is again increased slowly. This procedure is repeated until the volatility at the start of the simulation disappears, which leads us to take larger time time steps. After approximately 2000 initial iterations, the time step can be increased as high as 10^{-2}.

References

[1] T. P. Weihs, *Self-propogating reactions in multilayer materials*, ch. F7. Institute of Physics, 1998.

[2] G. M. Fritz, H. Joress, and T. P. Weihs, "Enabling and controlling slow reaction velocities in low-density compacts of multilayer reactive particles," *Combustion and Flame*, vol. 158, pp. 1084–1088, 2011.

[3] C. on Advanced Energetic Materials and M. Technologies, "Advanced energetic materials," tech. rep., National Research Council of the National Academies, 2004.

[4] M. W. Beckstead, K. Puduppakkama, P. Thakreb, and V. Yang, "Modeling of combustion and ignition of solid-propellant ingredients," *Pogress in Energy and Combustion Science*, vol. 33, pp. 497–551, 2007.

[5] M. D. Clemenson, S. Johnson, H. Krier, and N. Glumac, "Explosive initiation of various forms of ti/2b reactive materials," *Propellants Explos. Pyrotech.*, vol. 39, pp. 454 – 462, 2014.

[6] S. P. Koundinyan, J. B. Bdzil, M. Matalon, and D. S. Stewart, "Diffusion flames in condensed-phase energetic materials: Application to titaniumboron combustion," *Combustion and Flame*, vol. 162, no. 12, pp. 4486–4496, 2015.

[7] N. Glumac, D. Stewart, M. Clemenson, S. Koundinyan, J. Bdzil, and J. Foster, "Shock actuated burning of thermitic and inter-metallic reactive composite materials in preparation, results presented for integrated experimental and modeling study of meso-scale processes in reactive materials," Tech. Rep. HDTRA-08-10, Defense Threat Reduction Agency Basic Research Technical Review, 2014.

[8] F. A. Williams, *Combustion Theory 2nd*. Princeton University, 1985.

[9] A. Linan, "The asymptotic structure of counterflow diffusion flames for large activation energies," *Acta Astronautica*, vol. 1, pp. 1007–1039, 1974.

[10] J. S. Kim and F. A. Williams, "Extinction of diffusion flames with nonunity Lewis numbers," *Journal of engineering mathematics*, vol. 31, no. 2–3, pp. 101–118, 1997.

[11] H. G. Im, C. K. Law, J. S. Kim, and F. A. Williams, "Response of counterflow diffusion flames to oscillating strain rates," *Combustion and Flame*, vol. 100, no. 1–2, pp. 21–30, 1995.

[12] L. Krishnamurthy, F. A. Williams, and K. Seshadri, "Asymptotic theory of diffusion-flame extinction in the stagnation-point boundary layer," *Combustion and Flame*, vol. 26, pp. 363–377, Feb. 1976.

[13] S. Cheatham and M. Matalon, "A general asymptotic theory of diffusion flames with application to cellular instability," *Journal of Fluid Mechanics*, vol. 414, pp. 105–144, 2000.

[14] M. D. Smooke, R. E. Mitchell, and D. E. Keyes, "Numerical solution of two-dimensional axisymmetric laminar diffusion flames," *Combustion Science and Technology*, vol. 67, no. 4-6, pp. 85–122, 1986.

[15] J. A. M. Mitchell D. Smooke and R. J. Kee, "Solution of premixed and counterflow diffusion flame problems by adaptive boundary value methods," in *Numerical Boundary Value ODEs* (U. M. Ascher and R. D. Russell, eds.), ch. 18, pp. 303–317, Birkhauser, 1985.

[16] G. Ribert, N. Zong, V. Yang, L. Pons, N. Darabiha, and S. Candel, "Counterflow diffusion flames of general fluids: Oxygen/hydrogen mixtures," *Combustion and Flame*, vol. 154, no. 3, pp. 319–330, 2008.

[17] G. Dixon-Lewis, T. David, P. Gaskell, S. Fukutani, H. Jinno, J. Miller, R. Kee, M. Smooke, N. Peters, E. Effelsberg, J. Warnatz, and F. Behrendt, "Calculation of the structure and extinction limit of a methane-air counterflow diffusion flame in the forward stagnation region of a porous cylinder," *International Symposium on Combustion*, vol. 20, no. 1, pp. 1893–1904, 1984.

[18] N. Peters and R. J. Kee, "The computation of stretched laminar methane-air diffusion flames using a reduced four-step mechanism," *Combustion and Flame*, vol. 68, no. 1, pp. 17–29, 1987.

[19] D. E. Keyes and M. D. Smooke, "Flame sheet starting estimates for counterflow diffusion flame problems," *Journal of Computational Physics*, vol. 73, no. 2, pp. 267–288, 1987.

[20] M. D. Smooke, I. K. Puri, and K. Seshadri, "A comparison between numerical calculations and experimental measurements of the structure of a counterflow diffusion flame burning diluted methane in diluted air," *International Symposium on Combustion*, vol. 21, no. 1, pp. 1783–1792, 1988.

[21] N. Darabiha, "Transient behaviour of laminar counterflow hydrogen-air diffusion flames with complex chemistry," *Combustion science and technology*, vol. 86, pp. 163–181, 1992.

[22] O. Gicquel, N. Darabiha, and D. Thévenin, "Laminar premixed hydrogen/air counterflow flame simulations using flame prolongation of ILDM with differential diffusion," *Proceedings of the Combustion Institute*, vol. 28, no. 2, pp. 1901–1908, 2000.

[23] H. Tsuji, "Counterflow diffusion flames," *Progress in Energy and Combustion Science*, vol. 8, no. 2, pp. 93–119, 1982.

[24] S. Ishizuka and H. Tsuji, "An experimental study of effect of inert gases on extinction of laminar diffusion flames," *International Symposium on Combustion*, vol. 18, no. 1, pp. 695–703, 1981.

[25] C. J. Sung, J. B. Liu, and C. K. Law, "Structural response of counterflow diffusion flames to strain rate variations," *Combustion and Flame*, vol. 102, pp. 481–492, Sept. 1995.

[26] I. K. Puri and K. Seshadri, "Extinction of diffusion flames burning diluted methane and diluted propane in diluted air," *Combustion and Flame*, vol. 65, no. 2, pp. 137–150, 1986.

[27] J. S. T'ien and D. W. Foutch, "Extinction of a stagnation-point diffusion flame at reduced gravity," *AIAA journal*, vol. 25, no. 7, pp. 972–976, 1987.

[28] MATLAB, *version 8.4.0 (R2014b)*. Natick, Massachusetts: The MathWorks Inc., 2014.

[29] V. N. Kurdyumov and M. Matalon, "Dynamics of an edge flame in a mixing layer," *Combustion and Flame*, vol. 139, no. 4, pp. 329–339, 2004.

[30] M. Füri, P. Papas, and P. A. Monkewitz, "Non-premixed jet flame pulsations near extinction," *Proceedings of the Combustion Institute*, vol. 28, no. 1, pp. 831–838, 2000.

[31] E. Eteng, G. Ludford, and M. M., "Displacement effect of a flame in a stagnation-point flow," *Physics of Fluids*, vol. 29, no. 7, pp. 2172–2180, 1986.

[32] M. A. Trunov, V. K. Hoffmann, M. Schoenitz, and E. L. Dreizin, "Combustion of boron-titanium nanocomposite powders in different environments," *Journal of Propulsion and Power*, vol. 24, no. 2, pp. 184–191, 2008.

[33] A. S. Rogachev, "Exothermic reaction waves in multilayer nanofilms," *Russian Chemical Reviews*, vol. 77, no. 1, pp. 21–37, 2008.

[34] D. Adams, "Reactive multilayers fabricated by vapor deposition: A critical review," *Thin Solid Films*, vol. 576, pp. 98–128, 2015.

[35] T. P. Weihs, "Fabrication and characterization of reactive multilayer films and foils," in *Metallic Films for Electronic, Optical and Magnetic Applications: Structure, Processing and Properties* (K. Barmak and K. Coffey, eds.), Woodhead Publishing Series in Electronic and Optical Materials, 2014.

[36] R. Reeves, "Condensed-phase and oxidation reaction behavior of ti/2b foils in varied gaseous environments," *Journal of Physical Chemistry C*, vol. 116, pp. 17904–17912, 2012.

[37] I. Sraj, "Numerical simulation of shock initiation of ni/al multilayered composites," *Journal of Applied Physics*, vol. 115, no. 023515, 2014.

[38] S. Zhao, "Molecular dynamics simulation of dynamical response of perfect and porous ni/al nanolaminates under shock loading," *Physical Review B*, vol. 76, no. 014103, 2007.

[39] D. R. Gaskell, *Introduction to the Thermodynamics of Materials*. Taylor and Francis, 5th ed., 2008.

[40] C. F. Curtiss, "Symmetric gaseous diffusion coefficients," *J. Chem. Phys.*, vol. 49, pp. 2917–2919, 1968.

[41] C. F. Curtiss and R. B. Bird, "Multicomponent diffusion," *Ind. Eng. Chem. Res.*, pp. 2515–2522, 1999.

[42] J. O. Hirschfelder, C. F. Curtiss, and R. B. Bird, *Molecular theory of gases and liquids*. Wiley, 1954.

[43] R. Taylor and R. Krishna, *Multicomponent Mass Transfer*. Wiley, 1993.

[44] Z. Fan and B. Cantor, "The kinetics and mechanism of interfacial reaction in sigma fibre-reinforced ti mmcs," *Composites Part A*, vol. 28A, pp. 131–140, 1997.

[45] H. Scmidt, "Self-diffusion of boron in titanium diboride," *J. Appl. Phys*, vol. 93, no. 2, pp. 907–911, 2003.

[46] I. Barin, *Thermochemical Data of Pure Substances*. Weinheim: VCH, 1995.

[47] "Boron (b) thermal duffusivity and conductivity, beta-rhombohedral boron," tech. rep., 1998.

[48] G. K. White, "Thermal conductivity at 273 - 300 k," in *Thermal conductivity of pure metals and Alloys* (O. Madelung and G. K. White, eds.), vol. 15c, Springer, 2015.

[49] R. Munro, "Material properties of titanium diboride," *J. Res. Natl. Inst. Stand. Technol*, vol. 105, pp. 709–720, 2000.

[50] M. Pacheco, *Self-sustained High-temperature Reactions: Initiation, propagation and synthesis*. PhD thesis, Universidad Carlos III de Madrid, 2007.

[51] N. L. Peterson, "Diffusion in refractory metals," Tech. Rep. 60–793, Wadd Technical Report, 1960.

[52] B. Sarma and K. RaviChandran, "Accelerated kinetics of surface hardening by diffusion near phase transition temperature: Mechanism of growth of boride layers on titanium," *Acta Materialia*, vol. 59, pp. 4216–4228, 2011.

[53] S. Fischer and M. Grubelich, "A survey of combustible metals, thermites, and intermetallics for pyrotechnic applications," *AIAA 32nd Joint Propulsion Conference and Exhibit*, 1996.

[54] D. S. Stewart, "A gibbs formulation for reactive materials with phase change," in *Proc. of the Conf. of the APS Topical Group on SCCM (Tampa, Florida)*, 2015. To appear.

[55] M. J. O'Neil, *The Merck index: an encyclopedia of chemicals, drugs, and biologicals*. Merck, 2001.

[56] R. W. Powell, C. Y. Ho, and P. E. Liley, "Thermal conductivity of selected materials," 1966.

[57] P. M. Nasch and S. G. Steinemann, "Density and thermal expansion of molten manganese, iron, nickel, copper, aluminum and tin by means of the gamma-ray attenuation technique," *Physics and Chemistry of Liquids*, vol. 29, no. 1, pp. 43–58, 1995.

[58] M. W. Chase, *NIST-JANAF thermochemical tables*. American Chemical Society, 1998.

[59] W. J. Knapp, "Thermal conductivity of nonmetallic single crystals*," *Journal of the American Ceramic Society J American Ceramic Society*, vol. 26, no. 2, pp. 48–55, 1943.

[60] D. R. Lide and W. M. Haynes, *CRC handbook of chemistry and physics*. CRC Press, 2009.

[61] M. A. Kedzierski, "Viscosity and density of cuo nanolubricant," *International Journal of Refrigeration*, vol. 35, no. 7, pp. 1997–2002, 2012.

[62] S. Ansell, S. Krishnan, J. K. R. Weber, J. J. Felten, P. C. Nordine, M. A. Beno, D. L. Price, and M.-L. Saboungi, "Structure of liquid aluminum oxide," *Physical Review Letters*, vol. 78, no. 3, pp. 464–466, 1997.

[63] M. Manga and R. Jeanloz, "Thermal conductivity of corundum and periclase and implications for the lower mantle," *J. Geophys. Res. Journal of Geophysical Research: Solid Earth*, vol. 102, pp. 2999–3008, Oct 1997.

[64] V. Sarou-Kanian, F. Millot, and J. C. Rifflet, "Surface tension and density of oxygen-free liquid aluminum at high temperature," *International Journal of Thermophysics*, vol. 24, no. 1, pp. 277–286, 2003.

[65] E. L. Cussler, *Diffusion: mass transfer in fluid systems*. Cambridge University Press, 2015.

[66] H. Mehrer, *Diffusion in solids: fundamentals, methods, materials, diffusion-controlled processes*. Springer, 2007.

[67] K. Lee, K. Joshi, S. Chaudhuri, and D. S. Stewart, "Mirrored continuum and molecular scale simulations of the ignition of high-pressure phases of rdx," *The Journal of Chemical Physics J. Chem. Phys.*, vol. 144, no. 18, 2016.

[68] L. E. Fried and W. M. Howard, "Explicit gibbs free energy equation of state applied to the carbon phase diagram," *Phys. Rev. B Physical Review B*, vol. 61, pp. 8734–8743, Jan 2000.

[69] J. Tallon and A. Wolfenden, "Temperature dependence of the elastic constants of aluminum," *Journal of Physics and Chemistry of Solids*, vol. 40, no. 11, pp. 831–837, 1979.

[70] G. Kerley, "Theoretical equation of state for aluminum," *International Journal of Impact Engineering*, vol. 5, no. 1-4, pp. 441–449, 1987.

[71] K. S. Holian, "A new equation of state for aluminum," *J. Appl. Phys. Journal of Applied Physics*, vol. 59, no. 1, p. 149, 1986.

[72] J. Peng, F. Jing, D. Li, and L. Wang, "Pressure and temperature dependence of shear modulus and yield strength for aluminum, copper, and tungsten under shock compression," *J. Appl. Phys. Journal of Applied Physics*, vol. 98, 2005.

[73] S. P. Marsh, *LASL shock hugoniot data*. University of California Press, 1980.

[74] G. Fiquet, P. Richet, and G. Montagnac, "High-temperature thermal expansion of lime, periclase, corundum and spinel," *Physics and Chemistry of Minerals*, vol. 27, no. 2, pp. 103–111, 1999.

[75] L. S. Dubrovinsky, S. K. Saxena, and P. Lazor, "High-pressure and high-temperature in situ x-ray diffraction study of iron and corundum to 68 gpa using an internally heated diamond anvil cell," *Physics and Chemistry of Minerals*, vol. 25, no. 6, pp. 434–441, 1998.

[76] M. Binnewies and E. Milke, *Thermochemical data of elements and compounds*. Wiley-VCH, 1999.

[77] B. Glorieux, F. Millot, J.-C. Rifflet, and J.-P. Coutures, "Density of superheated and undercooled liquid alumina by a contactless method," *International Journal of Thermophysics*, vol. 20, no. 4, pp. 1085–1094, 1999.

[78] A. K. Verma, P. Modak, and B. B. Karki, "First-principles simulations of thermodynamical and structural properties of liquid al2o3 under pressure," *Phys. Rev. B Physical Review B*, vol. 84, no. 17, 2011.

[79] J. Zhang, Y. Zhao, R. S. Hixson, G. T. Gray, L. Wang, W. Utsumi, S. Hiroyuki, and H. Takanori, "Thermal equations of state for titanium obtained by high pressuretemperature diffraction studies," *Phys. Rev. B Physical Review B*, vol. 78, no. 5, 2008.

[80] G. I. Kerley, "Equations of state for titanium and ti6a14v alloy.," *SAND 2003-3785*, Jan 2003.

[81] P.-F. Paradis and W.-K. Rhim, "Non-contact measurements of thermophysical properties of titanium at high temperature," *The Journal of Chemical Thermodynamics*, vol. 32, no. 1, pp. 123–133, 2000.

[82] K. Shirai, A. Masago, and H. Katayama-Yoshida, "High-pressure properties and phase diagram of boron," *physica status solidi (b) phys. stat. sol. (b)*, vol. 244, no. 1, pp. 303–308, 2007.

[83] D. N. Sanz, P. Loubeyre, and M. Mezouar, "Equation of state and pressure induced amorphization of beta boron from x-ray measurements up to 100 gpa," *Phys. Rev. Lett. Physical Review Letters*, vol. 89, no. 24, 2002.

[84] P.-F. Paradis, T. Ishikawa, and S. Yoda, "Non-contact density measurements of liquid, undercooled, and high temperature solid boron," *Appl. Phys. Lett. Applied Physics Letters*, vol. 86, no. 15, 2005.

[85] W. Chun-Lei, Y. Ben-Hai, H. Hai-Liang, C. Dong, and S. Hai-Bin, "First principle study on the elastic and thermodynamic properties of tib 2 crystal under high temperature," *Chinese Physics B Chinese Phys. B*, vol. 18, no. 3, pp. 1248–1252, 2009.

[86] C. A. Perottoni, A. S. Pereira, and J. A. H. D. Jornada, "Periodic hartree-fock linear combination of crystalline orbitals calculation of the structure, equation of state and elastic properties of titanium diboride," *Journal of Physics: Condensed Matter J. Phys.: Condens. Matter*, vol. 12, no. 32, pp. 7205–7222, 2000.

[87] G. Cao, L. Geng, and M. Naka, "Elastic properties of titanium monoboride measured by nanoindentation," *Journal of the American Ceramic Society J American Ceramic Society*, vol. 89, no. 12, 2006.

[88] B. F. Decker and J. S. Kasper, "The crystal structure of tib," *Acta Crystallographica Acta Cryst*, vol. 7, pp. 77–80, Jan 1954.

[89] J. L. Murray, P. K. Liao, and K. E. Spear, "The bti (boron-titanium) system," *Bulletin of Alloy Phase Diagrams*, vol. 7, no. 6, pp. 550–555, 1986.

[90] PETSc, *version 3.4.3.* Lemont, IL: Argonne National Lab, 2013.